ARCHIVES
OF CIVIL AND MECHANICAL
ENGINEERING

EDITOR IN CHIEF

ZBIGNIEW GRONOSTAJSKI

EDITORIAL LAYOUT AND PROOF-READING

WIOLETTA GÓRALCZYK

TYPESETTING

SEBASTIAN ŁAWRUSEWICZ

SECRETARY

WIOLETTA GÓRALCZYK

Publisher: Committee of Civil and Mechanical Engineering
of Polish Academy of Sciences – Wrocław Branch,
Faculty of Civil Engineering and Faculty of Mechanical Engineering
of Wrocław University of Technology

Contents

Spis treści

Criteria of effective materials cutting
with suspension abrasive-water jet

J. BORKOWSKI, P. BORKOWSKI

University of Technology Koszalin, Unconventional HydroJetting Technology Center, ul. Racławicka 15–17, 75-620 Koszalin, Poland

The present work discuss criteria of the cutting process optimization using the original BorJet method that allows the suspension abrasive-water jet and the suspension hybrid water jet to be formed. Results of optimization investigations carried out on the base of criteria for minimizing the costs of abradant consumption and the total costs of machining are presented too.

Keywords: *suspension abrasive-water jet, costs of the process, optimization*

1. Introduction

The processes of high-pressure abrasive-water jet material treatment have more and more effectively competed with conventional cutting methods in the last decade. The cutting with suspension water jet has undergone development that is even more intensive. The first installations of this type were designed at the end of the eighties, in the form of DIAJET's [9] and original BORJET's [2, 4], where the efficiency of abrasive-water mixture under conditions of the circular jet motion with respect to the abradant bed was utilized markedly. In the nineteen nineties there was an extremely rapid development in novel machining systems [10, 11] and technological equipment [12, 13] making it possible to work at the highest (up to 200 MPa) pressure [7]. On the basis of own seven years' work, a novel BorJet unit construction [3] has been created. At the end of this period, an appropriate control system for the suspension water jet was worked out [6, 8]. Our own research [1, 5] focused on the optimization of such the cutting process was also carried out.

The present work is devoted to the optimization issues of cutting various materials using the suspension water jet produced according to our own BorJet system.

2. Cutting optimisation

Experimental results, after considering the economic and technological aspects, provide a solid basis for optimizing the process of cut using the suspension water jet produced according to BorJet system [1, 3, 5]. When optimizing such the cutting process one should consider the minimization of the energy consumption in the course of cutting, duration of operation, abrasive consumption and cutting costs.

The first three criteria show the importance of individual process parameters influence on its run whereas the last one is responsible for its total effects. In practice, the cutting optimization is usually carried out based on the last two criteria.

2.1. Abrading consumption costs minimization

The optimum selection of abrasive material for the cutting process using the suspension water jet should possibly provide the most advantageous effects of processing at the lowest commodity price. The cutting operations, where the maximum depth of cutting plays the most important part, is characterized by the factor that perfectly illustrates the effects achieved, so-called "the individual surface cut-off speed", expressed by the Equation:

$$v_F = v_p \cdot h \ [\mathrm{mm^2/s}], \tag{1}$$

where:

v_p is the feed velocity and h – depth of cut.

The above coefficient expressed by Formula (1) is also useful to estimate the costs of abradant consumption. It determines "the unit cost of abradant" expressing the exclusive cost of abrasive material used for cutting the unit of surface cut-off trace. It describes the following relation:

$$K_S = \frac{\dot{m}_a \cdot C_A}{h \cdot v_p} \ [\mathrm{PLN/mm^2}], \tag{2}$$

where:

$\dot{m}_a$ is the mass abradant consumption,

C_A is the price of 1 kg of abrasive material.

The abradant unit costs specified in this way make it also possible to evaluate the costs of cutting the surface depending on the type of abrasive material applied and its consumption.

2.2. Criterion for minimizing the total costs of cutting

The costs of cutting using the suspension water jet are affected by a series of factors, including the most important, i.e. the costs of the unit depreciation, the labour costs, and the costs of energy, abradant and water consumption. It enables to introduce the notion of "the unit cost of surface cutting" K_j described by the following relation:

$$K_j = n \cdot \frac{\sum \dot{K}}{h \cdot v_p} = n \cdot \frac{\dot{K}_E + \dot{K}_A + \dot{K}_W + \dot{K}_R + \dot{K}_{AM}}{h \cdot v_p} \ [\mathrm{PLN/mm^2}], \tag{3}$$

where:

$\dot{K}_E$ – cost of energy,

$\dot{K}_A$ – cost of abradant,

$\dot{K}_W$ – cost of water,

$\dot{K}_R$ – cost of labour,

$\dot{K}_{AM}$ – cost of unit depreciation,

n – number of paths,

h – depth of cut,

v_p – feed velocity.

Beside the above costs there are also other charges imposed, including the maintenance of premises and the transportation of work materials. These costs shall not be estimated here because their level depends directly on the cutting process.

3. Optimisation tests

The process of cutting with the suspension water jet was examined using a modified BorJet unit. This unit generates the suspension water jet with the following process parameters: $p_{max} = 35$ MPa, $Q_{max} = 1.5$ dm^3/s, $v_p = 0.5$–20 mm/s.

3.1. Optimisation according to the criterion for minimising the costs of abradant consumption

It is possible to minimise the costs of abradant consumption applying relation (2). The costs of abradant consumption incurred in the course of cutting the mild construction steel (St3S) are illustrated in Figure 1. It gives an indication that an increase in water pressure contributes to the reduction of these costs and the change in abradant is parabolic in shape. The lowest costs of the order of 800 PLN/m^2 were incurred for the abradant consumption ranged from 60 to 70 g/s.

Similar characteristics of the abradant costs distribution occur in the case of cutting brass and aluminium alloys. The optimized costs of brass cutting are 2–3 times lower than for steel; while in case of PA4 alloy they are even over five times lower (Figure 2).

Similar relations of abradant consumption costs also occur in case of cutting textolite or marble and their minimal values could be reduced event to the level of 80 PLN/m^2 (for $\dot{m}_a = 60$ g/s). Not much higher are the sand consumption costs while cutting syenite (Figure 3) represents a group of hard rock materials.

An abrasive-water nozzle plays an essential part in the process using the suspension water jet created according to BorJet's system. An increase in a length of the nozzle involves higher costs of abradant consumption, while a change in a nozzle diameter is affected ambiguously. If an abrasive-water nozzle of 75 mm in its length is ap-

plied, the lowest costs of abradant consumption for a nozzle 2–2.25 mm in diameter shall be observed. For nozzles with a larger diameter the high-silica sand consumption is increased, like in case of a nozzle with a smaller diameter.
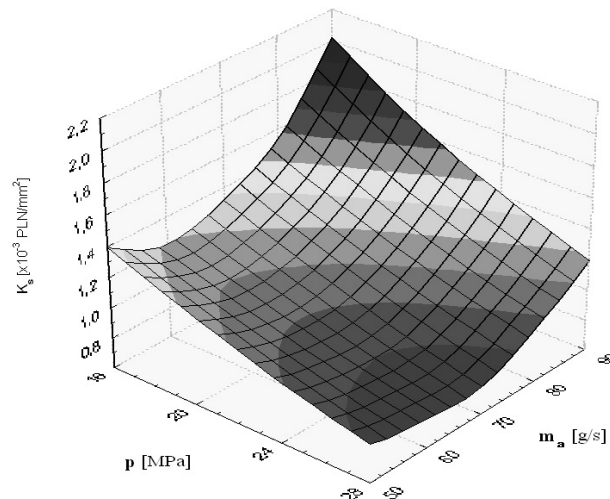
Fig. 1. Influence of water pressure and abradant consumption on its consumption costs during cutting of the steel St3S. Examination conditions: abrasive-water jet SiO_2 #30;
$v_p = 4$ mm/s, $d_{sc} = 2$ mm, $l_{sc} = 50$ mm, $s = 6$ mm
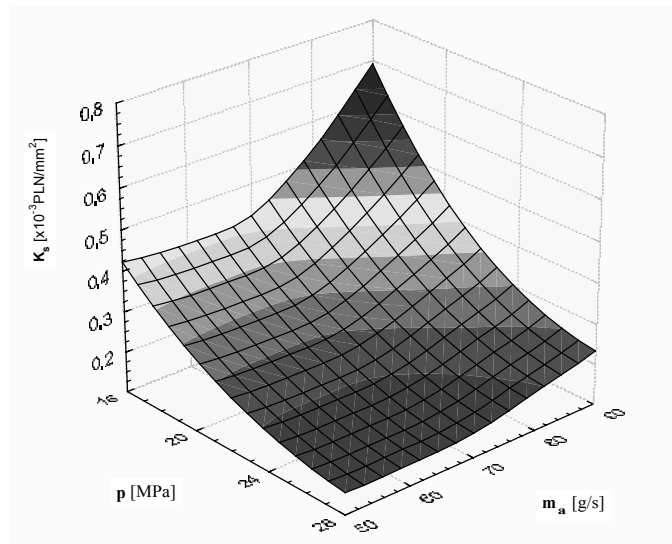
Fig. 2. Influence of water pressure and abradant consumption on its consumption costs during cutting of the PA4 aluminum alloy. Examination conditions: abrasive-water jet SiO_2 #30;
$v_p = 4$ mm/s, $d_{sc} = 2$ mm, $l_{sc} = 50$ mm, $s = 6$ mm
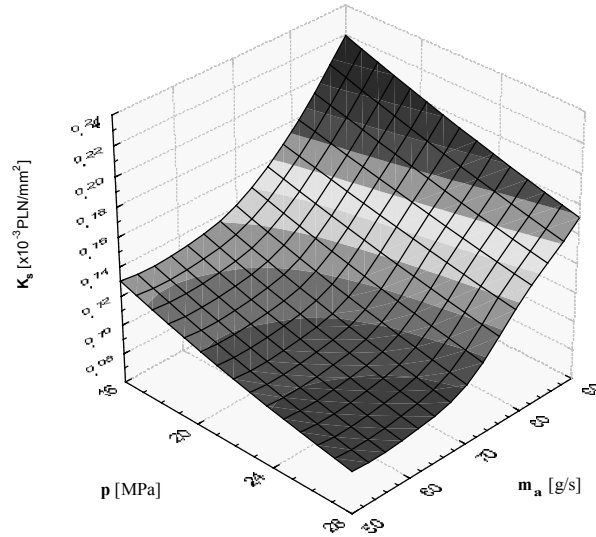
Fig. 3. Influence of water pressure and abradant consumption on its consumption costs during cutting of the syenite. Examination conditions: abrasive-water jet SiO_2 #30;
$v_p = 4$ mm/s, $d_{sc} = 2$ mm, $l_{sc} = 50$ mm, $s = 6$ mm
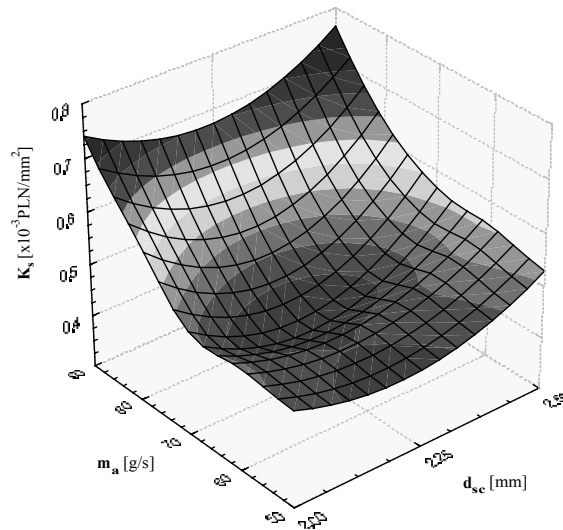
Fig. 4. Influence of water nozzle diameter and abradant consumption on its consumption costs during cutting of the St3S steel. Examination conditions: hybrid jet 1% Super-Water+SiO_2 #30;
$p = 28$ MPa, $v_p = 4$ mm/s, $l_{sc} = 75$ mm, $s = 6$ mm

However, applying the same abrasive-water nozzles under similar conditions of forming the hybrid suspension water jet with addition of Super-Water polymeric emulsion is more advantageous. It follows from the comparison of abradant consumption costs under such conditions that the above costs are from 20 to 30% lower for the hybrid jet (Figure 4) than for the abrasive-water jet.

Respecting the economic aspects, it is recommended to apply the silica sand to create the suspension water jet because of its highest efficiency. Moreover, the analysis of the research results shows that the optimisation of the cutting processes of suspension hybrid water jet due to the criterion for minimising the abradant consumption costs could be unreliable. Evidence of the above observations is close level of abrasive consumption costs in spite of a distinct difference in the costs of hybrid improvers introduced to the suspension water jet. Therefore, a more general criterion for optimisation, including also the costs of such improvers should be applied.

3.2. Minimisation of total machining costs

The optimisation of the abrasive suspension water jet machining, including all elements of the costs involved, with reference to relation (3) expresses the unit of surface cut-off. Some sample optimisation results according to such the collective criterion for minimising the costs are given in Figure 5. They are compiled in the form of histograms that illustrate the level of abradant consumption and the inner length as well as diameter of the abrasive-water nozzle has affected the total unit costs of the abrasive-water jet.
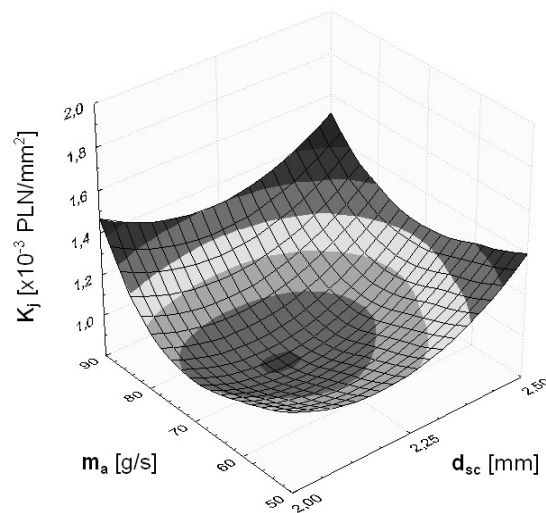
Fig. 5. Influence of abradant consumption and abrasive-water nozzle diameter on total unit cost for St3S steel cutting. Work conditions: ASJ SiO_2 #30; $p = 28$ MPa, $v_f = 4$ mm/s, $l_{sc} = 7.5$ mm, $s = 6$ mm

Characteristics of such the total unit costs in case of applying the suspension hybrid water jet are presented in Figure 6.
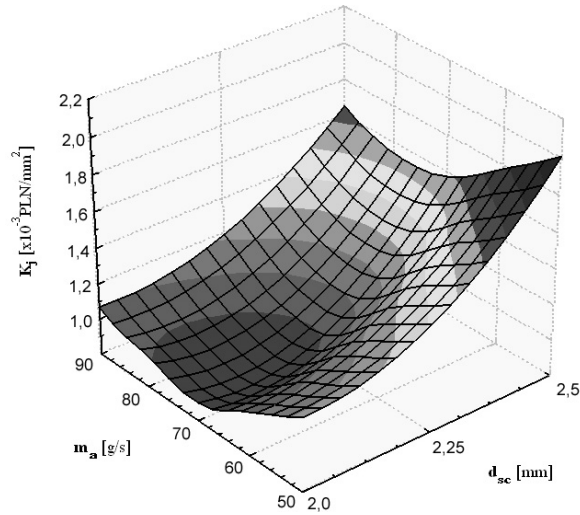
Fig. 6. Influence of abrasive-water nozzle diameter and abradant consumption on
total unit cost for St3S steel cutting. Examination conditions: hybrid jet 1% Super-Water+SiO_2 #30;
p = 28 MPa, v_p = 4 mm/s, l_{sc} = 75 mm, s = 6 mm
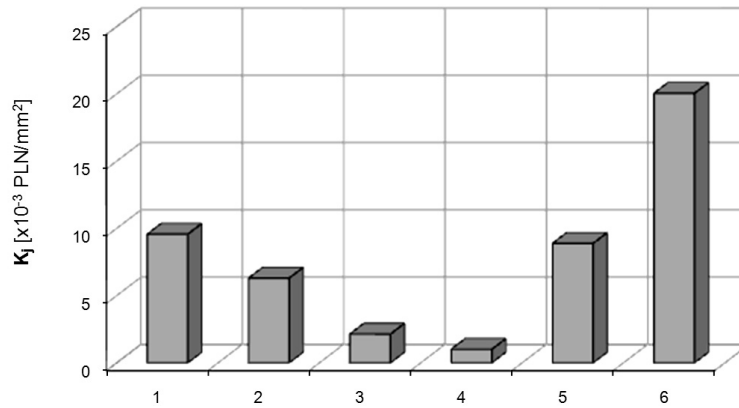
Fig. 7. Total unit cost for St3S steel cutting by BorJet method ($\dot{m}_a$ = 70 g/s, p = 28 MPa, v_f = 4 mm/s,
d = 2.2 mm): 1 – ASJ SiC #80, 2 – ASJ Al_2O_3 #46, 3 – ASJ Olivin silica #30, 4 – ASJ SiO_2 #30,
5 – HSJ SiO_2 #30 & 10% poly-hartenol E8, 6 – HSJ SiO_2 #30 & 15% polyfluid

Some interesting information in that scope provides histogram presented in Figure 7. It shows that the total costs of high-pressure suspension jet with admixtures of silica sand are definitely the lowest. Olivine sand admixtures to the suspension jet give simi-

lar costs of machining, while synthetic abrasive materials leads to a rapid increase in the abradant consumption costs. It results from a definitely higher price of such abrasive materials, which could not be balanced by the higher erosive efficiency of such the abrasive-water jet. The application of silicon carbide to the high-pressure jet is found to increase over 16 times in comparison to silica sand. This relation in case of alundum abradant is somewhat more favorable; however, the cost of this abradant consumption increases more than 10 times. Moreover, the suspension jets with polymer components were analyzed affecting on jet increased coherence. However, analysis of the above plots shows that the cutting processes using suspension jet with polymer components is extremely expensive.

The optimization of abrasive machining respecting all elements of costs involved reveals the occurrence of quite different relations than before, where different types of suspension hybrid water jets were applied. It should be also taken into account that the lowest costs of machining (amount 1000.38 PLN/m^2) are incurred if the suspension water jet supplied with silica sand was applied [1, 3, 5].

4. Conclusions

From the optimisation results analysis respecting the different criteria for minimising the costs the following conclusions, more general in character, could be drawn:

• The abradant costs incurred while cutting different work materials (metal, nonmetal and rock) are similar in character. An increase in water pressure is found to cause a decrease in the costs of materials, where their level depends mainly on properties of work material. Whereas, a change in the abradant consumption is parabolic in shape allowing the abradant costs to be optimised, which minimum values mostly occur at the abradant consumption of the order of 60–70 g/s.

• Respecting the abradant consumption costs, the longer abrasive nozzles (75 mm) for which an optimum diameter amounts to 2.25 mm are more favourable. The same conclusions could be also drawn from analysis of the total costs of cutting processes using the suspension water jet.

• The costs of abradant consumption in the suspension hybrid water jet are about 20–30% lower than in case of the suspension water jet applied under similar process conditions. However, if the costs of the other jet components were included, it would lead a rapid increase in the costs of the hybrid water jet with addition of Super-Water polymeric emulsion, which impinges on the final costs of cutting processes.

• The cost index for abrasive material in case of the hybrid water jet does not reflect the real economic aspects showing the costs on the level similar to the abrasive-water jet. The index of the unit costs of cutting process, expressed by complex formula (3), shows the more real state. The calculation results obtained from this relation reveal how high costs are incurred by the application of the hybrid jet.

• The application of high-efficient synthetic abradant instead of silica sand causes all the material costs of suspension abrasive-water jet to be considerably higher.

• All the types of the high-pressure suspension jet with polymer components are very expensive. Therefore using of poly-fluidal and poly-hartenol occurs to be unprofitable.

• Therefore, respecting all the above aspects it should be stated that the processes of cutting with the suspension water jet created according to BorJet's system are the most favourable if the abradant is admixed exclusively with silica sand #30.

References

[1] Borkowski J.: *Materials cutting with abrasive suspension jet using BorJet system*, International Symposium on Unconventional HydroJetting Technologies, Koszalin, 2007, pp. 129–136.

[2] Borkowski J.: *Possibility of rock cutting with hydroabrasive BorJet*, Convegno Internazionale su Situazione e Prospettive del'Industria Lapidea, Cagliari, 1988.

[3] Borkowski J., Borkowski P.: *Optimization of material cutting with abrasive suspension jet*, Advances in Manufacturing Science and Technology, Vol. 28, No. 2, 2004, pp. 49–59.

[4] Borkowski J., et all: *Conception and construction of BorJet suspension jet system*, Report CPBP 02.04.15. Koszalin, 1988.

[5] Borkowski P., Borkowski J.: *Economical aspects of materials cutting with abrasive suspension jet*, 8th Pacific Rim Int. Conf. on Water Jet Technology, Quingdao, 2006, pp. 275–281.

[6] Brandt S., Louis H.: *Controlling of high-pressure abrasive water suspension jets*, 15th International Conference on Jetting Technology, Ronneby, Sweden, 2000, pp. 21–33.

[7] Brandt C., Louis H., Meier G., Tebbing G.: *Abrasive suspension jets at working pressures up to 200 MPa*, 12th Int. Symp. Jet Cutting Technology, Rouen, 1994, No. 41.

[8] Brandt C., Louis H., Ohlsen J., Tebbing G.: *Process control of abrasive water suspension jets*, 13th International Conference on Jetting Technology, Sardinia, Italy, 1996, pp. 563–581.

[9] Fairhurst R.M., Heron R.A., Saunders D.H.: *"DIAJET" – a new abrasive water jet cutting technique*, 8th Int. Symp. Jet Cutting Technology, Durham, 1986, Paper H2, pp. 395–402.

[10] Kiyoshige M., Matsumura H., Ikemoto Y., Okada T.: *A study of abrasive waterjet cutting using slurred abrasives*, 9th International Symposium on Jet Cutting Technology, Sendai, 1988, Paper B2, pp. 61–73.

[11] Lju B.-L., Shang Y., Yao H. F., Zhang F.: *The recent PREMAJET advance in cutting & derusting technology*, 11th Int. Conf. Jet Cutting Technology, St. Andrews, 1992, pp. 451–460.

[12] Quingweng Y., Zhengfang L., Lin Y., Aihua F.: *Flow dynamic abort underwater DIAJet*, 13th International Conference on Jetting Technology, Sardynia, 1996, pp. 299–306.

[13] Zhang H., You M.Q., Wang Y.L., Cui M.S.: *Study on the DIAJET system and its cutting effect*, 4th Pacific Rim Int. Conf. on Water Jet Technology, Kajima, 1995, pp. 273–282.

Kryteria efektywnego przecinania materiałów zawiesinową strugą wodno-ścierną

W artykule omówiono kryteria optymalizacji procesu przecinania materiałów oryginalną metodą BorJet, która pozwala na wytwarzanie zawiesinowej strugi wodno-ściernej oraz zawiesinowej strugi hybrydowej. Przedstawiono wyniki badań optymalizacyjnych przeprowadzonych w oparciu o kryteria minimalizacji kosztów użycia ścierniwa i sumarycznych kosztów obróbki.

Stochastic response analysis of suspension bridge under gusty wind with time-dependent mean velocity

D. BRYJA

Wrocław University of Technology, Wybrzeże Wyspiańskiego 27, 50-370 Wrocław, Poland

The paper presents a general outline of the method of stochastic response analysis of suspension bridge subjected to randomly fluctuated wind with time-dependent mean velocity. The proposed method is aimed to examine how the repeatable wind gusts affect bridge vibrations and to investigate amplified bridge response in resonant regimes. First, a non-homogeneous wind velocity model and associated buffeting forces are developed. The buffeting forces are derived under the general assumption that their spanwise correlation is the same as that of incoming wind fluctuations. Next, a bridge deck is divided into sections along span, and the dynamic bridge response is obtained with neglecting structure nonlinearities, by summing up component responses due to sectional buffeting forces. For the correlation response analysis an analytical time-domain approach based on stochastic calculus is suggested. The mean function and covariance function of bridge response are derived in the general case where in-time correlation of wind velocity fluctuations results from a given wind spectrum. Additionally, for a tentative estimation, two approximate formulas for variance of bridge response are obtained using two opposing mathematical idealizations of wind correlation in time. In the last part, numerical application of the proposed procedure is presented and advantages in bridge engineering are discussed.

Keywords: *suspension bridge, aerodynamics, non-homogeneous wind model, buffeting response, stochastic analysis, resonant buffeting effects*

1. Introduction

Suspension bridges are unique for their slenderness and long spans, which results in high susceptibility to wind-induced vibrations. Depending on the wind speed, different types of aerodynamic phenomena can be observed, for instance – vortex shedding, buffeting or flutter instability [1]. In this paper the attention will be focused on the buffeting phenomenon which is defined as "*the unsteady loading of a structure by velocity fluctuations in the oncoming flow*" [2]. This loading varies randomly in time and space, hence the buffeting response analysis is performed in terms of stochastic aerodynamics.

Extensive studies on buffeting problem in bridge engineering have been published in the literature – see, for example References [2–8] and the references cited therein. In polish literature, the buffeting is discussed for instance by Flaga [9–11]. Analyses of the researchers' achievements show that two general approaches are now available for the buffeting response analysis: (i) frequency-domain (spectral) approach and (ii) time-domain approach. In both cases, wind velocity is treated, in general, as stationary Gaussian stochastic process [4].

Frequency-domain approach is usually applied to analytical investigations, and it offers computational efficiency mainly due to well handling of unsteady aerodynamic forces that are functions of frequency. However, the results of spectral analysis are limited to the standard-derivative buffeting response [5]. Actual time history of the buffeting response can not be obtained instantly, and the variation of turbulent wind along the bridge, if any, can not be analyzed (quoted from Boonyapinyo et al. [3]). Therefore, in most reported recent wind-load studies of long span bridges, the time-domain approach is preferred [3, 5–7]. It seems more appropriate when including nonlinearities of structural and aerodynamic origins, and it enables to predict the buffeting response while simulating fluctuating wind velocities along the bridge [5].

First, the time-domain approach was based on quasi-steady aerodynamics in which buffeting forces were expressed using the static aerodynamic coefficients. Thus, the frequency dependent characteristics of unsteady aerodynamic forces were ignored in the numerical schemes [5]. Recently, the time-domain approach has been extended by introducing rational function approximation of frequency-dependent aerodynamic characteristics, such as admittance function, span-wise coherence and flutter derivatives [6]. Rational function representation allows to include unsteady buffeting forces as well as self-excited forces into buffeting response analysis.

Time-domain approach opens the possibility to consider the buffeting problem due to time-dependent wind velocity with superimposed random fluctuation. Then, it becomes possible to investigate resonant amplification effects induced by wind velocity fluctuations which can occur in flexible structures such as long span suspension bridges [2]. To analyze amplified bridge vibrations in resonant regime, the mean value of wind velocity should be considered as periodically time-dependent. Stochastic response analysis of suspension bridge under such a case of aerodynamic excitation is a subject of this article in which the unique analytical time-domain approach based on stochastic calculus is suggested to obtain the mean function and covariance function of random bridge response. In the first part of the study, non-homogeneous stochastic model of buffeting excitation is developed. As the mean wind velocity is assumed as periodically time-dependent, the model enables to examine how the repeatable wind gusts affect the bridge vibrations and to investigate amplified bridge response in resonant regime. The second part of this paper is devoted to the method of correlation analysis of suspension bridge response. First, the equations of motion of a bridge are derived by using the continuous analytical approach developed by Bryja [12, 13] with the application of standard Galerkin's procedure. Similar approach was applied in [14–17] to investigate different problems of suspension bridge dynamics. Next, neglecting structure nonlinearities, the buffeting bridge response is obtained as a sum of component solutions due to sectional, uniformly distributed, buffeting forces acting on bridge deck sections. These component solutions are expressed by impulse response functions calculated for the considered continuous system. Applying the theory of random processes, the mean function and covariance function of random bridge response are derived in the general case where time correlation of wind velocity fluctuations

results from a given wind spectrum. Additionally, two opposing mathematical idealizations of time correlation are suggested to obtain approximate formulas for a tentative estimation of the variance of bridge response. In the last part of the study a numerical application of the method is presented and advantages in bridge engineering are discussed.

2. Non-homogeneous stochastic model of buffeting excitation

Long span suspension bridges are recognized as flexible structures susceptible to wind-induced vibrations. Such structures "*may exhibit resonant amplification effects induced by velocity fluctuations*" [2]. However, in the standard approach to buffeting problem in bridge engineering, the amplified resonant structure response can not be investigated. It results from the assumption that the along-wind velocity $U(x, t) = \overline{U} + \hat{u}(x, t)$ acting on a bridge deck at a given cross-section x is a sum of a steady mean value $\overline{U}$ and random fluctuation $\hat{u}(x, t)$ which is described by homogeneous stochastic process [2–8]. In this paper, the above wind model is expanded by including the additional periodic term $\overline{u}(t)$ that modifies the mean value of wind velocity so that the resonant vibration analysis could be feasible. Hence, the along-wind velocity is defined as

$$U(x, t) = \overline{U} + \overline{u}(t) + \hat{u}(x, t), \tag{1}$$

and it constitutes a non-homogeneous stochastic process which mean value (mean function) depends on time and amounts $E[U(x, t)] = \overline{U} + \overline{u}(t)$ where $E[\cdot]$ denotes expectation. The periodic term $\overline{u}(t)$ is treated here as the leading component of wind velocity fluctuations which emerges when the bridge exhibits resonant effects. On account of its leading role, the fluctuation component $\overline{u}(t)$ is assumed as not random and not varying along bridge span. Time-and-space dependent term $\hat{u}(x, t)$ describes random velocity fluctuation which forms a zero-mean homogeneous Gaussian process, similarly as in the standard wind model.

The periodic component $\overline{u}(t)$ could be taken simply as harmonic one, like as in [18]. However, in this study the more general case is considered where

$$\overline{u}(t) = \sum_{i=0}^{v} \lambda \overline{U} P_T(t - t_i), \qquad P_T(t - t_i) = \begin{cases} 0 & \text{for } t < t_i \text{ and } t > t_i + T \\ P(t - t_i) & \text{for } t_i \leq t \leq t_i + T \end{cases}. \tag{2}$$

Here, the function $\overline{u}(t)$ describes a series of repeatable wind gusts occurring at regular intervals Δ, at times $t_i = i\Delta$. Function $P(t - t_i)$ defines gust time-shape, $T \leq \Delta$ denotes gust duration, $\lambda = \max_t[\overline{u}(t)]/\overline{U}$ is the scale ratio, v is the number of gusts

occurred until time t, $v \Delta \leq t < (v + 1) \Delta$. Defined in such a way the wind velocity model can have different applications. Taking $\lambda = 0$ we can get the standard wind model with a steady mean velocity. Assuming that the periodic series of repeatable gusts (2) constitutes harmonic function with the frequency close to natural frequency of bridge vibrations, we can describe fluctuating wind which causes resonant buffeting effects. Also, setting in formulae (2) the gust characteristics λ, T, Δ and $P(t - t_i)$, we can define an arbitrary series of repeatable long-duration large-scale gusts with superimposed random fluctuation. Moreover, limiting the periodic series (2) to a single gust, we can describe the wind acting over the time T and characterized by any given time-dependent mean velocity expressed as $\overline{U} + \overline{u}(t) = \overline{U}[1 + \lambda P(t - t_0)]$ where t_0 is the initial time and $t_0 \leq t \leq t_0 + T$.

Along-wind velocity defined by formulae (1) and (2) forms time-and-space dependent continuous stochastic process. It is quite complicated problem to find a buffeting solution in this case, especially for long span suspension bridges. Therefore, some expedient simplifications are suggested in this paper. Bridge deck is divided into n sections along its span, as it is shown in Figure 1 where x_j^s denotes the coordinate of section midpoint, d_j^s is the section length, $j = 1...n$. The spectrum of wind velocity is approximately taken as not varying along given deck section, and finally, the continuous random process $\hat{u}(x, t)$ is replaced by a set of zero-mean homogeneous processes $\hat{u}_j(t) = \hat{u}(x_j, t)$ constituting multivariate stochastic process $\hat{\mathbf{u}}(t)$ with n components $\hat{u}_j(t)$.
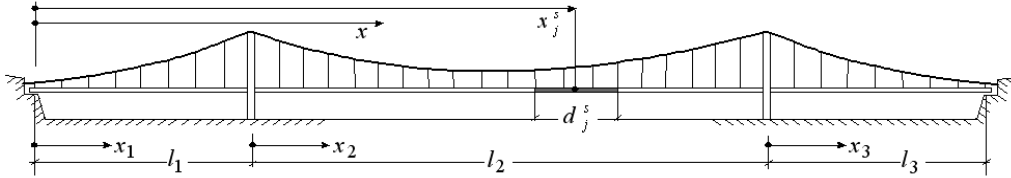
Fig. 1. Location of a bridge deck section and sectional wind load

Assuming that the wind spectra of all points x_j^s on the bridge deck are the same (that is, the random wind fluctuations $\hat{u}_j(t)$ are of the same type), we have

$$S_{\hat{u}_1 \hat{u}_1}(\omega) = S_{\hat{u}_2 \hat{u}_2}(\omega) = \ldots = S_{\hat{u}_n \hat{u}_n}(\omega) = S(\omega). \tag{3}$$

Then, we can obtain autocorrelations of random processes $\hat{u}_j(t)$ as

$$K_{\hat{u}_j \hat{u}_j}(\tau) = C_{\hat{u}_j \hat{u}_j}(\tau) = 2\int_0^\infty S_{\hat{u}_j \hat{u}_j}(\omega)\cos \omega\tau \, d\omega = 2\int_0^\infty S(\omega)\cos \omega\tau \, d\omega, \tag{4}$$

on the basis of widely known relationship between covariance $C_{\hat{u}_j \hat{u}_j}(\tau)$ and spectral density function $S_{\hat{u}_j \hat{u}_j}(\omega)$, where $\tau = t_1 - t_2$ [19], [20]. For zero-mean homogeneous processes $\hat{u}_j(t)$, autocorrelation $K_{\hat{u}_j \hat{u}_j}(\tau)$ is equal to covariance.

As the correlation between wind turbulence acting on two different bridge sections decreases when the distance between deck sections grows, we should modify cross-spectral densities by introducing the coherence function as follows [4]

$$S_{\hat{u}_j \hat{u}_k}(\omega) = \sqrt{S_{\hat{u}_j \hat{u}_j}(\omega) S_{\hat{u}_k \hat{u}_k}(\omega)}\, \mathrm{coh}(\delta_{jk}, \omega) = S(\omega)\mathrm{coh}(\delta_{jk}, \omega), \qquad \delta_{jk} = \left| x_j - x_k \right|. \quad (5)$$

Then, cross-correlations are given by

$$K_{\hat{u}_j \hat{u}_k}(\tau) = C_{\hat{u}_j \hat{u}_k}(\tau) = 2\int_0^\infty S_{\hat{u}_j \hat{u}_k}(\omega)\cos \omega\tau\, d\omega = 2\int_0^\infty S(\omega)\mathrm{coh}(\delta_{jk}, \omega)\cos\omega\tau\, d\omega, \quad (6)$$

where $j, k = 1\ldots n$, $j \neq k$. The coherence function can be expressed by the following relation

$$\mathrm{coh}(\delta_{jk}, \omega) = \exp\left(-\frac{\lambda_c \omega \delta_{jk}}{2\pi \overline{U}(z)} \right), \quad (7)$$

based on the model suggested by Davenport, where z is the height of deck above ground, $\overline{U}(z)$ is the average wind velocity on the deck and λ_c is usually between 7 and 10 [4]. Wind spectrum $S(\omega)$ is commonly modeled by Kaimal's spectral density function which is given for horizontal wind velocity by

$$\frac{nS(n)}{U_*^2} = \frac{200f}{(1+50f)^{5/3}}, \quad n = \omega/2\pi, \quad f = nz/\overline{U}(z), \quad U_* = K\overline{U}(z)/\ln(z/z_0), \quad (8)$$

where:

z_0 is the ground roughness ratio, $K = 0.4$ [4].

To formulate aerodynamic force model related to the wind velocity defined by Equations (1) and (2), the fundamental buffeting problem where $\overline{u}(t) = 0$ should be considered as the first one. Aerodynamic loads on a bridge deck (Figure 2) are represented by three components: drag (F_D), lift (F_L) and moment (F_M) forces acting at the effective centre of rotation (i.e. shear centre of a deck cross-section [8]). For a steady mean velocity, aerodynamic forces caused by fluctuating wind are expressed per unit span by the following well known formulae [5]

$$F_D(x,t) = \frac{1}{2}\rho\overline{U}^2 B\left(C_D\chi_{Du}\left[1+2\frac{\hat{u}(x,t)}{\overline{U}}\right]+C_D'\chi_{Dw}\frac{\hat{w}(x,t)}{\overline{U}}\right),\tag{9}$$

$$F_L(x,t) = -\frac{1}{2}\rho\overline{U}^2 B\left(C_L\chi_{Lu}\left[1+2\frac{\hat{u}(x,t)}{\overline{U}}\right]+(C_L'+C_D)\chi_{Lw}\frac{\hat{w}(x,t)}{\overline{U}}\right),\tag{10}$$

$$F_M(x,t) = \frac{1}{2}\rho\overline{U}^2 B^2\left(C_M\chi_{Mu}\left[1+2\frac{\hat{u}(x,t)}{\overline{U}}\right]+C_M'\chi_{Mw}\frac{\hat{w}(x,t)}{\overline{U}}\right),\tag{11}$$

where:

  $\hat{w}(x, t)$ is the cross-wind velocity fluctuation,

  C_D, C_L, C_M denote mean (static) drag, lift and moment coefficients,

  $C_D' = dC_D/d\alpha$, $C_L' = dC_L/d\alpha$, $C_M' = dC_M/d\alpha$, and χ_{Du}, χ_{Dw}, χ_{Lu}, χ_{Lw}, χ_{Mu},
χ_{Mw} are frequency dependent admittance functions.
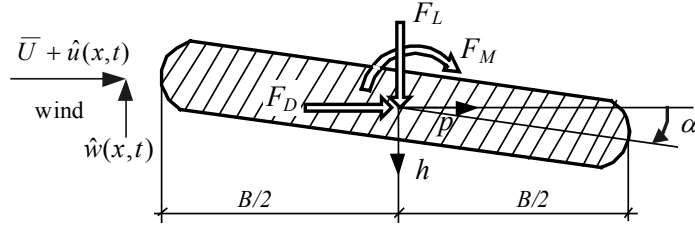
Fig. 2. Aerodynamic loads and displacements at a bridge cross-section

Buffeting forces due to the gusty wind with time-dependent mean velocity can be written in an analogical form given by

$$D(x,t) = \frac{1}{2}\rho[\overline{U}+\overline{u}(t)]^2 B\left[C_D\chi_{Du}\left(1+2\frac{\hat{u}(x,t)}{\overline{U}+\overline{u}(t)}\right)+C_D'\chi_{Dw}\left(\frac{\hat{w}(x,t)}{\overline{U}+\overline{u}(t)}\right)\right],\tag{12}$$

$$L(x,t) = -\frac{1}{2}\rho[\overline{U}+\overline{u}(t)]^2 B\left[C_L\chi_{Lu}\left(1+2\frac{\hat{u}(x,t)}{\overline{U}+\overline{u}(t)}\right)+(C_L'+C_D)\chi_{Lw}\left(\frac{\hat{w}(x,t)}{\overline{U}+\overline{u}(t)}\right)\right],\tag{13}$$

$$M(x,t) = \frac{1}{2}\rho[\overline{U}+\overline{u}(t)]^2 B^2\left[C_M\chi_{Mu}\left(1+2\frac{\hat{u}(x,t)}{\overline{U}+\overline{u}(t)}\right)+C_M'\chi_{Mw}\left(\frac{\hat{w}(x,t)}{\overline{U}+\overline{u}(t)}\right)\right].\tag{14}$$

To substantiate the above formulae let us consider a simple load case when the wind acts on a small hypothetical point-like structure with the area A perpendicular to the

mean wind direction [8]. Neglecting in-wind structure motion, the along-wind load (drag force) gathered from surface A amounts

$$F_D(t) = \frac{1}{2}\rho U^2(t)AC_D = \frac{1}{2}\rho AC_D[\overline{U} + \hat{u}(t)]^2 \cong \frac{1}{2}\rho AC_D[\overline{U}^2 + 2\overline{U}\hat{u}(t)], \tag{15}$$

$$D(t) = \frac{1}{2}\rho U^2(t)AC_D = \frac{1}{2}\rho AC_D[\overline{U} + \overline{u}(t) + \hat{u}(t)]^2 =$$
$$\cong \frac{1}{2}\rho AC_D\left([\overline{U} + \overline{u}(t)]^2 + 2[(\overline{U} + \overline{u}(t)]\hat{u}(t)\right), \tag{16}$$

in two considered cases, respectively. In both cases the term $[\hat{u}(t)]^2 [\hat{u}(t)]^2$ is neglected as much smaller than the other terms. For the cross-section x of a bridge deck with the width B, Equations (15) and (16) can be rewritten as

$$F_D(x,t) = \frac{1}{2}\rho BC_D\overline{U}^2\left(1 + 2\frac{\hat{u}(x,t)}{\overline{U}}\right), \tag{17}$$

$$D(x,t) = \frac{1}{2}\rho BC_D[\overline{U} + \overline{u}(t)]^2\left(1 + 2\frac{\hat{u}(x,t)}{\overline{U} + \overline{u}(t)}\right). \tag{18}$$

Introducing the cross-wind turbulence component $\hat{w}(x, t)$ and admittance functions into Equation (17) one obtains commonly known drag force (9). Newly formulated drag force (12) can be obtained analogically, on the basis of Equation (18). Lift and moment buffeting forces, (13) and (14), can be justified in the same way.

In subsequent parts of this study, all buffeting components related to the cross-wind turbulence $\hat{w}(x, t)$ will be omitted for brevity, and admittance functions will be taken as equal unity. The neglected effects can be taken into account in the way presented in [18] where a bit simpler wind model has been formulated and employed to buffeting response analysis of cable-stayed bridge.

On the basis of above assumptions, we can divide buffeting forces (12–14) into sectional forces uniformly distributed within j-th deck section:

$$D_j^s(t) = \rho BC_D f_j(t), \; L_j^s(t) = -\rho BC_L f_j(t), \; M_j^s(t) = \rho B^2 C_M f_j(t), \tag{19}$$

$$f_j(t) = 0.5[\overline{U} + \overline{u}(t)]^2 + [\overline{U} + \overline{u}(t)]\hat{u}_j(t) = \bar{f}(t) + \hat{f}_j(t), \tag{20}$$

where $j = 1...n$.

It reveals that the above drag, lift and moment sectional forces are expressed by the same random function $f_j(t)$. For the sake of convenience of stochastic calculus, this function has been divided into time dependent mean function $\bar{f}(t) = 0.5[\overline{U} + \overline{u}(t)]^2$, the same for all deck sections, and random fluctuation $\hat{f}_j(t) = [\overline{U} + \overline{u}(t)]\hat{u}_j(t)$, specific to the j-th deck section.

3. Equations of motion of suspension bridge

It is assumed that suspension bridge vibrations are described by the equations of motion developed in [12, 13] for structural systems consisting of a bridge deck and two perfectly flexible cables (Figure 1). The bridge model is defined on the basis of the following basic assumptions:

(i) suspended structure is idealized by a set of prismatic thin-walled girders with mono-symmetric closed or open-type cross-section; the girders are simply supported on pylons or bridgeheads and suspended by vertical inextensible hangers to continuous cables;

(ii) cables are anchored at their ends and movable at their supporting points on rigid pylons;

(iii) initial dead load is carried by two cables causing no stresses in the stiffening structure, cables under dead load are of parabolic profile in accordance to the assumption that the total weight of the bridge is uniformly distributed along the span;

(iv) all stresses in bridge follow Hook's law.

When the considerations are limited to suspension bridges with small cable sags, equations governing the motion of i-th bridge span have the following forms, for vertical, lateral and torsional vibrations, respectively:

$$EJ_{yi}\frac{\partial^4 w_i}{\partial x_i^4} - 2H_0\frac{\partial^2 w_i}{\partial x_i^2} + \frac{16k_c f}{l_2^2}\mu_i\sum_{k=1}^{3}\mu_k\int_0^{l_k} w_k\, dx_k - 2H_0\eta_1\frac{\partial^2 w_i}{\partial x_i^2} - 2H_0 e\eta_2\frac{\partial^2 \varphi_i}{\partial x_i^2} +$$

$$\left(m_{bi} + \frac{2m_c}{\cos\beta_{0i}}\right)\frac{\partial^2 w_i}{\partial t^2} = p_{zi}(x_i, t)\,, \tag{21}$$

$$EJ_{zi}\frac{\partial^4 v_i}{\partial x_i^4} + \frac{m_{bi}g}{h_{ci}}v_i - \frac{m_{bi}gc_i}{h_{ci}}\varphi_i + m_{bi}\frac{\partial^2 v_i}{\partial t^2} - m_{bi}b_i\frac{\partial^2 \varphi_i}{\partial t^2} = p_{yi}(x_i, t)\,, \tag{22}$$

$$EJ_{\omega i}\frac{\partial^4 \varphi_i}{\partial x_i^4} - GI_i\frac{\partial^2 \varphi_i}{\partial x_i^2} - 2H_0 e^2\frac{\partial^2 \varphi_i}{\partial x_i^2} + \frac{16k_c fe^2}{l_2^2}\mu_i\sum_{k=1}^{3}\mu_k\int_0^{l_k}\varphi_k\, dx_k\,,$$

$$-2H_0 e^2 \eta_1 \frac{\partial^2 \varphi_i}{\partial x_i^2} - 2H_0 e \eta_2 \frac{\partial^2 w_i}{\partial x_i^2} + m_{bi}g\left(b_i - c_i + \frac{c_i^2}{h_{ci}}\right)\varphi_i - \frac{m_{bi}g c_i}{h_{ci}}v_i +$$

$$\left(j_{\mathrm{B}i} + m_{bi}b_i^2 + \frac{2m_c e^2}{\cos\beta_{0i}}\right)\frac{\partial^2 \varphi_i}{\partial t^2} - m_{bi}b_i\frac{\partial^2 v_i}{\partial t^2} = m_{xi}(x_i,t) \,. \tag{23}$$

Vertical, lateral and torsional displacements w_i $(x_i,\ t)$, v_i $(x_i,\ t)$, φ_i $(x_i,\ t)$, and dynamic loads p_{zi} $(x_i,\ t)$, p_{yi} $(x_i,\ t)$, m_{xi} $(x_i,\ t)$, are referred to the shear centre of stiffening girder cross-section at i-th span. EJ_{yi}, EJ_{zi}, $EJ_{\omega i}$, GI_{yi} are flexural rigidities, warping rigidity and St. Venant torsional rigidity of stiffening girder, m_{bi} denote unit mass, j_{Bi} is mass polar moment of inertia calculated per unit span, g is acceleration of gravity. Vertical coordinates b_i, c_i, measured from the shear centre, determine the location of cross-section mass centre and suspension centre, respectively. The latter one is related to connection points between deck and hangers. $E_c A_c$ and m_c are longitudinal rigidity and unit mass of cable. Cable stiffness and length are described by the coefficients:

$$k_c = (E_c A_c / L_c)(8f / l_2^2) \quad \text{and} \quad L_c = \sum_{i=0}^{3} \int_0^{l_i} \cos^{-3}\beta_{0i} dx_i \,.$$
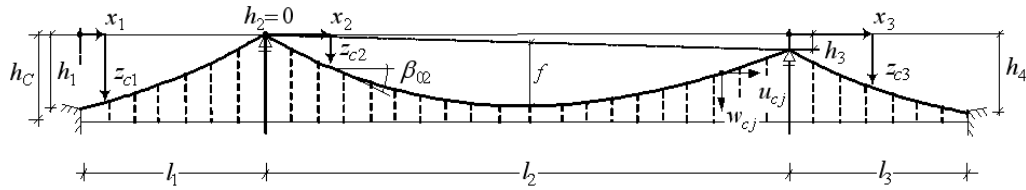
Fig. 3. Cable profile under dead load

Function $h_{ci}(x_i) = h_C - [h_i + (h_{i+1} - h_i)x_i / l_i]$ determines a vertical distance between cable chord and suspension centre, which results from Figure 3 where the cable profile under dead load is presented. This initial static profile is given by a set of parabolic functions $z_{ci}(x_i) = h_i + (h_{i+1} - h_i)x_i / l_i + \mu_i(4f / l_2^2)(l_i x_i - x_i^2)$, where $i = 1, 2, 3$ and $\mu_i = \tilde{m}_i / \tilde{m}_2$ is the ratio of averaged unit mass $\tilde{m}_i$ of a bridge in the i-th span to that in the central span $-\tilde{m}_2$. Initial horizontal component of cable tension, the same for both cables, amounts $H_0 = \tilde{m}_2 g l_2^2 / 16f$. An increment in cable tension due to dynamic load is expressed as $\Delta H_1(t) = H_0[\eta_1(t) - \eta_2(t)]$ for a cable situated on the left side of a bridge cross-section or $\Delta H_2(t) = H_0[\eta_1(t) + \eta_2(t)]$ for that on the right side, where

$$\eta_1(t) = \frac{k_c}{H_0}\sum_{i=1}^{3}\mu_i\int_0^{l_i}w_i dx_i, \quad \eta_2(t) = \frac{ek_c}{H_0}\sum_{i=1}^{3}\mu_i\int_0^{l_i}\varphi_i dx_i. \tag{24}$$

Equations (21–23) can be transformed into a time domain by applying standard Galerkin's procedure with an approximation of bridge displacements given by

$$w_i(x_i, t) = \mathbf{s}_i^{\mathrm{T}} \mathbf{q}_{wi}, \quad v_i(x_i, t) = \mathbf{s}_i^{\mathrm{T}} \mathbf{q}_{vi}, \quad \varphi_i(x_i, t) = \frac{1}{e} \mathbf{s}_i^{\mathrm{T}} \mathbf{q}_{\varphi i}, \tag{25}$$

where:

$\mathbf{s}_i(x_i) = \mathrm{col}(\sin \pi \xi_i, \sin 2\pi \xi_i, \ldots, \sin n_i \pi \xi_i)$, $\xi_i = x_i / l_i$, $i = 1, 2, 3$ and e is the half-distance between cables in a bridge cross-section. In further considerations, the non-linear terms of Equation (21) and (23) have been omitted as not significant for suspension bridges which are numbered among weakly nonlinear structures. After including dissipative forces referred to viscous Rayleigh-type damping, linear equations of motion of the bridge have the following matrix form

$$\mathbf{B}\ddot{\mathbf{q}}(t) + \mathbf{C}\dot{\mathbf{q}}(t) + \mathbf{K}\mathbf{q}(t) = \mathbf{F}(t), \tag{26}$$

where:

the vector $\mathbf{q} = \mathrm{col}(\mathbf{q}_1, \mathbf{q}_2, \mathbf{q}_3)$ assembling Lagrangian coordinates referred to subsequent bridge spans is formed by sub-vectors as follows

$$\mathbf{q}_1 = \mathrm{col}(\mathbf{q}_{w1}, \mathbf{q}_{v1}, \mathbf{q}_{\varphi 1}), \quad \mathbf{q}_2 = \mathrm{col}(\mathbf{q}_{w2}, \mathbf{q}_{v2}, \mathbf{q}_{\varphi 2}), \quad \mathbf{q}_3 = \mathrm{col}(\mathbf{q}_{w3}, \mathbf{q}_{v3}, \mathbf{q}_{\varphi 3}). \tag{27}$$

The over-dot indicates differentiation with respect to time. $\mathbf{B}$, $\mathbf{C}$, $\mathbf{K}$ are mass, damping and stiffness matrices, respectively. Their explicit forms are presented in Appendix I. The excitation vector $\mathbf{F}(t) = \mathrm{col}(\mathbf{F}_1, \mathbf{F}_2, \mathbf{F}_3)$ is an assemblage of the following sub-vectors

$$\mathbf{F}_1 = \mathrm{col}(\mathbf{F}_{w1}, \mathbf{F}_{v1}, \mathbf{F}_{\varphi 1}), \quad \mathbf{F}_2 = \mathrm{col}(\mathbf{F}_{w2}, \mathbf{F}_{v2}, \mathbf{F}_{\varphi 2}), \quad \mathbf{F}_3 = \mathrm{col}(\mathbf{F}_{w3}, \mathbf{F}_{v3}, \mathbf{F}_{\varphi 3}), \tag{28}$$

$$\mathbf{F}_{wi} = \int_0^{l_i} p_{zi} \mathbf{s}_i \, dx_i, \quad \mathbf{F}_{vi} = \int_0^{l_i} p_{yi} \mathbf{s}_i \, dx_i, \quad \mathbf{F}_{\varphi i} = \frac{1}{e} \int_0^{l_i} m_{xi} \mathbf{s}_i \, dx_i, \quad i = 1, 2, 3. \tag{29}$$

Considering uniformly distributed buffeting forces (19) acting on the j-th deck section being a part of the i-th span, one obtains

$$p_{zi}(x_i, t) = L_j^s(t) h_j(x_i), \quad p_{yi}(x_i, t) = D_j^s(t) h_j(x_i), \quad m_{xi}(x_i, t) = M_j^s(t) h_j(x_i), \tag{30}$$

where:

$h_j(x_i)$ is expressed by Heaviside function $\Im(x)$ as follows

$$h_j(x_i) = \Im[x_i + L_{i-1} - (x_j^s - 0.5d_j^s)] - \Im[x_i + L_{i-1} - (x_j^s + 0.5d_j^s)]. \tag{31}$$

Partial sum of span lenghts L_{i-1} amounts $L_0 = 0$, $L_1 = l_1$, $L_2 = l_1 + l_2$ for $i = 1, 2, 3$, respectively (Figure 1). Substituting (30) into (29) yields

$$\mathbf{F}_{wi} = L_j^s(t) \int_{a_j}^{b_j} \mathbf{s}_i(x_i)dx_i = -\rho B C_L f_j(t) l_i \mathbf{d}_i^{-1}[\mathbf{c}_i(a_j) - \mathbf{c}_i(b_j)] = \mathbf{f}_{wij}^s f_j(t), \tag{32}$$

$$\mathbf{F}_{vi} = D_j^s(t) \int_{a_j}^{b_j} \mathbf{s}_i(x_i)dx_i = \rho B C_D f_j(t) l_i \mathbf{d}_i^{-1}[\mathbf{c}_i(a_j) - \mathbf{c}_i(b_j)] = \mathbf{f}_{vij}^s f_j(t), \tag{33}$$

$$\mathbf{F}_{\varphi i} = M_j^s(t) \frac{1}{e} \int_{a_j}^{b_j} \mathbf{s}_i(x_i)dx_i = \rho B^2 C_M f_j(t) \frac{l_i}{e} \mathbf{d}_i^{-1}[\mathbf{c}_i(a_j) - \mathbf{c}_i(b_j)] = \mathbf{f}_{\varphi ij}^s f_j(t), \tag{34}$$

when $L_{i-1} < x_j^s < L_i$ and otherwise $\mathbf{F}_{wi} = \mathbf{0}$, $\mathbf{F}_{vi} = \mathbf{0}$, $\mathbf{F}_{\varphi i} = \mathbf{0}$, $i = 1, 2, 3$. In the above relationships the following notation is used: $\mathbf{c}_i(x_i) = [\cos\pi\xi_i, \cos 2\pi\xi_i, \ldots, \cos n_i\pi\xi_i]^T$, $\mathbf{d}_i = \text{diag}(\pi, 2\pi, \ldots, n_i\pi)$, $a_j = (x_j^s - 0.5d_j^s) - L_{i-1}$, $b_j = (x_j^s + 0.5d_j^s) - L_{i-1}$.

Sub-vectors (32−34) constitute the excitation vector $\mathbf{F}_j^s(t)$ due to sectional buffeting forces. It can be written as a product of constant vector $\mathbf{f}_j^s$ and time dependent random function $f_j(t)$. The total vector of generalized excitation forces is a sum of component vectors as follows

$$\mathbf{F}(t) = \sum_{j=1}^n \mathbf{F}_j^s(t) = \sum_{j=1}^n \mathbf{f}_j^s f_j(t). \tag{35}$$

4. Buffeting bridge response

Let $R(t)$ denote a bridge response due to buffeting excitation, e.g. cable force, displacement or stress at any point of bridge cross-section. When the structure nonlinearities are omitted, every bridge response is a result of linear transformation of generalized coordinates and the buffeting bridge response can be calculated as a sum of component responses $R_j(t)$ due to sectional excitations $\mathbf{F}_j^s(t)$. The component response can be expressed as $R_j(t) = \mathbf{a}_R^T\mathbf{q}$, where $\mathbf{q}$ is a solution of equation of motion written in the form

$$\mathbf{B}\ddot{\mathbf{q}} + \mathbf{C}\dot{\mathbf{q}} + \mathbf{K}\mathbf{q} = \mathbf{f}_j^s f_j(t), \tag{36}$$

and the constant vector $\mathbf{a}_R$ transforms coordinates $\mathbf{q}$ into the examined response $R(t)$. As a right-hand side of the equation of motion (36) is a product of constant vector $\mathbf{f}_j^s$ and time-dependent function $f_j(\mathrm{t})$, the component response $R_j(t)$ can be obtained by summing up the elementary solutions due to differential impulses $f_j(\tau)d\tau$ as follows

$$R_j(t) = \int_0^t H_{Rj}(t - \tau) f_j(\tau) d\tau. \tag{37}$$

Function $H_{Rj}(t)$ has the same meaning as the impulse response function of SDOF systems – it is the response $R_j(t)$ due to the unit impulsive load. Then we have $H_{Rj}(t - \tau) = \mathbf{a}_R^\mathrm{T} \mathbf{q}_{imp}$ where $\mathbf{q}_{imp}$ is a solution of equation $\mathbf{B}\ddot{\mathbf{q}} + \mathbf{C}\dot{\mathbf{q}} + \mathbf{K}\mathbf{q} = \mathbf{f}_j^s \delta(t - \tau)$ where $\delta(t - \tau)$ denotes Dirac delta function.

Substituting the random function (20) into the Equation (37) yields

$$R_j(t) = \int_0^t H_{Rj}(t - \tau)[\bar{f}(\tau) + \hat{f}_j(\tau)]d\tau = \overline{R}_j(t) + \hat{R}_j(t), \tag{38}$$

$$\overline{R}_j(t) = \frac{1}{2}\int_0^t H_{Rj}(t - \tau)[\overline{U} + \overline{u}(\tau)]^2 d\tau, \;\; \hat{R}_j(t) = \int_0^t H_{Rj}(t - \tau)[\overline{U} + \overline{u}(\tau)]\hat{u}_j(\tau)d\tau. \tag{39}$$

The total bridge response is a sum of component solutions (38), that is

$$R(t) = \sum_{j=1}^n \overline{R}_j(t) + \sum_{j=1}^n \hat{R}_j(t). \tag{40}$$

5. Correlation analysis of buffeting bridge response

It reveals from zero-mean distinctive of wind fluctuations $\hat{u}_j(t)$ that expected values $\mathrm{E}[\hat{R}_j(t)]$ of random response fluctuations are equal to zero. Hence, the expectation of stochastic bridge response (40) yields

$$\mathrm{E}[R(t)] = \sum_{j=1}^n \overline{R}_j(t) =$$

$$\frac{1}{2}\overline{U}^2\sum_{j=1}^{n}\left(\int_0^t H_{Rj}(t-\tau)d\tau + \sum_{i=0}^{v-1}\int_{t_i}^{t_i+T}H_{Rj}(t-\tau)P(\tau-t_i)[2\lambda+\lambda^2 P(\tau-t_i)]\,d\tau + \right.$$

$$\left.\int_{t_v}^{t}H_{Rj}(t-\tau)P(\tau-t_v)[2\lambda+\lambda^2 P(\tau-t_v)]\,d\tau\right), \tag{41}$$

when $v\varDelta \le t \le v\varDelta + T$ or

$$\mathrm{E}[R(t)] = \sum_{j=1}^{n}\overline{R}_j(t) =$$

$$\frac{1}{2}\overline{U}^2\sum_{j=1}^{n}\left(\int_0^t H_{Rj}(t-\tau)d\tau + \sum_{i=0}^{v}\int_{t_i}^{t_i+T}H_{Rj}(t-\tau)P(\tau-t_i)[2\lambda+\lambda^2 P(\tau-t_i)]\,d\tau\right), \tag{42}$$

when $v\varDelta + T < t < (v+1)\,\varDelta$, where v is the number of T-duration wind gusts occurred until time t (cf. Equation (2)).

Regarding that $\mathrm{E}[\hat{R}_j(t)] = 0$, it can be proved that the covariance function of bridge response satisfies the following relation

$$C_{RR}(t_1,t_2) = \mathrm{E}[R(t_1)R(t_2)] - \mathrm{E}[R(t_1)]\mathrm{E}[R(t_2)] =$$

$$\mathrm{E}\left[\sum_{j=1}^{n}\hat{R}_j(t_1)\cdot\sum_{k=1}^{n}\hat{R}_k(t_2)\right] = \sum_{j=1}^{n}\sum_{k=1}^{n}\mathrm{E}[\hat{R}_j(t_1)\hat{R}_k(t_2)]. \tag{43}$$

It means that the covariance function is a sum of all cross-correlations $K_{\hat{R}_j\hat{R}_k}(t_1,t_2) = \mathrm{E}[\hat{R}_j(t_1)\hat{R}_k(t_2)]$ which constitute the correlation matrix of multivariate stochastic process $\hat{\mathbf{R}}(t)$ consisting of the n components $\hat{R}_j(t)$. The cross-correlations obtained on the basis of Equation (39) with Equation (2) being introduced are given by

$$K_{R_jR_k}(t_1,t_2) = \overline{U}^2\int_0^{t_2}\int_0^{t_1}H_{jk}(t_1,t_2,\tau_1,\tau_2)K_{\hat{u}_j\hat{u}_k}(\tau_1,\tau_2)d\tau_1 d\tau_2 +$$

$$\lambda\overline{U}^2\sum_{i_2=0}^{v_2-1}\int_{t_{i_2}}^{t_{i_2}+T}\int_0^{t_1}H_{jk}K_{\hat{u}_j\hat{u}_k}P(\tau_2-t_{i_2})d\tau_1 d\tau_2 + \lambda\overline{U}^2\int_{t_{v_2}}^{t_2}\int_0^{t_1}H_{jk}K_{\hat{u}_j\hat{u}_k}P(\tau_2-t_{v_2})d\tau_1 d\tau_2 +$$

$$\lambda\overline{U}^2\sum_{i_1=0}^{v_1-1}\int_{t_{i_1}}^{t_{i_1}+T}\int_0^{t_2}H_{jk}K_{\hat{u}_j\hat{u}_k}P(\tau_1-t_{i_1})d\tau_2 d\tau_1 + \lambda\overline{U}^2\int_{t_{v_1}}^{t_1}\int_0^{t_2}H_{jk}K_{\hat{u}_j\hat{u}_k}P(\tau_1-t_{v_1})d\tau_2 d\tau_1 +$$

$$\lambda^2 \overline{U}^2 \sum_{i_1=0}^{v_1-1} \sum_{i_2=0}^{v_2-1} \int_{t_{i_2}}^{t_{i_2}+T} \int_{t_{i_1}}^{t_{i_1}+T} H_{jk} K_{\hat{u}_j \hat{u}_k} P(\tau_1 - t_{i_1}) P(\tau_2 - t_{i_2}) d\tau_1 d\tau_2 +$$

$$\lambda^2 \overline{U}^2 \sum_{i_2=0}^{v_2-1} \int_{t_{i_2}}^{t_{i_2}+T} \int_{t_{v_1}}^{t_1} H_{jk} K_{\hat{u}_j \hat{u}_k} P(\tau_2 - t_{i_2}) P(\tau_1 - t_{v_1}) d\tau_1 d\tau_2 +$$

$$\lambda^2 \overline{U}^2 \sum_{i_1=0}^{v_1-1} \int_{t_{i_1}}^{t_{i_1}+T} \int_{t_{v_2}}^{t_2} H_{jk} K_{\hat{u}_j \hat{u}_k} P(\tau_1 - t_{i_1}) P(\tau_2 - t_{v_2}) d\tau_2 d\tau_1 +$$

$$\lambda^2 \overline{U}^2 \int_{t_{v_2}}^{t_2} \int_{t_{v_1}}^{t_1} H_{jk} K_{\hat{u}_j \hat{u}_k} P(\tau_1 - t_{v_1}) P(\tau_2 - t_{v_2}) d\tau_1 d\tau_2, \tag{44}$$

where:

$$H_{jk} = H_{jk}(t_1, t_2, \tau_1, \tau_2) = H_{Rj}(t_1 - \tau_1) H_{Rk}(t_2 - \tau_2), \quad K_{\hat{u}_j \hat{u}_k} = K_{\hat{u}_j \hat{u}_k}(\tau_1, \tau_2) \text{ and } v_1 \Delta \leq$$

$t_1 \leq v_1 \Delta + T$, $v_2 \Delta \leq t_2 \leq v_2 \Delta + T$. All integrals $\int_{t_{v1}}^{t_1} ... d\tau_1$ are equal to zero when $v_1 \Delta + T <$ $t_1 < (v_1 + 1)\Delta$, and then, the upper sum limit "$v_1 - 1$" amounts v_1. Similarly, if $v_2 \Delta + T < t_2 < (v_2 + 1)\Delta$, then $\int_{t_{v2}}^{t_2} ... d\tau_2$ and "$v_2 - 1$" is v_2. Double integrals appearing in Equation (44) can be obtained in a numerical way only because the impulse response functions $H_{Rj}(t - \tau)$ are not given in an analytical form – their ordinates in subsequent time points result from numerical integration of equation of motion.

From the practical viewpoint it is worthwhile to obtain the variance of random buffeting response. The variance results directly from covariance function (43) written for $t_1 = t_2 = t$ [19, 20]. In this case $v_1 = v_2 = v$ and then we have

$$\sigma_R^2 = C_{RR}(t,t) = \sum_{j=1}^{n} \sum_{k=1}^{n} K_{\hat{R}_j \hat{R}_k}(t,t), \tag{45}$$

where cross-correlations of component bridge responses are expressed as

$$K_{R_j R_k}(t,t) = \overline{U}^2 \int_0^t \int_0^t H_{jk} K_{\hat{u}_j \hat{u}_k} d\tau_1 d\tau_2 + \lambda \overline{U}^2 \sum_{i=0}^{v-1} \int_{t_i}^{t_i+T} \int_0^t (H_{jk} + H_{kj}) K_{\hat{u}_j \hat{u}_k} P(\tau_2 - t_i) d\tau_1 d\tau_2 +$$

$$\lambda \overline{U}^2 \int_{t_v}^t \int_0^t (H_{jk} + H_{kj}) K_{\hat{u}_j \hat{u}_k} P(\tau_2 - t_v) d\tau_1 d\tau_2 +$$

$$\lambda^2 \overline{U}^2 \sum_{i=0}^{v-1} \int_{t_i}^{t_i+T} \int_{t_v}^t (H_{jk} + H_{kj}) K_{\hat{u}_j \hat{u}_k} P(\tau_1 - t_i) P(\tau_2 - t_v) d\tau_2 d\tau_1 +$$

$$\lambda^2 \overline{U}^2 \sum_{i=0}^{v-1} \sum_{i=0}^{v-1} \int_{t_i}^{t_i+T} \int_{t_i}^{t_i+T} H_{jk} K_{\hat{u}_j \hat{u}_k} P(\tau_1 - t_i) P(\tau_2 - t_i) d\tau_1 d\tau_2 +$$

$$\lambda^2 \overline{U}^2 \int_{t_v}^{t} \int_{t_v}^{t} H_{jk} K_{\hat{u}_j \hat{u}_k} P(\tau_1 - t_v) P(\tau_2 - t_v) d\tau_1 d\tau_2, \tag{46}$$

where:

$H_{jk} = H_{Rj}(t - \tau_1) H_{Rk}(t - \tau_2)$, $v\varDelta \leq t \leq v\varDelta + T$. If $v\varDelta + \mathrm{T} < t < (v + 1)\varDelta$, then all

integrals $\int_{t_v}^{t} ... d\tau$ are equal to zero and the upper sum limit "$v - 1$" equals v.

Determined by cross-correlations (46), the variance of bridge response (45) is derived in the general case where in-time correlation $K_{\hat{u}_j \hat{u}_k}(\tau_1, \tau_2)$ of wind velocity fluctuations results from a given wind spectrum (cf. Equation (6)). However, numerical application of expressions (45) and (46) is very time-consuming. To decrease computational effort, two opposing mathematical idealizations of in-time correlation will be suggested below in order to obtain approximate formulas for a tentative fast estimation of the variance.

From Equations (3–4) it reveals that the autocorrelations $K_{\hat{u}_j \hat{u}_j}(\tau_1, \tau_2)$ are the same for all zero-mean homogeneous stochastic processes $\hat{u}_j(t)$, that is $K_{\hat{u}_j \hat{u}_j}(\tau_1, \tau_2) = K_{\hat{u}_j \hat{u}_j}(\tau_1 - \tau_2) = K_{\hat{u}}(\tau)$ for $j = 1...n$, where $\tau_1 - \tau_2 = \tau$. In order to estimate the variance tentatively, it is suggested to idealize the autocorrelation function $K_{\hat{u}}(\tau)$ as: (i) constant correlation $K_{\hat{u}}(\tau) = \sigma_{\hat{u}}^2$, (ii) correlation of white noise type $K_{\hat{u}}(\tau) = \sigma_{\hat{u}}^2 \delta(\tau)$. In both cases, the variance $\sigma_{\hat{u}}^2 = K_{\hat{u}}(0)$ is obtained on the basis of Equation (4), so it is referred to a given wind spectrum $S(\omega)$. Hence, the cross-correlations given by Equation (6) can be written in the following form

(i): $K_{\hat{u}_j \hat{u}_k}(\tau) = \alpha_{jk} \sigma_{\hat{u}}^2$,   (ii): $K_{\hat{u}_j \hat{u}_k}(\tau) = \alpha_{jk} \sigma_{\hat{u}}^2 \delta(\tau),$ \hfill (47)

with reference to two considered cases. The coefficient α_{jk} is given by

$$\alpha_{jk} = \int_0^\infty S(\omega) \coh(\delta_{jk}, \omega) d\omega \bigg/ \int_0^\infty S(\omega) d\omega. \tag{48}$$

Expressions (47) are also valid for autocorrelations, because $\alpha_{jk} = 1$ when $j = k$. The variance of bridge response (45) obtained by substituting (47) into (46) is expressed for $v\varDelta \leq t \leq v\varDelta + T$ as follows

$$\text{(i): } \sigma_R^2(t) = \overline{U}^2 \sigma_{\hat{u}}^2 \sum_{j=1}^{n} \sum_{k=1}^{n} \alpha_{jk} \Big(h_j(t)h_k(t) + \lambda h_j(t)g_k(t) + \lambda h_k(t)g_j(t) + \lambda^2 g_j(t)g_k(t) \Big), \quad (49)$$

$$h_l(t) = \int_0^t H_{R_l}(t-\tau)d\tau, \qquad l = j, k, \tag{50}$$

$$g_l(t) = \sum_{i=1}^{v-1} \int_{t_i}^{t_i+T} H_{R_l}(t-\tau)P(\tau-t_i)d\tau + \int_{t_v}^{t} H_{R_l}(t-\tau)P(\tau-t_v)d\tau, \quad l = j, k, \tag{51}$$

$$\text{(ii): } \sigma_R^2(t) = \overline{U}^2 \sigma_{\hat{u}}^2 \sum_{j=1}^{n} \sum_{k=1}^{n} \alpha_{jk} \Big(h_{jk}(t) + 2\lambda g_{jk}(t) + \lambda^2 f_{jk}(t) \Big), \tag{52}$$

$$h_{jk}(t) = \int_0^t H_{R_j}(t-\tau)H_{R_k}(t-\tau)d\tau, \tag{53}$$

$$g_{jk}(t) = \sum_{i=1}^{v-1} \int_{t_i}^{t_i+T} H_{R_j}(t-\tau)H_{R_k}(t-\tau)P(\tau-t_i)d\tau + \int_{t_v}^{t} H_{R_j}(t-\tau)H_{R_k}(t-\tau)P(\tau-t_v)d\tau, \tag{54}$$

$$f_{jk}(t) = \sum_{i=1}^{v-1} \int_{t_i}^{t_i+T} H_{R_j}(t-\tau)H_{R_k}(t-\tau)P^2(\tau-t_i)d\tau + \int_{t_v}^{t} H_{R_j}(t-\tau)H_{R_k}(t-\tau)P^2(\tau-t_v)d\tau. \tag{55}$$

Approximate formulas (49) and (52) are written with the use of definite single integrals so their application decreases the computational effort significantly in comparison with Equation (46) expressed by double integrals. Therefore, these formulae, though not related exactly to wind spectrum $S(\omega)$, can be applied to an initial fast estimation of the bridge response variance. The results received in two considered cases are expected to be the upper and lower limit of variance that can serve to obtain the variance envelope. It results from an opposing properties of the assumed mathematical idealizations of the autocorrelation function $K_{\hat{u}}(\tau)$ – white noise process appears to have a flat spectral density (contains equal amounts of all frequency components) while the process with constant (flat) correlation is characterized in frequency domain by Dirac delta function [20].

It is worth noting that all the formulated solutions (i.e. mean functions (41), (42), covariance function (43) and variances (45) and (49), (52)) can be transformed easily into the solutions referred to the standard wind velocity $U(x,t) = \overline{U} + \hat{u}(x,t)$. In that

case $\overline{u}(t) = 0$, that is $\lambda = 0$, and then, the characteristics of steady-state buffeting bridge response are given by

$$\mathrm{E}[R(\infty)] = \sum_{j=1}^{n} \overline{R}_j(\infty) = \frac{1}{2}\overline{U}^2 \sum_{j=1}^{n} \left(\int_0^\infty H_{R_j}(\theta)d\theta \right), \tag{56}$$

$$\sigma_R^2(\infty) = \overline{U}^2 \sum_{j=1}^{n} \sum_{k=1}^{n} \int_0^\infty \int_0^\infty H_{R_j}(\theta_1) H_{R_k}(\theta_2) K_{\hat{u}_j \hat{u}_k}(\theta_1 - \theta_2) d\theta_1 d\theta_2, \tag{57}$$

and approximate formulas for variance are

(i): $\quad \sigma_R^2(\infty) = \overline{U}^2 \sigma_{\hat{u}}^2 \sum_{j=1}^{n} \sum_{k=1}^{n} \alpha_{jk} \int_0^\infty H_{R_j}(\theta)d\theta \int_0^\infty H_{R_k}(\theta)d\theta, \tag{58}$

(ii): $\quad \sigma_R^2(\infty) = \overline{U}^2 \sigma_{\hat{u}}^2 \sum_{j=1}^{n} \sum_{k=1}^{n} \alpha_{jk} \int_0^\infty H_{R_j}(\theta) H_{R_k}(\theta)d\theta. \tag{59}$

6. Application example

The proposed method of buffeting response analysis can be the base for extensive numerical research. However, the application example presented in this article is intended only for illustrating and clarifying advantages of the suggested procedure. Numerical results are obtained for a hypothetical single-span suspension bridge, 300 m long, with a deck of open type. For the assumed design parameters that can be found in [13, 15], the first four natural frequencies of lateral and torsional coupled vibrations are: 0.3816 Hz, 0.3978 Hz, 0.5960 Hz, 0.802 Hz. The damping ratio to critical is taken as $\alpha = 0.015$ in order to obtain the damping matrix defined as $\mathbf{C} = \mu\mathbf{B}$, where $\mu = 2\alpha\omega_1$ and ω_1 is the first circular frequency. Buffeting bridge response due to the drag wind force exclusively is analyzed. It is assumed that the periodic component of wind velocity $\overline{u}(t)$ describes repeatable gusts with the shape function $P(t - t_1) = [\sin(2\pi(t - t_1)/T - \pi/2) + 1]/2$, where $t_i \le t \le t_i + T$. The results presented in Figures 4 and 5 are calculated for $T = 30$ s, $\varDelta = 60$ s, $\lambda = 1$ and for $n = 1$ (wind load is not divided into sections along deck span).

Figures 4, 5 reveal that the mean function and standard deviation approach the steady-state cycle with the period $\varDelta$. It means that the steady-state bridge response constitutes cyclostationary stochastic process [20]. Standard deviations, calculated on the assumption that the time correlation of wind velocity fluctuations is modelled by white noise, are significantly larger then these obtained for constant time-independent correlation.

The solution achieved on the basis of Equations (45), (46) where in-time correlation of wind turbulence results from a given wind spectrum is expected to be inside the envelope formed by approximate solutions (49), (52) shown in Figure 5.
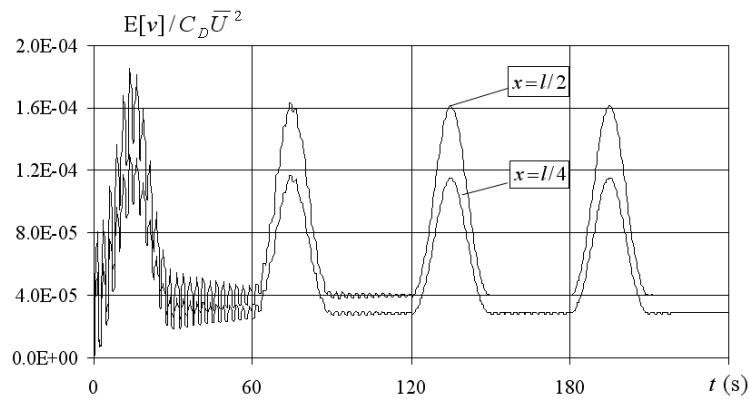
Fig. 4. Mean functions of lateral bridge vibrations at the quarter and at the middle of bridge span
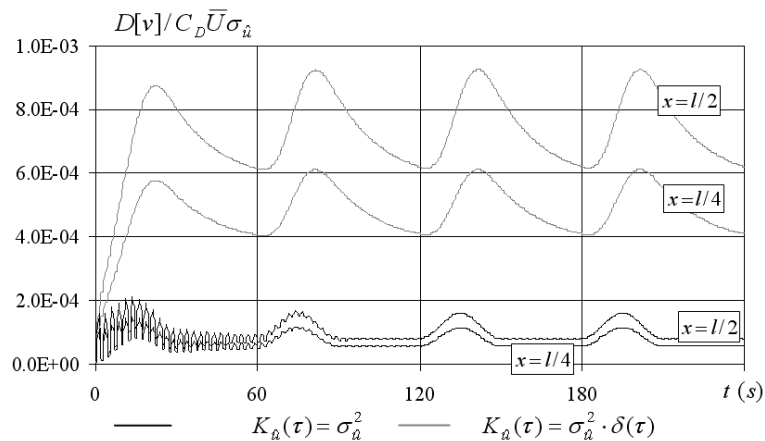
Fig. 5. Standard deviations of lateral bridge vibrations at the quarter and at the middle of bridge span

For solving design problems in bridge engineering, maximum values of mean function and standard deviation of bridge response are useful. In the considered case, such maximum values should be selected from a steady-state cycle of solutions. As an example, in Figures 6 and 7 the maximum values of response mean function and standard deviation are plotted versus cycle time Δ of the periodic component $\overline{u}(t)$ of wind velocity. Solutions obtained for the wind model suggested in this article are compared with the referred solution where the periodic component of wind velocity is neglected ($\lambda = 0$). Regarding that $\max_t[\overline{U} + \overline{u}(t)] = 2\overline{U}$ when $\lambda = 1$, the referred solution is com-

puted for mean velocity equal to $2\overline{U}$. Calculations are performed for the following data: $\sigma_{\hat{u}}/\overline{U} = 25\%$, $T = 0.5\Delta$.
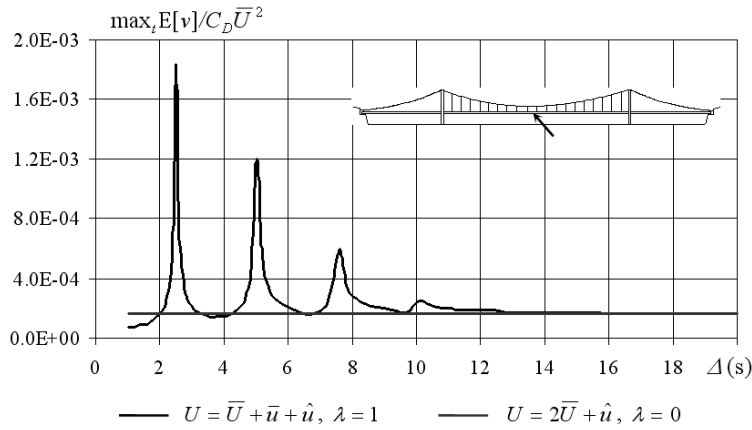
Fig. 6. Maximum value selected from a steady cycle of mean function calculated for lateral vibrations vs. cycle time of periodic component of wind velocity
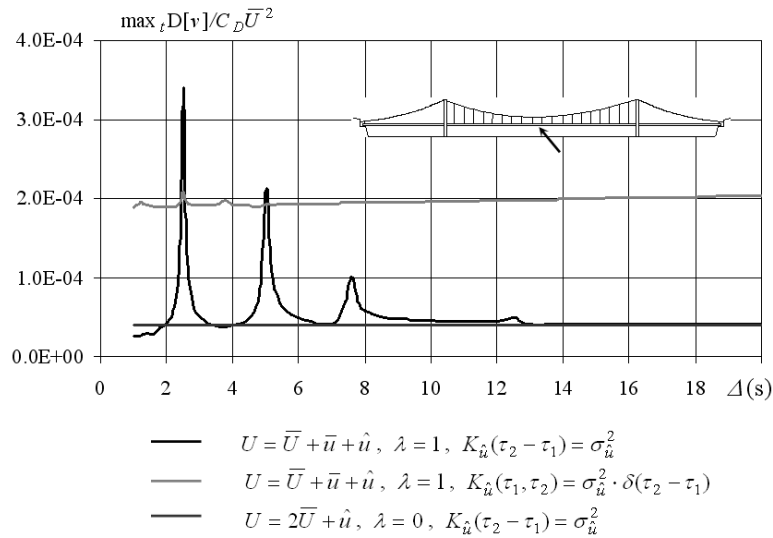
Fig. 7. Maximum value selected from a steady cycle of standard deviation calculated for lateral vibrations vs. cycle time of periodic component of wind velocity

From the results presented in Figures 6, 7 it follows that:

(i) for the considered suspension bridge, the resonant amplification effects occur when the cycle time Δ is within the range 2–8 s, it means that high-frequency wind velocity fluctuations (> 0.125 Hz) can give rise to resonant vibrations;

(ii) resonant amplification effects are relatively high when compared with the referred solution obtained for the wind with steady mean velocity;

(iii) the first resonant peak of the response mean function and standard deviation appears for $\Delta \approx 2.6$ s, that is, when the period of the leading wind velocity fluctuation is related to the first natural frequency 0.3816 Hz (symmetric mode), next two peaks are related to multiples of this frequency;

(iv) resonant peaks of the response standard deviation occur when the time-independent (constant) correlation of random wind fluctuation is assumed, the first peak significantly exceeds the solution obtained for white-noise process;

(v) when the random wind fluctuation is idealized as white-noise process, resonant peaks don't occur (the solution is weakly time-dependent) but standard deviations are significantly larger then in the case of constant correlation – excluding resonant regime.

7. Concluding remarks

This paper provides a general outline of stochastic analysis of suspension bridge response due to randomly fluctuating wind with time-dependent mean velocity. The proposed wind model and time-domain method for determining the correlation characteristics of random bridge vibrations have an important application in predicting and evaluating resonant amplification effects induced by wind velocity fluctuations. These effects should not be neglected in buffeting analysis of long-span suspension bridges even when the probability of their occurrence seems small. The above statement follows from two reasons. Firstly, the resonant regime of buffeting excitation can not be excluded from vibration analysis because natural frequencies of long-span suspension bridges cover the substantial range of high-frequency wind pulsations (~0.05–0.5 Hz). Secondly, the resonant amplification of bridge response is relatively high due to low damping level specific to suspension bridges, so it should be taken into account in bridge calculations.

The possibility of analyzing resonant buffeting effects is ensured in the presented approach by introducing the additional periodic component $\bar{u}(t)$ into the mean function of wind velocity commonly assumed as a steady one. This modification is motivated by the assumption that the periodic component $\bar{u}(t)$, related to the natural frequency of bridge vibrations, emerges as the leading wind velocity fluctuation when the bridge exhibits resonant vibrations. It is worth noting that the component $\bar{u}(t)$ of the wind velocity model suggested in this paper has more general meaning – it can describe also a series of any repeatable wind gusts with any given time-shape, as well as a single gust defined over finite time T by any continuous function. Wind velocity formulated in such a way can have an application in simulating the time history of the mean function, covariance and variance of random bridge response due to randomly fluctuating wind with any given non-steady mean velocity.

The presented method of stochastic response analysis can be easily extended to include some issues of the buffeting problem, neglected in this paper for brevity. For instance, the aerodynamic buffeting forces can be completed with self-excited forces which are defined in a frequency domain with reference to frequency of harmonic structure vibrations [2, 3, 5−8]. This can be performed by setting the component $\bar{u}(t)$ in a harmonic form with the period $T = \varDelta$. Then, the bridge vibrations are dominated by harmonic part with the frequency $\omega = 2\pi/\varDelta$ that specifies reduced frequency $K = \omega B/\overline{U}$ necessary to obtain self-excited forces. Moreover, the buffeting forces, formulated in this paper with neglecting a frequency dependence of aerodynamic characteristics, can be developed including admittance functions referred to frequency ω of the leading wind velocity fluctuation $\bar{u}(t)$. Also, it is possible to include the orthogonal spectrum of randomly fluctuating wind velocity that has been omitted in solutions presented in this paper. In order to do that, the bridge response (40) should be completed with similarly obtained solution due to these components of buffeting forces (12−14) which are referred to cross-wind component $\hat{w}(x,t)$. That is permissible for linear vibrations on the basis of superposition principle [18]. To make the calculation easier, stochastic processes $\hat{u}(x,t)$ and $\hat{w}(x,t)$ can be assumed as mutually independent while calculating the correlation characteristics of such combined response.

Finally it is worth mention that the span-wise correlation of buffeting forces is assumed in this paper as the same as that of incoming wind fluctuations. This commonly accepted assumption is questioned recently on the basis of novel studies concerned with generation mechanism of buffeting forces [7]. This new aspect of buffeting problem will be examined in further research, similarly as the all above-mentioned issues which have been neglected in the presented approach to buffeting response analysis of long-span suspension bridges.

Appendix I

Mass matrix $\mathbf{B} = \mathrm{diag}(\mathbf{B}_1, \mathbf{B}_2, \mathbf{B}_3)$ is a diagonal assemblage of sub-matrices $\mathbf{B}_i$ being expressed as

$$\mathbf{B}_i = \begin{bmatrix} (\mathbf{B}_{ww})_i & \mathbf{0} & \mathbf{0} \\ \mathbf{0} & (\mathbf{B}_{vv})_i & (\mathbf{B}_{v\varphi})_i \\ \mathbf{0} & (\mathbf{B}_{\varphi v})_i & (\mathbf{B}_{\varphi\varphi})_i \end{bmatrix}, \tag{I.1}$$

where:

$$(\mathbf{B}_{ww})_i = \frac{m_{bi}l_i}{2}\mathbf{I}_i + 2m_c l_i \mathbf{J}_i , \quad (\mathbf{B}_{vv})_i = \frac{m_{bi}l_i}{2}\mathbf{I}_i , \tag{I.2}$$

$$(\mathbf{B}_{\varphi\varphi})_i = \frac{(j_{\mathrm{B}i} + m_{bi} b_i^2) l_i}{2e^2} \mathbf{I}_i + 2 m_c l_i \mathbf{J}_i, \ (\mathbf{B}_{v\varphi})_i = (\mathbf{B}_{\varphi v})_i = -\frac{m_{bi} b_i l_i}{2e} \mathbf{I}_i, \tag{I.3}$$

and $i = 1, 2, 3$, $\mathbf{I}_i = \mathrm{diag}(1, 1, \ldots 1)$, $\mathbf{J}_i = \int_0^1 \sqrt{(1 + z_{ci}'^2)} \, \mathbf{s}_i \mathbf{s}_i^{\mathrm{T}} \, \mathrm{d}\xi_i$, $\xi_i = x_i / l_i$.

Stiffness matrix $\mathbf{K}$ has the following form

$$\mathbf{K} = \begin{bmatrix} \mathbf{K}_{11} & \mathbf{K}_{12} & \mathbf{K}_{13} \\ \mathbf{K}_{21} & \mathbf{K}_{22} & \mathbf{K}_{23} \\ \mathbf{K}_{31} & \mathbf{K}_{32} & \mathbf{K}_{33} \end{bmatrix}, \tag{I.4}$$

which is a full assemblage of submatrices $\mathbf{K}_{ik}$, where $\mathbf{K}_{ik} = \mathbf{K}_{ki}^{\mathrm{T}}$, $i, k = 1, 2, 3$ and

$$\mathbf{K}_{ii} = \begin{bmatrix} (\mathbf{K}_{ww})_{ii} & \mathbf{0} & \mathbf{0} \\ \mathbf{0} & (\mathbf{K}_{vv})_{ii} & (\mathbf{K}_{v\varphi})_{ii} \\ \mathbf{0} & (\mathbf{K}_{\varphi v})_{ii} & (\mathbf{K}_{\varphi\varphi})_{ii} \end{bmatrix}, \ \mathbf{K}_{ik} = \begin{bmatrix} (\mathbf{K}_{ww})_{ik} & \mathbf{0} & \mathbf{0} \\ \mathbf{0} & \mathbf{0} & \mathbf{0} \\ \mathbf{0} & \mathbf{0} & (\mathbf{K}_{\varphi\varphi})_{ik} \end{bmatrix}, \tag{I.5}$$

$$(\mathbf{K}_{ww})_{ii} = \frac{EJ_{yi}}{2l_i^3} \mathbf{d}_i^4 + \frac{H_0}{l_i} \mathbf{d}_i^2 + \frac{64 k_c f}{l_2^2} l_i^2 \mu_i^2 \mathbf{g}_i \mathbf{g}_i^{\mathrm{T}}, \ (\mathbf{K}_{vv})_{ii} = \frac{EJ_{zi}}{2l_i^3} \mathbf{d}_i^4 + m_{bi} g \mathbf{G}_i, \tag{I.6}$$

$$(\mathbf{K}_{\varphi\varphi})_{ii} = \frac{EJ_{\omega i}}{2e^2 l_i^3} \mathbf{d}_i^4 + \left(\frac{GI_i}{2e^2 l_i} + \frac{H_0}{l_i} \right) \mathbf{d}_i^2 + \frac{m_{bi} g l_i (b_i - c_i)}{2e^2} \mathbf{I}_i +$$

$$\frac{m_{bi} g c_i^2}{e^2} \mathbf{G}_i + \frac{64 k_c f}{l_2^2} l_i^2 \mu_i^2 \mathbf{g}_i \mathbf{g}_i^{\mathrm{T}}, \tag{I.7}$$

$$(\mathbf{K}_{v\varphi})_{ii} = (\mathbf{K}_{\varphi v}^{\mathrm{T}})_{ii} = -\frac{m_{bi} g c_i}{e} \mathbf{G}_i, \ \left(\mathbf{K}_{ww} \right)_{ik} = \left(\mathbf{K}_{\varphi\varphi} \right)_{ik} = \frac{64 k_c f}{l_2^2} l_i l_k \mu_i \mu_k \mathbf{g}_i \mathbf{g}_k^{\mathrm{T}}, \tag{I.8}$$

where:

$$\mathbf{g}_i = \mathrm{col}(1/\pi, \ \ 0, \ \ 1/3\pi, \ \ 0, \ \ 1/5\pi, \ \ \ldots), \ \mathbf{G}_i = \int_0^1 \frac{l_i}{h_{\mathrm{C}} - h_i - (h_{i+1} - h_i)\xi_i} \, \mathbf{s}_i \mathbf{s}_i^{\mathrm{T}} \, \mathrm{d}\xi_i.$$

References

[1] Gimsing N.J.: *Cable supported bridges, concept and design*, John Wiley & Sons, New York, 1996.

[2] Simiu E., Scanlan R.H.: *Wind effects on structures, fundamentals and applications to design*, John Wiley & Sons, New York, 1996.

[3] Boonyapinyo V., Miyata T., Yamada H.: *Advanced aerodynamic analysis of suspension bridges by state-space approach*, ASCE Journal of Structural Engineering, Vol. 125, No. 12, 1999, pp. 1357–1366.

[4] Cao Y., Xiang H., Zhou Y.: *Simulation of stochastic wind velocity field on long-span bridges*, ASCE Journal of Engineering Mechanics, Vol. 126, No. 1, 2000, pp. 1–6.

[5] Chen X., Matsumoto M., Kareem A.: *Time domain flutter and buffeting response analysis of bridges*, ASCE Journal of Engineering Mechanics, Vol. 126, No. 1, 2000, pp. 7–16.

[6] Chen X., Matsumoto M., Kareem A.: *Aerodynamic coupling effects on flutter and buffeting of bridges*, ASCE Journal of Engineering Mechanics, Vol. 126, No. 1, 2000, pp. 17–26.

[7] Chen X., Kareem A.: *Advances in modelling of aerodynamic forces on bridge decks*, ASCE Journal of Engineering Mechanics, Vol. 128, No. 11, 2002, pp. 1193–1205.

[8] Dyrbye C., Hansen S.O.: *Wind loads on structures*, John Wiley & Sons, Chichester, 1997.

[9] Flaga A.: *Quasi-steady models of wind load on slender structures. Part I. Case of a motionless structure*, Archives of Civil Engineering, Vol. XL, No. 1, 1994, pp. 3–28.

[10] Flaga A.: *Quasi-steady models of wind load on slender structures. Part II. Case of a motionless structure*, Archives of Civil Engineering, Vol. XL, No. 1, 1994, pp. 29–41.

[11] Flaga A.: *Quasi-steady models of wind load on slender structures. Part III. Applications of quasi-steady theory in aerodynamics of slender structures*, Archives of Civil Engineering, Vol. XLI, No. 3, 1995, pp. 343–376.

[12] Bryja D.: *Spatial vibrations of multi-span suspension bridges with large cable sags: continnum formulation*, Proc. of the 4th European Conference on Structural Dynamics EURODYN'2002, Munich, Germany, (H. Grundmann, G.I. Schuëller, editors) Lisse: A.A. Balkema, Vol. 2, 2002, pp. 1047–1052.

[13] Bryja D.: *Deterministic and stochastic methods of analysis of suspension bridge vibrations*, Wrocław University of Technology Press, Wrocław, 2005 (in Polish).

[14] Bryja D., Śniady P.: *Random vibration of a suspension bridge due to highway traffic*, Journal of Sound and Vibration, Vol. 125, No. 2, 1988, pp. 379–387.

[15] Bryja D., Śniady P.: *Spatially coupled vibrations of a suspension bridge under random highway traffic*, Earthquake Engineering and Structural Dynamics, Vol. 20, 1991, pp. 999–1010.

[16] Bryja D., Śniady P.: *Stochastic non-linear vibrations of highway suspension bridge under inertial sprung moving load*, Journal of Sound and Vibration, Vol. 216, No. 3, 1998, pp. 507–519.

[17] Bryja D.: *Coupled lateral-torsional vibrations of suspension bridge excited by random wind load*, Zeitschrift für Angewandte Mathematik und Mechanik (ZAMM), Vol. 81, S2, 2001, pp. 183–184.

[18] Bryja D., Woszczyna A., Prokopowicz D.: *Non-stationary wind model in buffeting analysis of cable-stayed bridge*, Proc. of 7th European Conference on Structural Dynamics, EURODYN'2008, Southampton, UK, CD-ROM edited by M.J. Brennan, ISVR University of Southampton, 2008, p. E116.

[19] Lin Y.K.: *Probabilistic theory of structural dynamics*, R.E. Krieger Pub. Co., New York, 1976.

[20] Gardner W.A., *Introduction to random processes with applications to signals and systems*, Macmillan Pub. Comp., New York, 1986.

Analiza stochastyczna drgań mostu wiszącego obciążonego
porywistym wiatrem o prędkości średniej zależnej od czasu

Przedstawiono ogólny schemat metody analizy drgań stochastycznych mostu wiszącego, obciążonego losowym działaniem zmiennego wiatru o prędkości średniej zależnej od czasu. Sformułowano stochastyczny model pola prędkości wiatru oraz wynikające stąd obciążenia aerodynamiczne. Funkcję losową określającą prędkość założono w postaci sumy prędkości stałej, składnika okresowo zmiennego w czasie i losowej fluktuacji zależnej od czasu i od zmiennej przestrzennej. Losową fluktuację zastąpiono wektorowym procesem stochastycznym o składowych zależnych tylko od czasu, wynikających z podziału mostu na sekcje wzdłuż rozpiętości. Opracowano metodę wyznaczania charakterystyk drgań losowych mostu, w ujęciu teorii korelacyjnej, ograniczając rozważania do zadania liniowego. Zaprezentowana metoda umożliwia analizę efektów rezonansowych dzięki uwzględnieniu składnika okresowego średniej prędkości wiatru, który może opisywać najniekorzystniejszą pulsację prędkości o częstości zbliżonej do częstości własnej drgań mostu. Zaproponowano sposób wstępnego oszacowania wariancji, którego podstawą merytoryczną jest matematyczna idealizacja korelacji czasowej fluktuacji wiatru, w postaci „białego szumu" lub korelacji stałej. Przedstawiono przykład numeryczny zastosowania opracowanej procedury obliczeniowej do analizy drgań przykładowego mostu.

3K Mechanical Paradox transmissions:
The shaping of the meshing zone for better efficiency

A. GOLENKO

Wrocław University of Technology, Wybrzeże Wyspiańskiego 25, 50-370 Wrocław, Poland

In the paper, a new method (Hori and Hayashi) for the design of tooth addendum in a Mechanical Paradox 3K transmission gear was presented. A meshing scheme obtained in agreement with this method and actual meshing schemes after inclusion of generation and engagement limitations were presented. The results of calculations using a different approach proposed by the author to the problem of access/recess contact ratio equalisation were also included.

Keywords: *3K gear transmissions, efficiency, equalization, contact ratio*

1. Introduction

"Make four wheels, one wheel as thick as the other three. Cut teeth in all wheels. Set the thick wheels in line. Set the thick wheel so its teeth take into the three ones. Turn the thick wheel: One of the three wheels rotates in one way, the second in the other way and the third does not rotate at all" [1].

This procedure was first proposed at the end of the 17th century by James Ferguson, an English clockmaker, who used it for the construction of an orrery (Figure 1). His name was given to all transmission based upon this concept and become part of the engineering heritage.
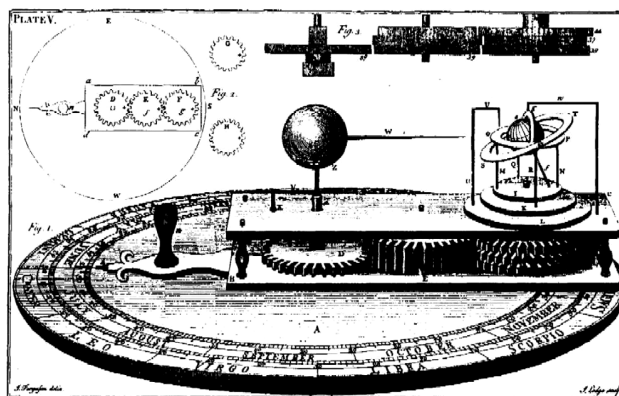

Fig. 1. Ferguson's orrery, 1773 [1]

The meshing scheme proposed by Ferguson (Figure 2a) had been employed for the modification of a traditional 3K transmission (a Wolfrom's transmission, Figure 2b). It consisted in the replacement of the two (different in size) planet gears by one uniform planet gear with the same number of teeth along its width (Figure 2c). This made it possible to avoid problems with the proper angular alignment of the planet gears, which are present in traditional gear sets of this type.
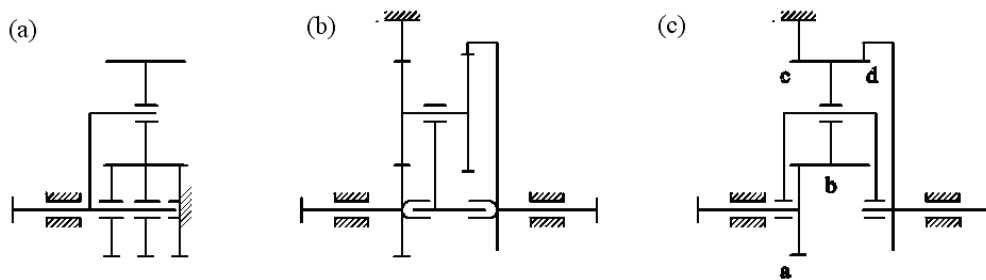

Fig. 2. Schemes of the Ferguson's (a), conventional 3K (b), and 3K Paradox (c) gear trains

First research projects dealing with this transmission had been carried out by Jastrebov [2], [3]. He gave a brief description of advantages and disadvantages of these transmissions together with the results of testing. The tested units featured nearly constant efficiency, equal to approx. 78%, in a wide range of transmission ratios. Based upon the results obtained by Jastrebov, Hori and Kurita [4] proposed a modification in the design of the whole gear train that aimed at its higher efficiency. The ultimate objective was to employ the transmission in the main arm of a space robot. The modification consisted in the equalization of the approach and recess contact ratios in the meshing of the common planet gear with the two internally toothed gears. The modified transmission was manufactured and tested. The results confirmed a roughly 10% increase in efficiency when compared to the efficiency of traditional gear sets. Hori and Hayashi [5] analysed in detail the proposed approach and offered a new method that supposedly guarantees the maximum equalisation of the approach and recess contact ratios over a wide range of overlap ratios.

As the proposed modifications result in non-standard tooth proportions and the authors, when questioned in a direct e-mail contact, gave only vague remarks concerning the generation process, the author analysed in detail these problems in conference papers [6]. A new area of application or 3K transmissions is micro-robotics. Suzumori et all [7] used this type of transmission to drive the feed of a robot operating in a pipe, one inch in diameter.

The objective of this paper is a short presentation of the method proposed by Hori, Kurita, and Hayashi, its verification in view of all constraints present during the generation and meshing processes and a proposal for further steps aiming at the best equalization of the approach and recess contact ratios.

2. The idea of the modification and method proposed by Hori, Kurita, and Hayashi [4], [5]

A starting point for the modification was a conventional Mechanical Paradox transmission in which the number of teeth, module etc. had been already established.

The left part of this combined drawing represents the toothed pair b–d; and the right side, the toothed pair b–c. The pressure lines are traced on both sides to show the respective limiting points (A, E).
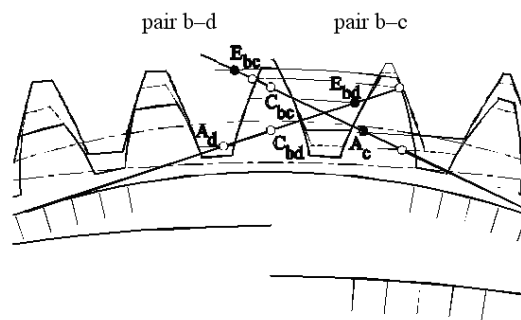

Fig. 3. Meshing representation in a conventional (dashed lines) and modified (solid lines) 3K Mechanical Paradox transmission (after [4])

A conventional 3K transmission (dashed lines) features very diversified approach and recess contact ratios: there is a strong shift in the position of the pitch point, either towards the addendum (pair b–c; the right side), or towards the dedendum (pair b–d; the left side). The addendum diameter of gear b is the least value that offers a minimum value of the bottom clearance in mesh with the three other gears. As the centre distance must remain the same, any change in the profile shift coefficients that improves situation in one toothed pair makes it worse in the other one.

A modification proposed by Hori and Kurita (solid lines) consists in the reduction of these disproportions in meshing. In the modified gear the tooth addendum in gear bc (a section of b in mesh with c) was increased and in the gear c, decreased. In toothed pair b–d the addendum of gear bd was decreased and in gear d, it was left unchanged.

The equalisation procedure proposed by Hori and Hayashi (details in [5]) is separate for each of the meshing toothed pairs. The idea of the method is to sequentially change the addendum coefficient in gear b seeking the maximum addendum diameter in gear bc when preserving a necessary minimum value of the top land thickness. The search shall be carried out within an area defined by six constraints, the most important of them being the absence of undercutting and interference.

Based upon the proposed procedure Hori and Hayashi established optimum meshing parameters for a 351 ($z_a = 12$, $zb = 47$, $zc = -105$, $zd = -108$, $m = 1.25$) transmis-

sion ratio gear with the overlap ratio equal to 1.2. These are: $x_b = 0.36$, $x_a = 0.308$, $x_c = -1.627$ (the ISO designation convention for internal gearing applies here). These values correspond to a pointed tooth limit of the planet gear. The analysis made by the authors in [5] is based upon an assumption that as long as the pointed tooth limit diameter is larger than (or the same as) the equal approach/recess contact ratio diameter, it is also possible to generate such gearing, which is not always true. This will be illustrated in the next chapter (a transition from theoretical values to actual values of the addendum radius for the data given above). All in all, the proposed method constitutes a shift in the traditional method of designing 3K Paradox transmissions (in a close relationship with parameters of the cutting tool) to a method, in which parameters of the cutting tool are included in the constraints only. This approach has been known as the Direct Gear Design [8].

3. Implementation of the method to a 351-transmission ratio gear train

3.1. Theoretical equalisation of the approach and recess contact ratios

Schemes of meshing in toothed pairs bc–c, bd–d and a–bc for a 351 transmission ratio gear with the overlap ratio $\varepsilon_\alpha = 1.2$ are shown in Figure 4 (the left side). These are valid for the data given in the previous chapter and are a true representation of dimensional proportions in the meshing.
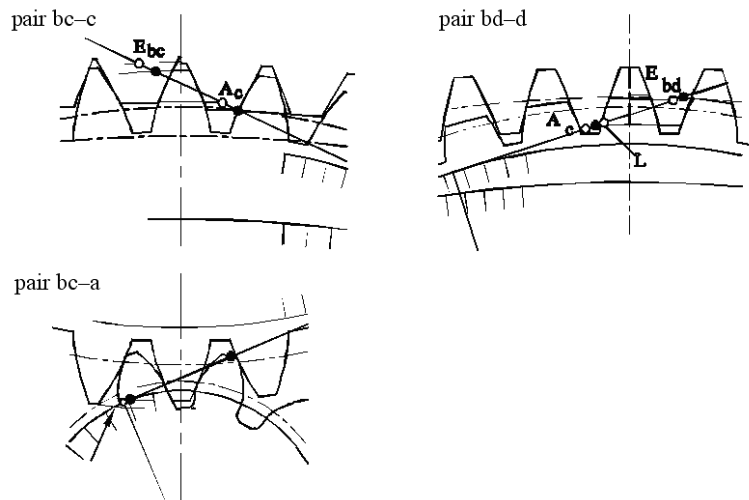

Fig. 4. Theoretical (the left side) and actual (the right side) values of the addendum radiuses
in meshing of toothed pairs bc–c, bc–a, and bd–d

Studying the left side of each meshing schemes it is clear that essential modifications of the tooth addendum in all toothed pairs are necessary (in spite of the fact that

the fulfilment of these conditions was prescribed by the very method proposed by Hori and Hayashi). As regards the tooth addendum in gear bc, it is clear that the fundamental law of toothed gearing will not be preserved in the toothed pair a–bc and this addendum must be reduced irrespective of possible generation and meshing problems in the toothed pair bc–c. The bottom clearance in the toothed pair bd–d is too small and interference is present (for reference, point L denotes a position of the last involute point at the bottom of gear b, if generated by a standard rack).

3.2. Actual equalisation of the approach and recess contact ratios

The actual equalisation of the approach and recess contact ratios is shown at the right sides of the meshing schemes in Figure 4. Dark points represent the final points of the pressure line after modification. The modified tooth proportions were obtained in the following way: The analysis had been started from the generation of gear b: for pinion cutters of different regrinding status, the dedendum diameter and the last involute point at the tooth foot were found. This made it possible to find the minimum value of the addendum diameter in gear d, meeting conditions of the bottom clearance and interference absence. An optimum cutter for gear b was a heavily reground one ($x_F = -0.25$, $c^* = 0.3$) with a number of teeth equal to 30 ($z_F = 30$). For gear d, a new cutter with also 30 teeth was assumed. Problems with its radial feed into the blank (which are characteristic for cutters with a big number of teeth) or tooth tip cutting (characteristic for cutters with a small number of teeth) are then absent. To generate gears c and a, assumed were cutters with 30 and 20 teeth respectively ($c^* = 0.3$, $x_F = 0.105$). A certain lack of symmetry visible in all meshing pairs stems from a need to compensate the reduced sections of the contact line with the elongation of the adjacent sections so as to maintain the contact ratio at the assumed level (1.2).

4. A quest for the best equalisation – an evaluation method

As the actual equalisation is different to the theoretical one (in terms of the addendum radiuses), a question arose if the strategy that had been proposed and adopted by Hori and Hayashi could not be modified to obtain an even better equalisation.

A quantitative analysis of the equalisation procedure was carried out using an objective function and taking into account all meshing gears. As the efficiency of toothed pair a–bc is of small importance to the overall efficiency of the gear train, a simplified formula, including only toothed pairs bc–c and bd–d, was used:

$$FC = 2 - \varepsilon_{\alpha 1}^{bc} - \varepsilon_{\alpha 2}^{bc} - \varepsilon_{\alpha 1}^{bd} - \varepsilon_{\alpha 2}^{bd} + \left(\varepsilon_{\alpha 1}^{bc}\right)^2 + \left(\varepsilon_{\alpha 2}^{bc}\right)^2 + \left(\varepsilon_{\alpha 1}^{bd}\right)^2 + \left(\varepsilon_{\alpha 2}^{bd}\right)^2,$$

where: the right side terms of the above equation represent partial (approach and recess) contact ratios for toothed pairs bc–c and bd–d. With an ideal equalisation this

simplified function takes a value of 1.04. In the above analysed case this function is equal to 1.24 (after modification).

To find the maximum value of the objective function within a range of possible values of coefficients x_d and x_b, a comprehensive search has been done. The calculations were carried out initially in agreement with the method proposed by Hori and Hayashi, i.e.:

a) $x_d = 0$ or close to zero, a starting value for x_b,

b) theoretical equalisation radiuses,

c) the minimum radius in gear bc with a width of the top land not less than 0.4 m,

d) if a value from point c was less than a value from point b, them, contrary to the original method, the least of the two values was accepted, x_b was left unchanged and calculations were continued the way explained in the previous chapter,

e) if any constraint was hit, the relevant addendum radius was decreased and the loss in the overlap ratio was made up with the associated radius,

f) the objective function was calculated,

h) a new value of x_b was set and the process repeated till x_b struck the limit (undercutting).

The same procedure was repeated for slightly different values of x_d. The results shown in Figure 5 correspond to a situation when gear b is generated using a pinion shaped cutter ($z_F = 30$, $c^* = 0.3$) of different regrinding status (x_F).
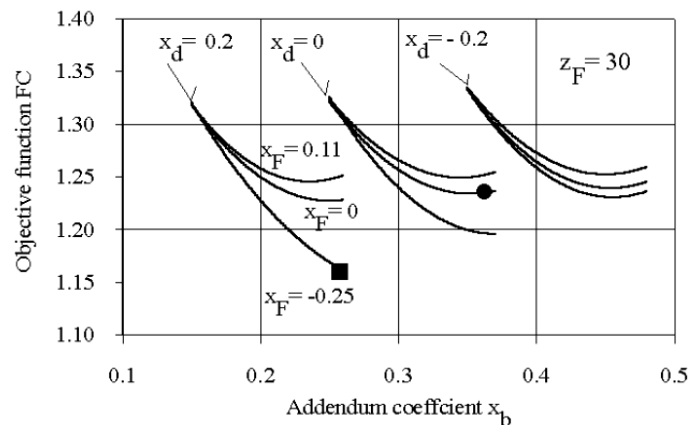
Fig. 5. Maximum equalisation of the approach and recess contact ratios as a function of x_b and the regrinding status x_F of the cutter (generation of gear b)

There is a well-pronounced minimum of the objective function for each graph (approximation) and it is not, apart from cases of generation with maximum reground cutters, a minimum on a constraint. The objective function decreases (a better equalisation) with the positive addendum modification in gear d and with the regrinding status of the cutter. This is associated mostly with a better equalisation in pair bd–d.

For the analysed gear transmission ($x_d = 0$, $x_b = 0.36$, $x_F = 0$) FC = 1.24 (a dark point in Figure 5). Using a properly selected tool for the generation of gear b, a value of this function can be decreased to 1.19 (the right side of meshing in Figure 4). By changing additionally the addendum modification in gear d, a value of the objective unction may be further reduced to 1.17 (a dark square). Tooth proportions for this point are shown in Figure 6. The toothed pair bd–d features then the full equalisation.
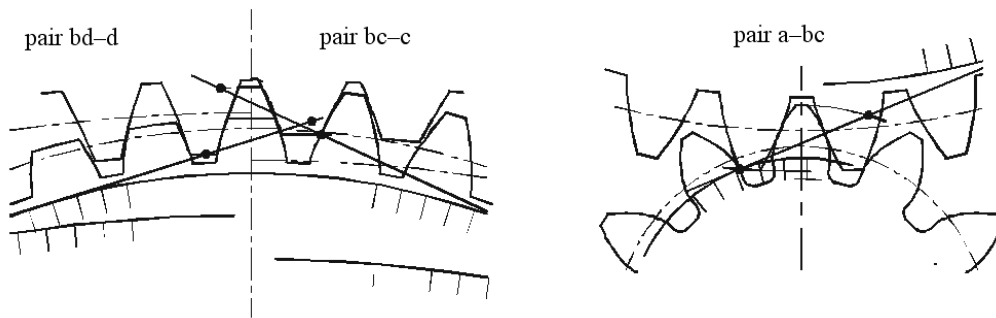
Fig. 6. Graphical representation of a transmission with the best equalisation (FC = 1.17)

5. Conclusions

1. The approach proposed by Hori and Kurita [4] provides a quick and relatively simple method (in terms of the numerical effort) to find the best equalisation in a 3K Paradox gear train. A generalisation proposed by Hori and Hayashi [5] doesn't meet fully objectives set by the authors (the full equalisation). Needed are some ex-post modifications to the results obtained.

2. Providing a positive addendum modification to gear d is beneficial to the equalization process. This results with reduced values of the pressure angle in both external/internal meshing pairs. For the analysed toothed pairs this process is limited by a danger of undercutting in gear a (in the limiting case a summary addendum modification in toothed pair bc–c is less than a value required due to a danger of undercutting in gear a). A positive addendum modification in gear d calls for a very detailed and careful analysis of generation conditions.

3. A better equalisation might be further sought by a reduction of the teeth number in gear b. This doesn't change the transmission ratio and doesn't violate assembly requirements permitting to continue the trend explained above. Additionally, a situation is avoided, in which the first meshing point in pair a–bc is very close to the base circle.

4. There is a strong influence of the cutter regrinding status on the result obtained; less important is the influence of x_b (so heavily stressed in the Hori and Hayashi's method).

References

[1] Ferguson J.: *Select mechanical exercises*, 1773.

[2] Jastrebov V.M.: *3K Epicyclic gear trains with a common planetary gear*, Vestnik Mashinostrojenija, 1960, No. 3, pp. 17–19 (in Russian).

[3] Jastrebov V.M.: *3K Epicyclic gear trains with one-body satellite*, Vestnik Mashinostrojenija, No. 12, 1965, pp. 7–10 (in Russian).

[4] Hori K., Kurita Y.*: Improvements in 3K mechanical "Paradox" planetary gear efficiency*, Power Transmission and Gearing Conference (ASME), Vol. 88, 1989, pp. 259–265.

[5] Hori K., Hayashi I.: *Improvement of efficiency of 3K-Type mechanical paradox planetary drive by equalising approach and recess contact Ratios*, DE – Vol. 48, Power Transmission and Gearing Conference (ASME), 1996, pp. 419–426.

[6] Golenko A.: *Interference limitations in a 3K paradox gear transmission, power source and transfer*, 6th International Scientific and Professional Conference, Becice, Serbia and Montenegro, 2000, pp. 403–408.

[7] Suzumori K. et al.: *Micro-inspection robot for* 1-*in pipes*, IEEE/ASME Transactions on Mechatronics, Vol. 4, No 3, 1999, pp. 286–292.

[8] Kapelevich A.L., McNamara T.M.: *Introduction to direct gear designer*, the Global Power Train Congress 2005, September 2005, pp. 48–62.

Jednowieńcowe przekładnie typu 3K: kształtowanie zazębienia dla poprawy sprawności

W artykule przedstawiono nową metodę (Hori i Hayashi) kształtowania zazębienia w jednowieńcowych przekładniach typu 3K umożliwiającą poprawienie sprawności w zazębieniu. Przedstawiono obraz zazębienia uzyskany po zastosowaniu metody, rzeczywisty obraz po uwzględnieniu wszystkich ograniczeń występujących w czasie nacinania uzębień i ich późniejszej współpracy oraz wyniki uzyskane przy nieco odmiennej procedurze poszukiwania rozwiązania o najlepszym wyrównaniu cząstkowych wskaźników przyporu.

Influence of cold and hot pressing on densification behaviour of titanium alloy powder Ti6Al4V

Z. GRONOSTAJSKI, P. BANDOŁA, T. SKUBISZEWSKI

Wrocław University of Technology, Wybrzeże Wyspiańskiego 25, 50-370 Wrocław, Poland

This paper analyzes three ways of processing Ti-6%Al-4%V titanium alloy powders: compacting specimens in 25 mm diameter under different pressures by a floating die and sintering in a vacuum furnace, producing axially symmetric PM compacts in a compacting device with a plastic die, hot compacting a powder in a die under protective argon atmosphere. The powder was produced by the following two methods: HDH (hydride-dehydride) and gas atomization (GA). A special device, allowing the simultaneous compaction and sintering of powder under protective argon atmosphere, was constructed. A solid material was obtained from Ti6Al4V titanium alloy powders produced by GA. It seems that the proposed technology of compaction under argon atmosphere could be used to manufacture products from titanium alloys on the industrial scale more economically since it combines compaction and sintering and does not require costly equipment.

Keywords: *sintering, titanium alloy, consolidation*

1. Introduction

The metallurgy of titanium and its alloys has been intensively developed for over 40 years now. Recent studies show that this material could be more widely used in medicine, in both prosthetics (e.g. for joint prostheses and various implants) and medical technology (e.g. surgical instruments and components of dialyzers, artificial hearts, etc.), as well as in the aircraft industry, the rocket industry and the chemical industry. Titanium is a very light metal with unique mechanical properties. It can be used in a wide range of temperatures. It is characterized by high biocompatibility, high corrosion resistance and very high relative strength (a strength/density ratio) in comparison with other metallic materials [1, 2]. Conventional titanium metallurgy supplies a wide spectrum of materials with very different properties [3–7]. However, any further improvement of such materials through conventional mechanical processing and heat treatment becomes less and less effective. It seems that creative synthesis techniques (such as powder metallurgy), which allow one to obtain materials with predetermined properties suitable for the specific applications, should be developed. Despite the very good properties of products made of titanium alloys, their high manufacturing costs are the reason that the industrial application of titanium powder metallurgy has been rather slow, especially in Europe. Titanium alloy powder metallurgy holds the promise that cheaper products with better properties will be produced [8, 9]. Today, because of the considerable technological difficulties, the very costly method of hot

isostatic pressing (HIP) is usually employed [10, 11]. The high costs provide a stimu-
lus for a search for cheaper sintering technologies which would yield products with
similar properties as the ones which characterize products obtained by hot isostatic
pressing. Research on different metal and metal alloy powders shows that very good
properties and low production costs can be achieved using other methods, mainly hot
compacting and extrusion [12–14].

Therefore it seems expedient to investigate the possibilities of compacting titanium
powders using other technologies than hot isostatic pressing. This paper analyzes three
ways of processing Ti-6%Al-4%V titanium alloy powders:

– compacting ϕ 25 mm specimens under different pressures by a floating die and
sintering in a vacuum furnace;

– producing axially symmetric PM compacts in a compacting device with a plastic
die;

– hot compacting a powder in a die under protective argon atmosphere.

2. Materials

Powder Ti6Al4V was used. The powder was produced by the following two methods:

1. HDH (hydride-dehydride), consisting in hydriding and dehydrogenation. Powder
with irregular particles (Fig. 1), with a reduced chlorine content (as compared with the
titanium sponge powdering method) but with its oxygen content likely elevated, is
obtained in this way. The chemical composition of the powder is shown in Table 1.
The powder particle size is below 44 μm (325 mesh).
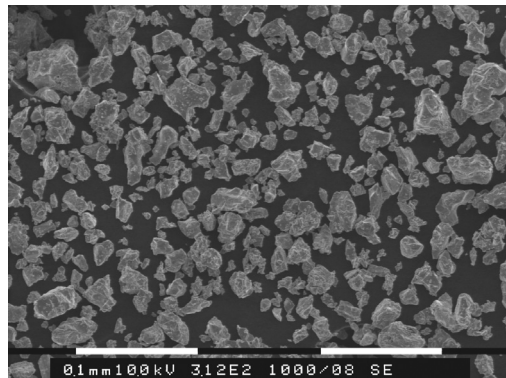

Fig. 1. Particles of Ti6Al4V titanium alloy powder produced by HDH

Table 1. Chemical composition of Ti6Al4V titanium alloy powder produced by HDH

Ti [%]	Al [%]	V [%]	Fe [%]	Zr [%]	O [%]	N [%]	H [%]
rest	6	4	0.03	0.03	Max. 0.55	Max. 0.5	Max. 0.3

2. Gas atomization (GA) of liquid metal. High-grade titanium alloy powders with spherical particles (Figure 2, the chemical composition is shown in Table 2) can be produced by this method.
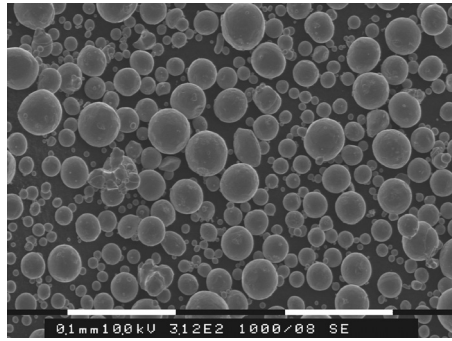
Fig. 2. Spherical Ti6Al4V titanium alloy powder produced by GA

Table 2. Chemical composition of Ti6Al4V titanium alloy powder produced by GA

Ti [%]	Al %]	V [%]	Fe[%]	O [%]	N [%]	H [%]
rest	5.9	3.9	0.19	0.12	0.01	0.004

3. Tests

3.1. Compacting ϕ 25 mm specimens under different pressures by floating die and sintering in vacuum furnace

Titanium alloy powder was precompacted under different pressures (1019 MPa, 700 MPa, 550 MPa, 500 MPa and 400 MPa). The compaction time under the maximum pressure was constant and amounted to 2 minutes. Each specimen was made of 26.7 g of powder and it was 25 mm in diameter. In the case of the spheroidal powder produced by GA, no compact with permanently bonded powder particles was obtained. All the specimens broke while being removed from the die (Figure 3).

Fig. 3. Compact made of Ti6Al4V titanium alloy powder produced by GA,
after compaction under pressure of 1019 MPa

In the case of the irregular powder produced by HDH, 500 MPa was sufficient to obtain permanent bonding of titanium alloy powder grains. This pressure was adopted as the limit pressure for the powder produced by HDH. Several different pressures were applied in order to determine the effect of pressure on the porosity of the compacts before and after sintering. The specimens were sintered in a vacuum furnace because of the high chemical activity of titanium alloy (particularly at high temperatures) and the risk of spontaneous ignition at temperatures above 237.5 °C. During sintering there was a vacuum of $1 \cdot 10^{-4}$ mbar in the furnace. The specimens were heated up at a rate of 15 °C/min to 1200 °C. This operation lasted about 80 min while sintering at a temperature of 1200 °C lasted 40 [min]. Figure 4 shows the relation between porosity and compaction pressure, and its changes caused by sintering.
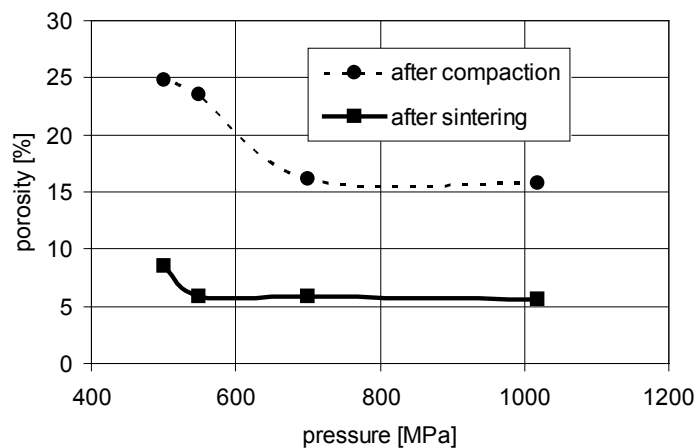
Fig. 4. Porosity versus pressure for Ti6Al4V titanium alloy produced by HDH

According to the diagram, before sintering porosity rapidly decreases from 24.8% at 500 MPa to 16.2% at 700 MPa. For greater pressures it remains at an almost constant level of 15.7%. After sintering, at pressures below 550 MPa porosity quickly decreases while above 550 MPa it has an almost constant value of 5.7%. This means that in the case of the Ti6Al4V titanium alloy powder produced by HDH it is not necessary to use too high pressures since after the limit of 550 MPa is exceeded, the porosity of the material after sintering changes only slightly.

After sintering two phases structure was obtained: α and β segregated in the Ti6Al4V titanium alloy. Phase α predominated since aluminium, which is responsible for the stabilization of this phase, occurs in a larger amount than vanadium which stabilizes phase β. The two phases occur in the lamellar form, with phase α plates (which segregate at grain boundaries) being the link between them (Figure 5). The number of pores increases towards the specimen's walls, which shows a strong effect of friction on the compaction process.
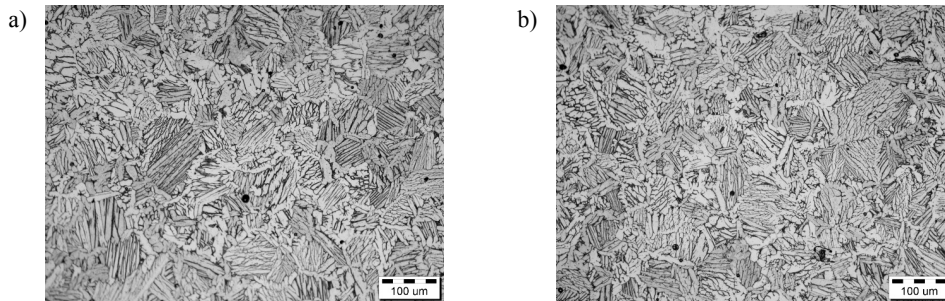
Fig. 5. Cross section of specimen Ti6Al4V titanium alloy powder cold compacted with pressure
of 1019 MPa and sintering: a) near specimen's edge, b) specimen's centre

3.2. Production of compacts in compacting device with plastic die

Since no durable compacts suitable for sintering could be made from the spheroidal
Ti6Al4V titanium alloy powder produced by GA, the method of compacting with
a plastic die was employed. The idea of the method is shown in Figure 6.
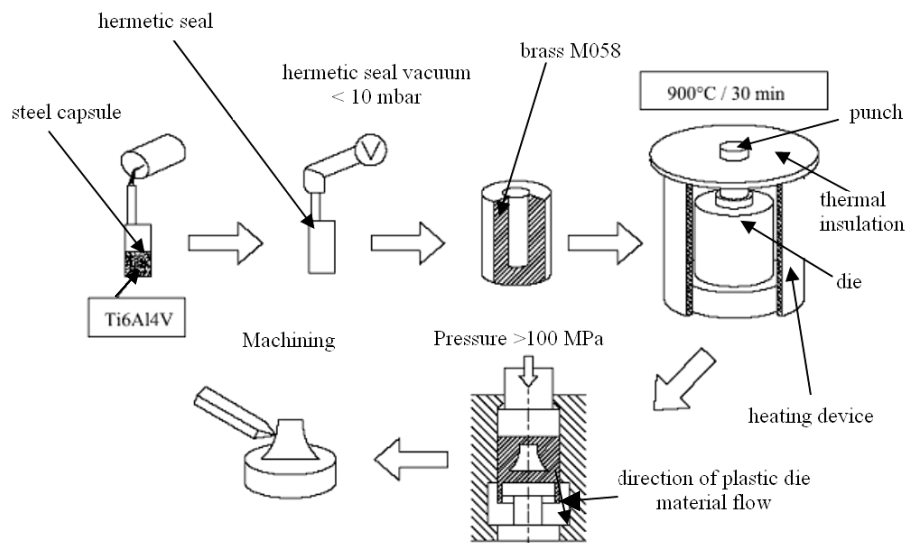
Fig. 6. Deformation of Ti-6Al-4V alloy powder in plastic die [15]

The consolidation of powder Ti-6Al-4V in this process includes the following op-
erations [15]:
   • a special steel capsule is made;
   • the powder is poured into the steel capsule and the latter is degassed and hermeti-
cally closed;

• brass alloy MO58 (which performs the role of a plastic die) is poured over the capsule placed in a mould;

• the die with the capsule is heated up to a proper temperature in a heating device; thanks to thermal insulation the temperature is kept stable;

• the plastic die with the capsule containing the titanium alloy powder is deformed (e.g. through extrusion), the plastic die material flows into the free space under the punch and at the same time the capsule with the titanium powder inside is compacted;

• the deformed plastic die is held at a temperature of 900 °C for 30 minutes;

• the permanently deformed die with the capsule is demoulded;

• the plastic die and the capsule are mechanically separated from the compacted titanium alloy powder.

The first tests of compaction in the plastic die were carried out at a temperature of 900 °C. The compaction distance was $s = 50$ mm. When the upper punch distance measuring device showed that the set distance had been covered, the compaction force indicated by the force sensor amounted to 2–3 kN, (i.e. it was probably too low to ensure proper compaction). Then the upper punch was removed, the tools were held at a temperature of 900 °C for 30 minutes, the heating device was switched off and the whole system was cooled in air down to the ambient temperature. When the set of tools was disassembled it became apparent that the viscosity of the brass used as the plastic die was too low (because of the too high temperature) and the material flowed down under gravitation and filled the free space in the bottom part of the die. As a result, the capsule containing the Ti6Al4V titanium alloy powder was exposed. At the moment when the upper punch came into contact with the capsule, the steel pipe broke and the vacuum was lost. Thus the capsule with the powder was not deformed in accordance with the experimental assumptions. Therefore the compaction temperature was lowered to 800 °C to reduce the flow of the brass. The heating up to a temperature of 800 °C took nearly six hours. When the temperature was reached, compaction in the plastic die started. When it finished and the punch was withdrawn, the mould and the plastic die together with the compacted powder were heated for 30 minutes at a temperature of 800 °C and subsequently cooled in air down to the ambient temperature.

The cooled down plastic die was demoulded and the part which held the compacted capsule containing the Ti6Al4V powder was separated (Figure 7).
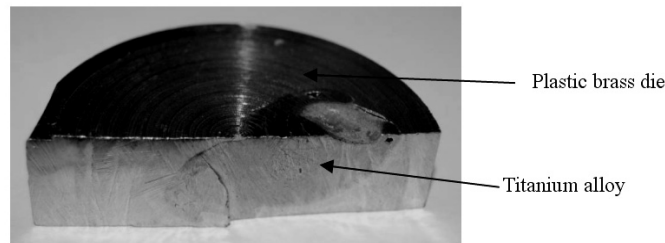

Fig. 7. Cut through titanium specimen and plastic brass die

Since the produced compact was highly irregular in shape the porosity of the compact could not be determined by conventional methods (by comparing its density with that of the compacted solid Ti6Al4V alloy). Therefore microsections were made, which revealed very high porosity (Figure 8).
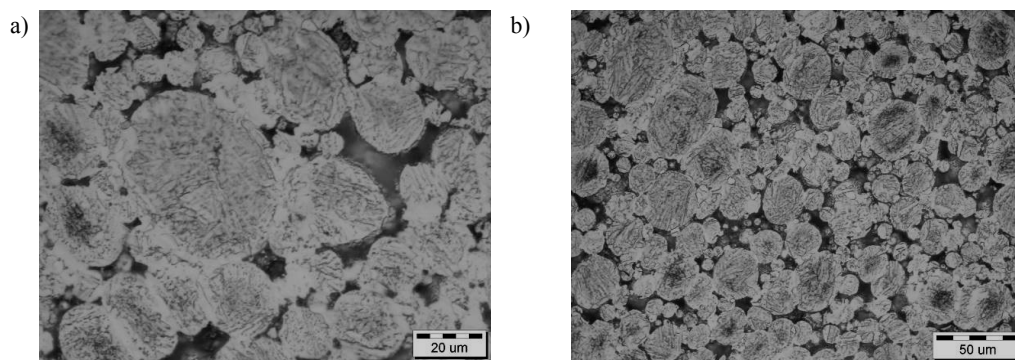

Fig. 8. Microstructure of Ti6Al4V titanium alloy powder compacted and sintered
for 0.5 h at temperature of 800 °C in plastic die

Summing up, compaction in a plastic die is highly troublesome, does not ensure proper density of the porous material and the pressure control depends on the plastic die material's melting point and flow. This method is unsuitable for consolidation of titanium alloy powders.

3.3. Hot compaction of powder in die under protective argon atmosphere

A special device was constructed to ensure the proper compaction of spheroidal powder produced by GA. The powder can be simultaneously compacted and sintered under protective argon atmosphere in this device (Figure 9).

Because of the high titanium powder compaction temperature, all the components were made of nickel alloy Inconel 625. The die consists of two parts: an external die and a split internal die (the latter is exchangeable and yields compacts 20 mm in diameter). The die rests on a corundum fitting and a top plate made of tool steel WCL. To the plate the die is secured with four M10 bolts. The split die is pushed out by four knockouts secured to one common fixture and shifted by a jack located as shown in Figure 9. High-temperature lubricant Molykote P37 was used to reduce friction between the dies. Because of similar operating conditions as those of the die, the knockouts were also made of Inconel 625. Their fixture was made of tool steel WCL.

The powder was compacted at a temperature of about a 800 °C. Because of the powder's high affinity to oxygen and nitrogen, compaction was conducted under argon shield. Owing to its higher density than that of air, argon pushes out air from the inside of the die. The air escapes in the place indicated by the arrow.
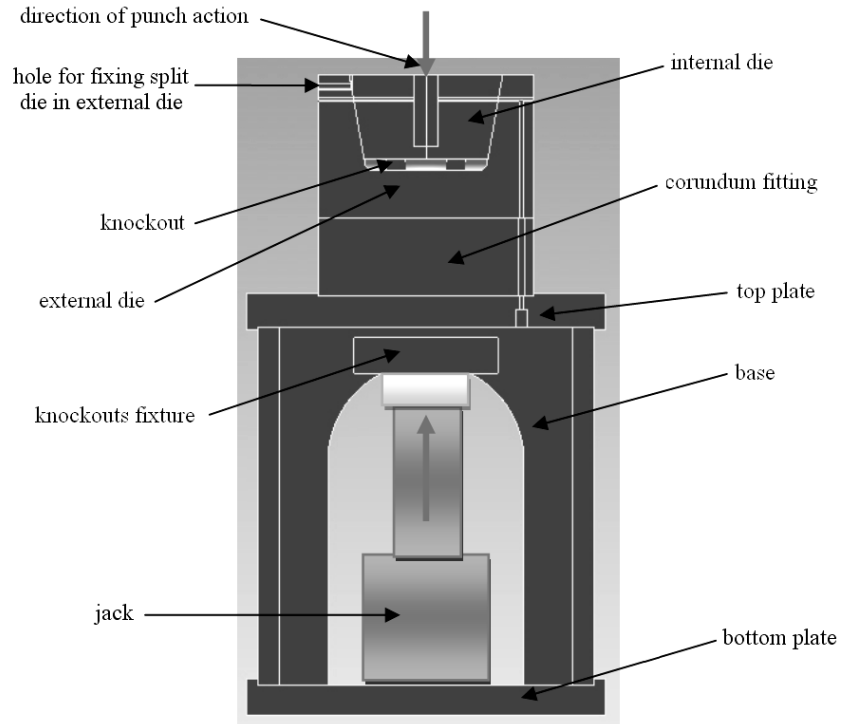
Fig. 9. Schematic of device for hot compaction of titanium powders

Induction heating and a specially made inductor were used in order to reach the set tool temperature appropriately quickly and obtain a uniform temperature distribution. 20×35 mm cylindrical specimens were yielded by the segment die, which were com-pacted at a temperature of 800 °C and soaked for 60 minutes under a pressure of 150 MPa.
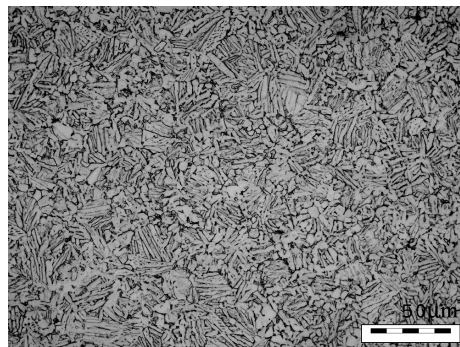
Fig. 10. Cross section of specimen made of Ti6Al4V titanium alloy powder hot compacted
at temperature of 800 °C under pressure of 150 MPa for 60 minutes

Density measurements and structural analyses showed that an almost solid material could be produced from Ti6Al4V titanium alloy powders in such conditions. The measured porosity amounted to 99.5% and was within the measuring error. Therefore it was assumed that the conditions were proper to obtain a solid material. This was confirmed by metallographic examinations – no pores were found in the microstructure (Figure 10).

Conclusions

1. The Ti6Al4V titanium alloy powder characterized by irregular geometry, produced by HDH, shows good cold compactibility. A pressure above 500 MPa is needed to produce a durable specimen. In the case of the spherical powder produced by GA, no durable specimens can be obtained by cold compaction.

2. For the Ti6Al4V titanium alloy powder produced by HDH there is no need to use cold compaction pressures higher than 550 MPa since when the latter value is exceeded the material's porosity after sintering is almost constant and amounts to about 5.7%.

3. Compaction in the plastic die is highly troublesome and it does not ensure proper density of the porous material. The pressure control depends on the melting point and flow of the material from which the plastic die is made. The method is unsuitable for consolidation of titanium alloy powders.

4. A special device, allowing the simultaneous compaction and sintering of powder under protective argon atmosphere, was constructed. A solid material was obtained from Ti6Al4V titanium alloy powders produced by GA. It seems that the proposed technology of compaction under argon atmosphere could be used (after some refinement) to manufacture products from titanium alloys on the industrial scale more economically since it combines compaction and sintering and does not require costly equipment.

References

[1] Cosmi F., Martinelli B., Valentini R.: *A mechanical and clinical evaluation of the Helix Wire for subcapital humerus fracture ostheosynthesis*, Acta of Bioengineering and Biomechanics, Vol. 6, No. 1, 2004, pp. 3–12.

[2] Chladek W., Hadasik E., Chladek G.: *Influence of surface modification on friction coefficient of the titanium–elastomer couple*, Acta of Bioengineering and Biomechanics, Vol. 9, No. 2, 2007, pp. 17–25.

[3] Long M, Rack HJ. *Titanium alloys in total joint replacement – a materials science perspective*, Biomaterials, 19, 1998, pp. 1621–1639.

[4] Czarnowska E., Wierzchoń T., Maranda-Niedbała A.: *Properties of the surface layers on titanium alloy and their biocompatibility in vitro tests*, Journal of Materials Processing Technology, 92–93, 1999, pp. 190–194.

[5] Wang G., Zhang K.F., Wu D.Z., Wang J.Z., Yu Y.D.: *Superplastic forming of bellows expansion joints made of titanium alloys*, Journal of Materials Processing Technology, 178, 2006, pp. 24–28.

[6] Kubiak K.: *Technological plasticity of hot deformed two-phase titanium alloys (in polish)*, Rzeszów 2004, 104.

[7] Niespodziana K., Jurczyk K., Jurczyk M.: *Titanium-Silica Nanocomposites: Preparation and Characterization*, Archives of Metallurgy and Materiale, Vol. 53/3, 2008, pp. 875–880.

[8] Fujita T., Ogawa A., Ouchi C., Tajima H.: *Microstructure and properties of titanium alloy produced in the newly developed blended elemental powder metallurgy process*, Material Science and Engineering, A213, 1996, pp. 148–153.

[9] Guden M., Celik E., Akar E., Cetiner S.: *Compression testing of a sintered Ti6Al4V powder compact for biomedical applications*, Materials Characterization, 54, 2005, pp. 399–408.

[10] Froes F.H., Ward-Close C.M.: *Processing of light metals for enhanced performance, Journal of Materials Processing Technology*, 48, 1995, pp. 667–673.

[11] Kim K.T., Yang H.C.: *Densification behavior of titanium alloy powder during hot Pressing*, Materials Science and Engineering, A313, 2001, pp. 46–52.

[12] Mamoru Mabuchi, Kohei Kubotal.: *New recycling process by extrusion for machined chips of AZ91 magnesium and mechanical properties of extruded bars*, Materials Transactions, 36, 1995, pp. 1249–1254.

[13] W. Chmura, Z. Gronostajski, *Bearing materials obtained by diffusion bonding of aluminium and aluminium bronze chips*, Archives of Civil and Mechanical Engineering, 2, 2007, pp. 53–66.

[14] Dybiec H.: *Plastic consolidation of metallic powders*, Archives of Metallurgy and Materiale Vol. 52 / 2, 2007, pp. 161–170.

[15] W. Smarsly: *Zusammenhang von Mikrostruktur und Umformbedingungen von Ti6Al4V Pulver beim "Matrizenverbundschmieden (MVS)"*. PhD Thesis, Rheinisch-Westfalischen Technischen Hochschule Aachen, 1985.

Wpływ prasowania na zimno i gorąco na proces zagęszczania proszku stopu tytanu Ti6Al4V

W pracy przeanalizowano trzy procesy przetwarzania proszków stopu tytanu Ti-6%Al-4%V: prasowanie z pływającą matrycą z różnym ciśnieniem próbek o średnicy 25 mm oraz spiekanie w piecu próżniowym, wytwarzania wyprasek osiowosymetrycznych na urządzeniu do prasowania z plastyczną matrycą, prasownie proszku w matrycy na gorąco w atmosferze ochronnej argonu. W badaniach zastosowano proszek Ti6Al4V otrzymywany dwiema metodami: HDH (hydride-dehydride) i gas atomization (GA). Zbudowane specjalne urządzenie, w którym jest możliwe jednoczesne prasowanie i spiekanie proszku w atmosferze ochronnej argonu, pozwo-

liło uzyskać z proszków stopu tytanu Ti6Al4V wytwarzanych metodą GA, lity materiał. Wydaje się, że opracowana technologia prasowania w atmosferze argonu, po odpowiednim dopracowaniu mogłaby posłużyć do bardziej ekonomicznego wytwarzania wyrobów z proszku stopów tytanu na skalę przemysłową, gdyż pozwala na połączenie procesu prasowania i spiekania oraz nie wymaga kosztownych urządzeń.

Modelling of the strand and mold temperature in the continuous steel caster

Z. MALINOWSKI, M. RYWOTYCKI

AGH University of Science and Technology, Al. Mickiewicza 30, 30-059 Kraków, Poland

The finite element 3D model has been developed to study the heat transfer and fluid flow in the mold region for the continuous steel casting. The strand and mold temperature is controlled by the heat transfer through steel – mold interface. The thermal resistance of interface layer has been modelled taking into consideration the convection heat transfer coefficient between the liquid steel and mold surface as an upper limit and the radiation heat transfer as a lower limit. An empirical equation has been derived to model heat conduction through the steel – mold interface. The computation has been performed to study the model response to thermal resistance of the mold –steel interface and the casting speed.

Keywords: *heat transfer, fluid flow, finite element method*

1. Introduction

In steel plants, which produce the hot rolled products, steel is continuously cast in the form of slabs. It is the most efficient technology used worldwide. Solidification of steel in the mold plays fundamental role in the sheet quality. Essential developments in the design of mold and casting technology have been observed in recent years. These include on-line control of the mold oscillation and the electromagnetic stir of the liquid steel. Quality of a mold material and taper design has been improved substantially [1]. The control of heat transfer in the mold and secondary cooling zones plays an essential role in the solidification of steel. The heat exchange limits the casting speed and essentially influences the formation of the solid shell [2]. A casting machine is a heat exchanger and heat is extracted from the solidifying steel by cooling water. However, the process of heat transfer is complex. It depends on heat convection and heat conduction in the steel-slag-mold system. Kinetic energy of liquid steel flowing from the nozzle causes mass movement and increases heat convection in the liquid region. In the mold a slag rim is formed on the plates. The thermal resistance of the slag rim and lubricant limits the heat flux transferred to the mold plates. The plates are made of copper or Cu-Ag, Cu-Cr-Zn alloys. Copper alloys improve strength and creep resistance of plates, however the conductivity is reduced. Vertical grooves are machined in plates on the side of the casing. It improves circulation of cooling water. The grooves dimensions and water velocity have direct impact on the heat transfer coefficient between cooling water and the mold plates. The described factors have been taken into consideration in the numerical model of heat transfer in continuous casting

of the square slab. The temperature fields of the mold and slab and the development of the solid shell have been analyzed.

2. The Heat and mass transfer models

2.1. Metal flow and heat transfer in the strand

The transfer of energy in the strand is composed of heat conduction in the solid shell and in the liquid core. In addition, in the liquid zone heat transfer take place by convection, which results from mass movement due to kinetic energy of pouring a molten metal into the mold [3]. Heat transfer by radiation in the liquid zone can be neglected and the strand temperature field is computed from the solution to the Equation [4]:

$$\frac{\partial T}{\partial \tau} + v_x \frac{\partial T}{\partial x} + v_y \frac{\partial T}{\partial y} v_z \frac{\partial T}{\partial z} = \frac{\lambda}{\rho c}\left(\frac{\partial^2 T}{\partial x^2} + \frac{\partial^2 T}{\partial y^2} + \frac{\partial^2 T}{\partial z^2}\right) + \frac{q_v}{\rho c}, \tag{1}$$

where:
  T – steel temperature, K,
  τ – time,
  s, v_x, v_y, v_z – steel velocity field, m/s,
  λ – thermal conductivity of steel, W/(m K),
  q_v – internal heat source, W/m^3,
  c – specific heat of steel, J/(kg K),
  ρ – steel density, kg/m^3,
  q_v – internal heat source, W/m^3.

In Equation (1) the velocity field describes movement of the liquid steel and the solid shell. The velocity field can be computed from the solution to the system of Equations [5]:

$$\frac{dv_x}{d\tau} = X - \frac{1}{\rho}\frac{\partial p}{\partial x} + \frac{\mu}{\rho}\left(\frac{\partial^2 v_x}{\partial x^2} + \frac{\partial^2 v_x}{\partial y^2} + \frac{\partial^2 v_x}{\partial z^2}\right),$$

$$\frac{dv_y}{d\tau} = Y - \frac{1}{\rho}\frac{\partial p}{\partial y} + \frac{\mu}{\rho}\left(\frac{\partial^2 v_y}{\partial x^2} + \frac{\partial^2 v_y}{\partial y^2} + \frac{\partial^2 v_y}{\partial z^2}\right), \tag{2}$$

$$\frac{dv_z}{d\tau} = Z - \frac{1}{\rho}\frac{\partial p}{\partial z} + \frac{\mu}{\rho}\left(\frac{\partial^2 v_z}{\partial x^2} + \frac{\partial^2 v_z}{\partial y^2} + \frac{\partial^2 v_z}{\partial z^2}\right),$$

$$\frac{\partial v_x}{\partial x} + \frac{\partial v_y}{\partial y} + \frac{\partial v_z}{\partial z} = 0, \tag{3}$$

where:

p – hydrostatic pressure, Pa,

X, Y, Z – mass forces, m/s^2,

μ – dynamic viscosity of steel, kg/(m s).

Equation (2) describes the motion of the steel in the control volume and Equation (3) gives the continuity condition of the metal flow. The motion of the liquid metal and the solid shell is forced by the withdrawal constant speed and a continuous molten steel feed. Thus, it is a case of the forced steady state flow and the influence of acceleration of gravity on the velocity field is neglected.

2.2. Boundary conditions

Solution to the general heat transfer Equation (1) should obey the boundary conditions specified on the steel surface. In the mold, on the steel – mold interface S_{sm} heat flux q_{sm} must be equal to:

$$q_{sm} = \alpha_{sm}(T_s - T_m) \text{ on } S_{sm}, \tag{4}$$

where:

α_{sm} – combined heat transfer coefficient, W/(m^2 K),

T_m – mold temperature, K,

T_s – steel temperature, K.

Below the mold on free surface of the strand S_{sf} convection boundary condition is specified and the heat flux q_{sf} can be expressed as

$$q_{sf} = \alpha_s(T_s - T_{ws}) \text{ on } S_{sf}, \tag{5}$$

where:

α_s – convection heat transfer coefficient for water spray cooling, W/(m^2 K).

Casting process consists of filling the mold with molten steel and its solidification. Below the meniscus level molten metal flows over the mold wall and convection is the main mechanism of heat transfer. Due to rapid cooling of the laminar layer of the liquid steel solidification starts and a gap between steel and mold is formed. For fully developed gap heat transfer mechanism changes to radiation. Thus, two boundaries for the heat transfer coefficient value can be prescribed. The upper bound is defined by the convection heat transfer coefficient α_l on the liquid steel – mold interface and the lover bound by the radiation heat transfer coefficient α_r in the gap. The value of α_r can be calculated taking into consideration radiation heat transfer between parallel plates,

$$\alpha_r = 5.67\ 10^{-8} \frac{\varepsilon_s \varepsilon_m}{\varepsilon_s + \varepsilon_m - \varepsilon_s \varepsilon_m} \frac{T_s^4 - T_m^4}{T_s - T_m}, \tag{6}$$

where:

ε_s – emissivity of the strand surface,

ε_m – emissivity of the mold surface.

Interface between mold and strand can be characterized by thermal contact conductance and the value of the heat transfer coefficient α_c is expressed by the empirical Equation

$$\alpha_c = (\alpha_l - \alpha_r) \exp \frac{T_s - T_{li}}{200}, \tag{7}$$

where:

α_l – convection heat transfer coefficient for liquid steel, W/(m^2 K).

Convection heat transfer coefficient α_l may vary from 500 to 2500 W/(m^2 K). Maximum value has been reported in [5]. The Nusselt relation due to Sleicher and Rouse [4] can be used to calculate α_l for liquid metals

$$Nu = 4.8 + 0.056 Re_s^{0.85} Pr_m^{0.93}. \tag{8}$$

The Reynolds number Re should be evaluated at the liquid steel bulk average temperature. The casting temperature can be used instead. The subscript m indicates that the Prandtl number Pr is to be calculated at the mold surface temperature.

Below the liquidus temperature combined conduction and radiation heat transfer take place as the gap between the mold and strip develops. In this stage of solidification decreases conduction and increases radiation process. However, decrease in the strip surface temperature lids to significantly slower heat exchange. Below the solidus temperature the combined heat transfer coefficient can be expressed as

$$\alpha_{sm} = \alpha_c + \alpha_r. \tag{9}$$

Typical distributions of the heat transfer coefficient are presented in Figure 1. Calculations have been performed for $\alpha_l = 2000$ W/(m^2 K), $T_m = 100$ °C, $\varepsilon_s = 0.8$, and $\varepsilon_m = 0.6$.

Outside the mold, strand is cooled by water sprays and the convection heat transfer coefficient α_s can be calculated from [6]:

$$\alpha_s = 10^9 3.15 w^{0.616} \left[700 + \frac{t - 700}{\exp(0.1t - 70) + 1} \right]^{-2.455} \left[1 - \frac{1}{\exp(0.025t - 6.25) + 1} \right], \tag{10}$$

where:

t – strand surface temperature, °C,

$\dot{w}$ – water spray flux rate, dm³/(m² s).

Presented in Figure 2 variation of the heat transfer coefficient as a function of strand temperature is typical for water cooling. For the water spray flux rate $\dot{w} = 3$ dm³/(m² s) and the strand surface temperature $t = 700$ °C the heat transfer coefficient $\alpha_s = 650$ W/(m² K). Similar values of heat transfer coefficient for water spray cooling have been reported in [7]. Meniscus surface temperature has been set equal to casting temperature $T_{in} = 1790$ K.
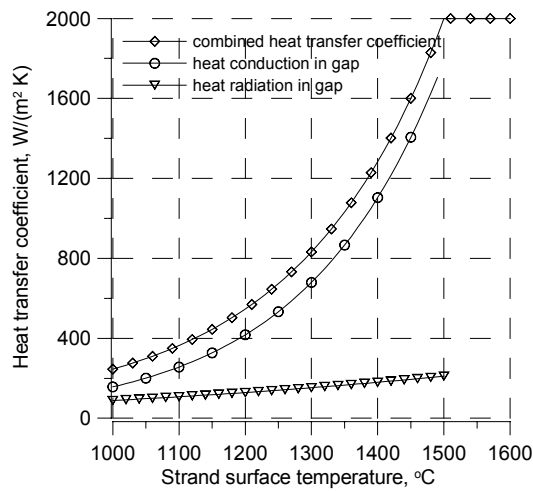

Fig. 1. Combined heat transfer coefficient on the steel – mold interface as a function of the strand temperature for $\alpha_l = 2000$ W/(m² K), $T_m = 100$ °C, $\varepsilon_s = 0.8$, and $\varepsilon_m = 0.6$

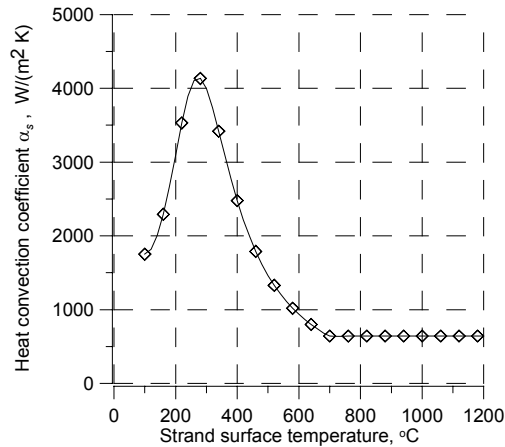Fig. 2. Distribution of the heat convection coefficient as a function of the strand surface temperature for the water spray flux rate $\dot{w} = 3$ dm³/(m² s)

Scheme of kinematical boundary condition for flow analysis has been presented in Figure 3. On free surface of the liquid steel two zones can be determined. In the first zone, which simulates the charging nozzle, normal velocity v_z is equal to pouring velocity v_{in} and tangent velocity $v_x = 0$. For the second zone the slip wall condition has been adopted and normal velocity v_z is set to zero. On the steel – mold interface the slip wall condition has been assumed and velocity v_x is set to zero, furthermore for the solid shell v_z equal to casting speed v_c is set. In the cross section of the strand below the mold for the solid shell $v_x = 0$ and $v_x = v_c$ have been prescribed and for the liquid steel only $v_x = 0$ has been assumed.
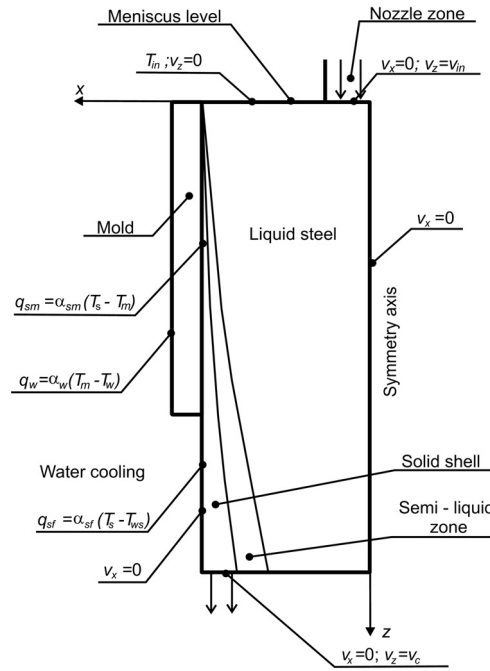
Fig. 3. Scheme of the continuous casting process and the boundary conditions
for steel flow and heat transfer models

2.3. The mold temperature model

Determination of the strand temperature field requires knowledge of the mold surface temperature T_s. Its value can be defined if the mold temperature field is known. The mold temperature field can be determined from the solution to the three dimensional heat transfer Equation

$$\frac{\partial T}{\partial \tau} = \frac{\lambda}{\rho c}\left(\frac{\partial^2 T}{\partial x^2} + \frac{\partial^2 T}{\partial y^2} + \frac{\partial^2 T}{\partial z^2}\right). \tag{11}$$

The mold is taking heat from the strand and is simultaneously water cooled on the outside surface. On the inner surface of mold the boundary condition has the form

$$q_{sm} = \alpha_{sm}(T_s - T_m) \text{ on } S_{sm}. \tag{12}$$

The heat transfer coefficient α_{sm} is defined in the same way as for the strand temperature model. Outer surface of the mold is water cooled and the heat flux is given by

$$q_w = \alpha_w(T_m - T_w) \text{ on } S_{sw}, \tag{13}$$

where:

α_w – is the heat transfer coefficient for water cooling in mold channels, $W/(m^2 K)$,

T_w – cooling water temperature, K.

Water cooling channels are machined in mold in a form of grooves of a side length 3 to 5 mm. Most relations for the heat transfer coefficient for turbulent flow are based on experimental studies. The Nusselt number relation due to Michiejew [8] can be used

$$Nu = 0.021 Re_w^{0.8} Pr_w^{0.43} \left(\frac{Pr_w}{Pr_s} \right)^{0.25}. \tag{14}$$

Subscript *s* indicates that the Prandtl number *Pr* must be evaluated at the mold surface temperature and subscript *w* denotes that the Reynolds *Re* and Prandtl *Pr* numbers are to be evaluated at the mean bulk temperature of water. Once the Nusselt number is known the convection heat transfer coefficient for water cooling is determined from

$$\alpha_w = \frac{Nu\lambda_w}{D_h}, \tag{15}$$

where:

D_h – hydraulic diameter of the water cooling channel, m,

λ_w – water conductivity, $W/(m K)$.

Several mold cooling strategies can be obtained varying the grooves dimensions and the distance between grooves [9].

3. Results and discussion

Finite element method has been chosen to solve the heat transfer and metal flow problems [3, 10]. Computer code has been developed to simulate the temperature and velocity fields in the continuous steel caster. Computations have been performed for

the mold of 160 mm × 160 mm cross section and 700 mm long. The mold corner radius has been assumed equal to 15 mm. Further, it has been assumed that mold is made of Cu-Ag alloy and cooling grooves with hydraulic diameter D_h = 4 mm are evenly distributed over the outer mold surface. Physical parameters of the mold material and cooling water are listed in Table 1.

Table 1. Physical properties of the mold material [1, 4] and cooling water [4] at room temperature

Material	Thermal conductivity W/(m K)	Density kg /m³	Specific heat J/(kg K)
Water	0.607	997	4180
Cu-Ag alloy	370	8900	400

The simulations have been performed for the bulk average velocity of cooling water v_w = 4.5 m/s. Chemical composition and properties of carbon steel used in computations are listed in Table 2 and Table 3, respectively.

Table 2. Chemical composition of the carbon steel used in simulation

Element	C	Si	Mn	P	S
wt. %	0.35	0.20	0.75	0.04	0.04

Table 3. Physical properties of the carbon steel used in simulation

Property	Unit	Value or function of temperature
Liquidus temperature [14]	°C	1500
Solidus Temperature [14]	°C	1460
Heat of solidification [11]	J/m³	10^9 1.93
Dynamic viscosity – liquid [12]	kg/(m s)	0.00285
Thermal conductivity – liquid [11]	W/(m K)	35
Density – liquid [13]	kg/m³	$\rho = \dfrac{1}{0.1235 + 12.67 \cdot 10^{-6} T + 9 \cdot 10^{-2} C}$
Specific heat – liquid [11]	J/(kg K)	574
Thermal conductivity – austenite [10]	W/(m K)	14.24+0.0127 t
Density – austenite [13]	kg/m³	$\rho = \dfrac{1}{0.1235 + 9.7 \cdot 10^{-6} T + 0.4 \cdot 10^{-2} C + 2 \cdot 10^{-2} C^2}$
Specific heat – austenite [10]	J/(kg K)	647.522+0.005852 t

Due to symmetry of the problem finite element simulations have been limited to ¼ of the steel – mold cross section. Finite element mesh of 3136 elements for steel temperature computation has been employed. In the case of mold temperature 855 elements have been used. Typical 8-node linear elements have been employed. The example of the finite element mesh is presented in Figure 4. For the velocity field computation 480 elements have been used in the longitudinal cross section of the strand. The steady state velocity field has been computed every 50th increment of the heat transfer solution. Since the heat transfer problem should converge to a steady

state solution the coupled problem has been solved iteratively. The computations of the strand temperature field have been performed as long as the difference between the current and previous temperature field was greater than the prescribed accuracy. Usually from 2000 to 5000 time increments ware needed to reach the steady state solution.

3.1. Cooling conditions analysis

The influence of the heat transfer from the strand surface on the steel temperature and velocity fields has been analyzed. In the strand temperature model there are two parameters which can be used to study this problem. The first one is the heat convection coefficient α_l and the second one is the water spray flux rate $\dot{w}$. In order to analyze heat transfer through steel – mold interface the computations have been performed for the cases of: $\alpha_l = 1000$, $\alpha_l = 1500$, $\alpha_l = 2000$ W/(m^2 K) and $\dot{w} = 3$ dm^3/(m^2 s). The water spray flux influence on the solidification process below the mold has been analyzed for the cases of: $\dot{w} = 3$, $\dot{w} = 5$, $\dot{w} = 10$ dm^3/(m^2 s) and $\alpha_l = 2000$ W/(m^2 K).The casting speed $v_c = 1.5$ m/min has been assumed in both cases.
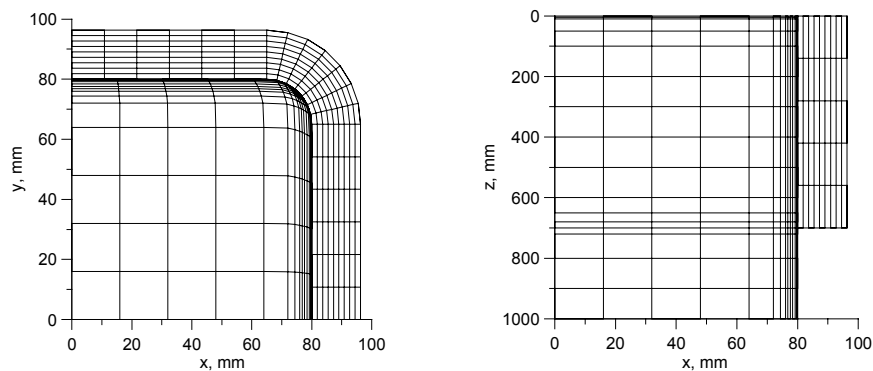
Fig. 4. The finite element mesh employed for heat transfer analysis

Thermal resistance of the mold–steel interface on the mold and strand temperature fields in the longitudinal section are presented in Figure 5.

Faster heat transfer through steel–mold interface results in significantly higher mold temperature. The maximum mold temperature rises to 250 °C in the zone of contact with the liquid steel. It limits further reduction of the thermal resistance of the mold–steel interface. The solid shell thickness is the highest for $\alpha_l = 2000$ W/(m^2 K) and is equal to 17 mm. For the heat transfer coefficient $\alpha_l = 1000$ W/(m^2 K) the solid shell thickness is 13.5 mm below the mold edge. The thermal resistance of the mold – steel interface has significant influence on the strand surface temperature. The results are shown in Figure 6. Below the mold edge the surface temperature in the middle of the strand side drops to 1250 °C for $\alpha_l = 1000$ W/(m^2 K) and to 1170 °C for $\alpha_l = 2000$

W/(m^2 K). Thus, thermal resistance of the mold–steel interface can be used to control the solidification process.

Fig. 5. The mold and strand temperature fields for
various thermal resistance of the mold–steel interface
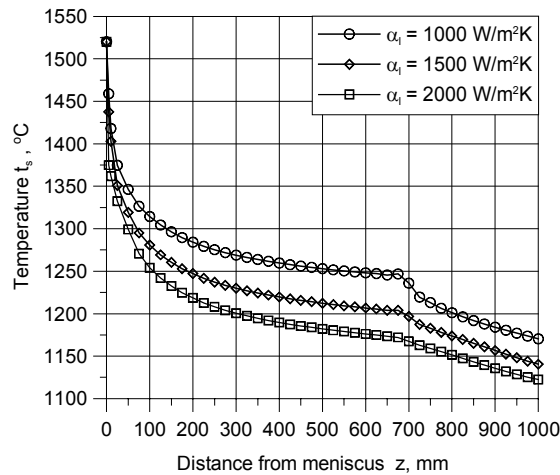
Fig. 6. The surface temperature variation in the middle of the strand side for
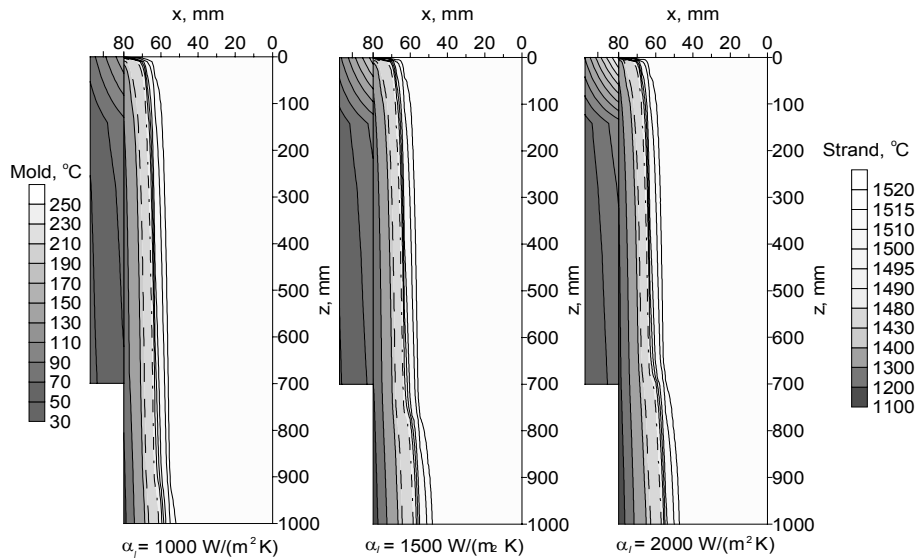various thermal resistances of the mold–steel interface

The mold temperature fields for various thermal resistance of the mold–steel interface have been presented in Figure 5 and Figure 7.
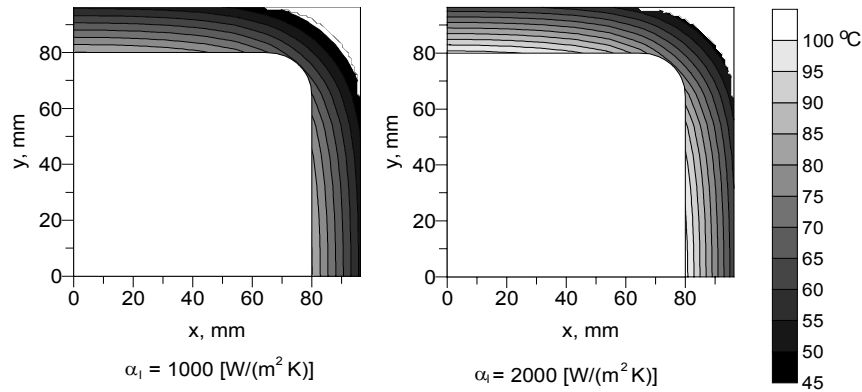
Fig. 7. The mold temperature fields in the cross 140 mm below the meniscus
for various thermal resistance of the mold–steel interface
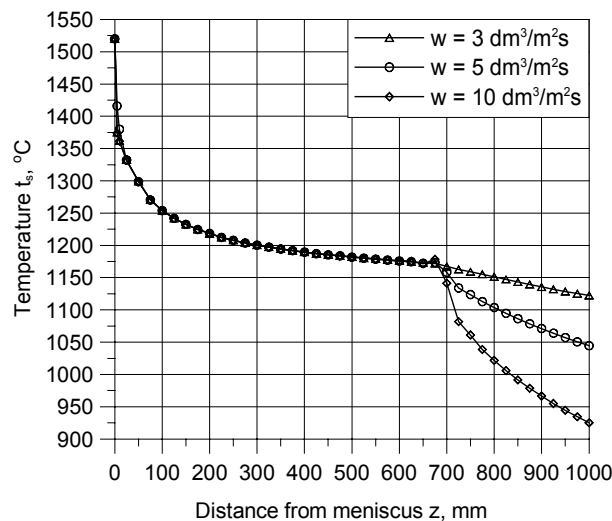
Fig. 8. The surface temperature variation in the middle of
the strand side for various water spray flux rates

The highest mold temperature is observed at surface which is in contact with the liquid steel. The mold surface temperature drops as the gap develops in the flow direction. In the mold cross section the temperature distribution is les or more uniform with the lowest values at the mold corner. Even distribution of cooling channels over the outer mold surface results in uniform heat transfer to the cooling water. Other cooling schemes are possible in order to control the mold temperature [9]. It has been shown that the thickness of the solid shell can be controlled by the convection heat transfer coefficient which is directly related to liquid steel flow down the mold. Simple empirical equation has been developed to describe the combined heat transfer at

the mold–steel interface. This equation can be easily adapted to a particular casting machine if the results of mold thermal monitoring are known. Below the mold, the strand temperature can be controlled by the water sprays applied to the strand surface. The effect of the water spray flux rate on the strand temperature is further explored in simulation, which has been performed for α_l = 2000 W/(m^2 K), casting speed v_c = 1.5 m/min and the water spray flux rates: $\dot{w}$ = 3, $\dot{w}$ = 5, $\dot{w}$ = 10 dm^3/(m^2 s). The results are shown in Figure 8. The model is sensitive to the water spray cooling. The strand temperature drops significantly below the mold while along the mold the temperature remains constant. The solid shell thickness increases from 17 mm for $\dot{w}$ = 3 dm^3/(m^2 s) to 19 mm for $\dot{w}$ = 10 dm^3/(m^2 s), respectively.

3.2. Casting speed analysis

The casting speed influence on the steel solidification has been analyzed for the thermal resistance of the mold – steel interface characterized by the convection heat transfer α_l = 1500 W/(m^2 K) and the water spray flux rate in the secondary cooling chamber $\dot{w}$ = 3 dm^3/(m^2 s). The computation has been performed for the casting speed varying from 1.5 to 3.5 m/min at intervals of 0.5 m/min. The mold and strand temperature fields are presented in Figure 9. Increase in the casting speed lids to a shorter cooling time and in consequence the strand temperature rises. In Figure 10 variation of the strand temperature in the middle of the strand side are shown. Below the mold the strand surface temperature rises by about 50 °C as the casting speed is increased from 1.5 to 3.5 m/min. The thickness of the solid shell decreases from 16 mm for the lowest casting speed to 9.5 mm for the highest casting speed. Significant reduction of the solid shell thickness may lead to surface defects such as cracks or folding back of the solidified rim. The simulations have shown significant influence of the velocity field on the strand temperature. The heat transfer and fluid flow problems are highly coupled and stationary results can be obtained after substantial increase in the computation time.

The temperature fields in the mold cross section 140 mm below the meniscus are presented in Figure 11. The mold temperature rises as the casting speed increases. The results confirm good predictive ability of the developed mold temperature model. The mold temperature rise is caused by a higher strand surface temperature and the heat flax increase. The maximum mold temperature rises by about 15 °C as the casting speed increases from 1.5 to 3.5 m/min.

Lack of the experimental data makes the comparison of the calculated temperature to measurements impossible. The accuracy of the computation can be validated on the thickness of the solidified shell for typical values of the heat transfer coefficient from the range of 1000 to 3000 W/m^{2}K. The value of the heat transfer coefficient can be chosen only for a particular casting machine based on the measurement of the cooling water temperature.

Fig. 9. The mold and strand temperature fields for the casting speed v_c = 1.5 m/min and v_c = 3.5 m/min
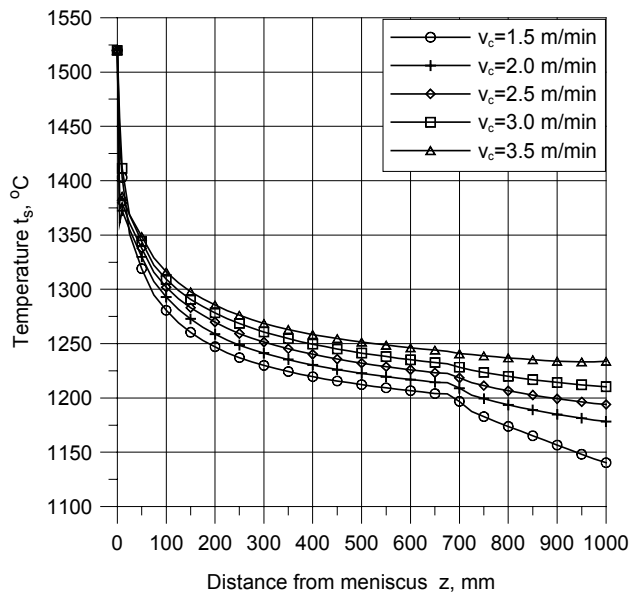
Fig. 10. The surface temperature variation in the middle of the strand side for various casting speeds
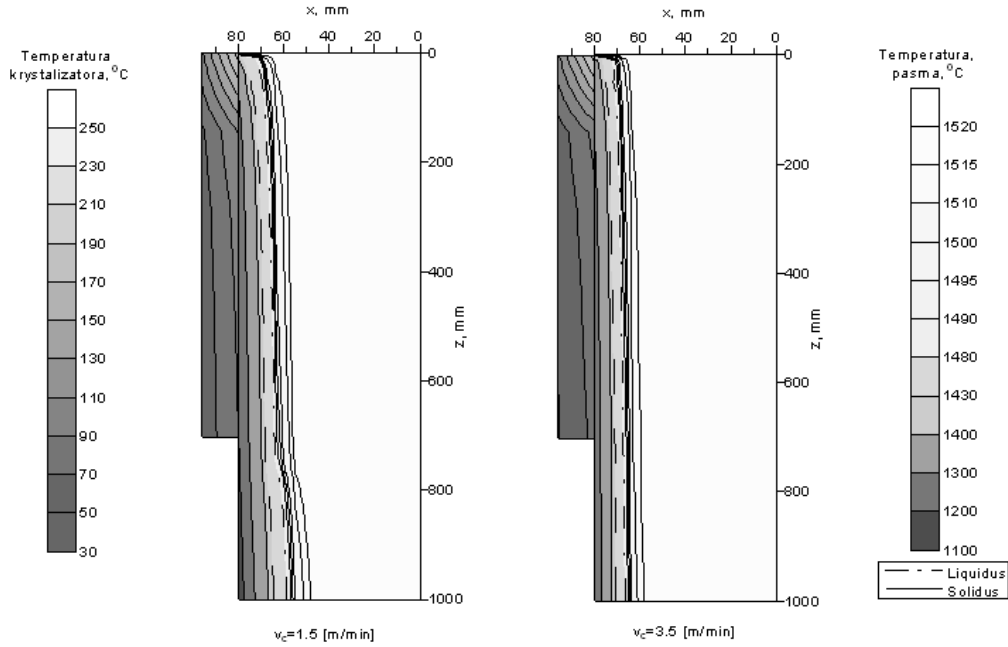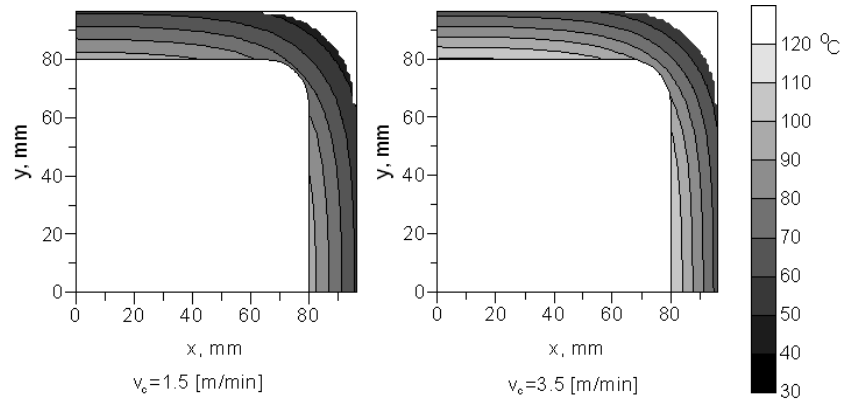
Fig. 11. The mold temperature fields in the cross section 140 mm below the meniscus
for the casting speed v_c = 1.5 m/min and v_c = 3.5 m/min

4. Conclusions

In the literature several solutions to the solidification of steel in the mold region
has been published. However, the problem is not well understood. The main
difficulties are concerned with the description of the heat transfer through the steel–
mold interface and with the determination of fluid flow. The heat transfer and fluid
flow problems are highly coupled and heat convection in the liquid region makes
serious problems while the temperature field is computed. The solution should
converge to a steady state and only at this stage it can be assumed as the final one.
Negligence of heat convection may cause essential inaccuracy in the strand
temperature field. In consequence the steel solidification and formation of the solid
shell is predicted with low accuracy. The empirical equation has been derived to
solve the heat transfer problem through the steel–mold interface. The upper limit of
the heat transfer coefficient has been determined based on the heat convection by the
liquid steel flowing down the mold. The lower limit for the heat transfer coefficient
sets the heat radiation in the gap. The computations have shown good response of
the finite element solution to the thermal resistance of the steel–mold interface,
water spray cooling in the secondary chamber and to the casting speed. Predictions
of the finite element 3D model are consistent with results published in the literature.
Further effort has to be done in order to limit the computation time and to improve
description of the boundary conditions.

Acknowledgements

References

[1] Normanton S., Watson P., Hardwick N.: *Some developments in mould technology*, [in:] Proc. 3rd European Conference on Continuous Casting, Madrid, 1998, pp. 737–743.

[2] Dilellio J.A., Young G.W.: *An asymptotic model of the mould region in continuous steel caster*, Metallurgical Transactions, 26, 1995, pp. 1225–1241.

[3] Rywotycki M., Malinowski Z.: *Modelling of fluid flow in the steel continuous casting process*, Metallurgy and Foundry Engineering, 30, 2004, pp. 99–108.

[4] Çengel Y.A.: *Heat and Mass Transfer: a practical approach*, McGraw-Hill, New York, 2007.

[5] Malczewski J., Piekarski M.: *Modele procesów transportu masy pędu i energii*, PWN, Warszawa, 1992.

[6] Hodgson P.D., Browne K.M., Collinson D.C., Pham T.T., Gibbs R.K.: *A mathematical model to simulate the thermo-mechanical processing of steel*, [in:] Proc. 3rd Int. Seminar of the International Federation for Heat Treatment and surface Engineering, Melbourne, 1991, pp. 139–159.

[7] Park J.K., Thomas B.G., Samarasekera I.V.: *Analysis of thermo mechanical behaviour in billet casting with different mold corner radii*, Ironmaking and Steelmaking, 29, 2002, pp. 359–375.

[8] Wiśniewski S., Wiśniewski T.S.: *Wymiana ciepła*, WNT, Warszawa, 1994.

[9] Rywotycki M., Malinowski Z., Telejko T.: *Wpływ konstrukcji krystalizatora na pole temperatury pasma COS*, Hutnik – Wiadomości Hutnicze, 4, 2006, pp. 142–147.

[10] Malinowski Z.: *Numeryczne modele w przeróbce plastycznej i wymianie ciepła*, UWND AGH, Kraków, 2005.

[11] Kurz W., Fisher D.J.: *Fundamentals of Solidification*, Trans. Tech. Publications, Switzerland, 1998.

[12] Kniaginin G.: *Staliwo – Metalurgia i Odlewnictwo*, Śląsk, Katowice, 1972.

[13] Theret J., Lesoult G.: *Deroulement de la solidification des fonts a graphite spheroidal*, Hommes et Fonderie, Fevrier, 4, 1984, pp. 19–30.

[14] Beranger G., Henry G., Sanz G.: *The Book of Steel*, Intercept Ltd., New York, 1996.

Modelowanie pola temperatury pasma i krystalizatora COS

W pracy przedstawiono model numeryczny opisujący wymianę ciepła pomiędzy krystalizatorem a pasmem w procesie ciągłego odlewania stali. Analizie poddano wpływ warunków wymiany ciepła w obszarze krystalizatora na pole temperatury pasma. Wykonano obliczenia pozwalające ocenić wpływ prędkości odlewania na pole temperatury krystalizatora i pasma. Zadanie rozwiązano z zastosowaniem metody elementów skończonych.

Problems of numerical simulation of stress and strain in the area of the adhesive-bonded joint of a conveyor belt

D. MAZURKIEWICZ

Lublin University of Technology, ul. Nadbystrzycka 36, 20-618 Lublin, Poland

Belt conveyors are commonly used in-factory transportation devices built of sections of belt (e.g., a fabric-rubber belt) bonded into a continuous loop. Conveyor belt joints are exposed to substantial dynamic loads during the long time of their operation. Taking into account the fact that ensuring a high durability of conveyor belt joints is tantamount to guaranteeing their reliable operation and that the results of research conducted so far fail to provide unambiguous solutions to a number of problems that emerge in this case, it is advisable that advanced studies using computer techniques should be conducted within this area. Of particular help in the search for new structures and optimum methods for joining conveyor belt sections is finite element analysis, which, however, entails a number of problems. This paper describes the circumstances of occurrence of these problems and potential solutions to them. One important problem in FEM modeling is appropriate definition of the models of the analyzed materials. In the case of conveyor belt adhesive-bonded joints composed of rubber and a gum rubber adhesive, the analyses found in the literature, as a general rule, assume the hyperelastic material model based on the Mooney-Rivlin law, which, however, is a fairly arbitrary choice made without verification against actual strength test data. Rubber is a unique material, capable of very large deformations, by virtue of which it is counted among hyperelastic materials. Such materials require appropriate constitutive models and a reliable choice thereof in each particular case. Adequately precise modeling of the behavior of rubber materials still remains an open question. However, access to strength test data makes it possible to check experimentally which of the available theoretical models best reproduce the behavior of the modeled material. For that purpose, the available hyperelastic material models were tested separately for each constituent rubber material of the analyzed conveyor belt adhesive joint. The models were assessed with regard to the degree of their conformity with experimental data by analyzing the behavior of the hyperelastic material in a given case based on the constructed reaction curves using selected strain energy potentials for the available test data.

Keywords: *adhesive-bonded joint, rubber material models, hyperelastic materials, numerical modelling*

1. Introduction

Belt conveyors are basic in-factory transportation devices that are used by various production and service companies. Belt transport, due to a number of its merits, is used in numerous branches of industry, including, among others, mineral processing plants, metals-producing, extractive, cement-and-lime, and paper industries, sea and inland ports, construction industry, power plants, transshipment points, as well as agriculture and sugar plants. Belt conveyors (Figure 1) enable fast and efficient transport of loose materials of different physical-mechanical properties, with a low degree of their degradation during high-speed and long-distance transfer [1–7].

Conveyor belts, which are continuous loops, are made up of sections joined by cold vulcanization (bonding) or heat curing. Joining of belts using these methods is a toilsome activity, which, however, ensures a high, though not always sufficient, strength of the joint. In high-performance belt transport systems, multi-ply belts are joined using stepped lap joints (Figure 2). Joining of belt sections is an important issue and a problem for persons working in belt conveyor maintenance services as belts require constant shortening, lengthening, or relocation, which is connected with making ever new joints, not only as a result of service activities. The particular significance of this issue does not only follow from the growing number of long conveyors which transport, at a high speed, vast bulks of different kinds of materials, but is also connected with the large number of new belt section joints made every year. According to data from FTT Stomil Wolbrom plc. [8], this company's service currently makes an average of over 1000 belt joints a year both in Poland and abroad.

Fig. 1. A typical belt conveyor structure used for in-factory transport [9]

The quality of joints made in that way is often different even for one conveyor as it depends on a number of factors including the structure of the joint, the joining method, and the properties of the materials used as well as the care on the part of the staff to retain the technological parameters of these materials as included in the manufacturers' instructions manuals.

To ensure proper strength of a typical adhesive joint, a number of studies and analyses are normally carried out in the areas of maintenance, joining technology, and the possibilities of monitoring and assessment of the durability of the joint in industrial

conditions [6, 7, 11–16]. It results from the broad range of issues connected with adhesive bonding which involve the theory of adhesion, adhesive manufacturing technology, and adhesive joining technology. As Godzimirski [17] observes, when an analysis of the strength of adhesive joints is carried out, an account should be taken not only of their short-term strength, but also of their long-term strength, fatigue strength, resistance to dynamic loading, the effect of aging on their load capacity, etc.
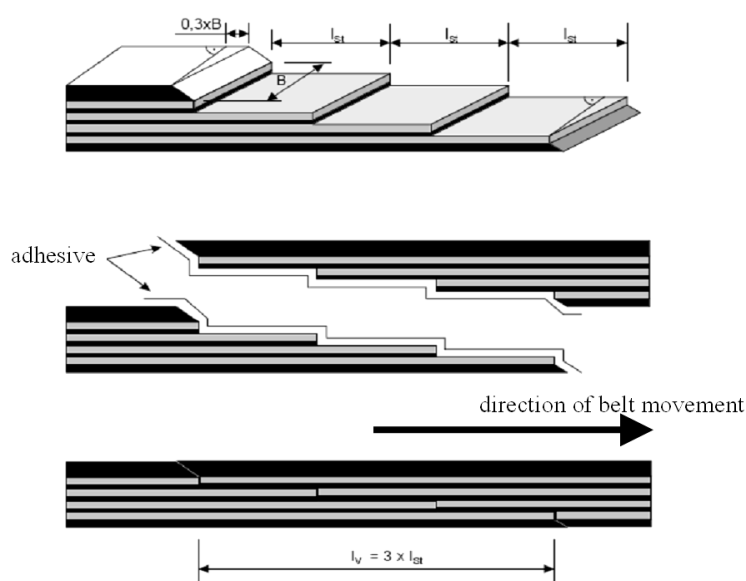
Fig. 2. A diagram of a method of joining a four-ply belt in accordance with
a brochure of Metso Minerals company [10]

These problems are particularly important in the case of conveyor belt joints, which are exposed to significant dynamic loads over the long period of their operation. Taking into account the fact that ensuring a high durability of conveyor belt joints is tantamount to guaranteeing their reliable operation and that the results of research conducted so far fail to provide unambiguous solutions to a number of problems that emerge in this case, it is advisable that advanced studies using recent developments in computer techniques should be conducted within this area. Of particular help in the search for new structures and optimum joining of conveyor belt sections is finite element analysis, which, however, entails a number of problems, the circumstances of the occurrence of which and potential solutions to which are described in this publication.

2. The goals of numerical analysis of belt joints

The most important problems of belt transport in the current period are issues concerning the necessity to reduce energy consumption and to increase durability. Par-

ticularly significant is the strength and durability of conveyor belt joints since, despite numerous research and implementation studies, it still constitutes an important problem that every belt conveyor user has to face. One of the possibilities of increasing the durability of the belt and its joints is, among others, reduction of longitudinal stresses in the belt. According to Jabłoński [18, 19], studies of fatigue life of joints indicate a strong effect of longitudinal stresses in the belt on its durability and strength. That is why a lot of design work is being carried out which aims at working out appropriate tensioning device solutions. A second potential direction of research in this case is one aimed at increasing the durability and strength of the joint between belt sections by means of analysis and assessment of the distribution of stresses in the joint and the influence that the very structure of the joint has on them. In this case, interesting results may be expected from the use of the finite element method.

In all types of structures in which adhesive-bonding has been used as a method for joining elements, the durability of the joint should be treated as one of the basic indexes of their operational usefulness. A potential solution to this problem is looking for the indispensable information by analyzing the distribution of stresses and strains in the joining area using numerical methods. It can be expected here that identification of stresses and strains in the adhesive joint will allow its appropriate design, selection of constituent materials and their properties, and will make possible specification of the manner in which the joint should be made in a purely structural context. An appropriate analysis may be conducted by means of numerical modelling using the classical method of finite elements, which is a calculation method based on matrix arithmetic [20]. The relations between forces and displacements are expressed in this method by means of the stiffness matrix, whose constituent elements include material constants describing the mechanical properties of the modelled materials.

3. Numerical analysis of stress and strain in the conveyor belt joint

Numerical analysis used in developing new design solutions for belt joints is aimed, among others, at estimating the possibility of using the developed FEM model of a joint for predicting the durability and strength of the joint as well as the possibility of using it at the stage of structural designing of the joint. It can be expected that the use of FEM-based numerical simulation in this case will enable precise analysis of stress distribution in the joining area of the selected conveyor belt, thus making possible the identification of areas of stress concentration or a stress distribution that would be unfavorable from the point of view of joint durability. It is believed [21] that this method can be treated as a significant expansion and supplementation of the analytical methods for assessing stress and strain, and as one that simultaneously allows reliable and precise determination of the share of the individual stress components, which, as a rule, constitutes important information in the design and optimization of adhesive joints. Of no mean significance is also the possibility this type of modelling gives of predicting the strength of adhesive joints of different geometry and different constitu-

ent material parameters without the need to use troublesome and, in the case of conveyor belts, expensive destructive tests.

To conduct a strength analysis based on determining stress and strain in the area of the analyzed adhesive joint connecting conveyor belt sections, two models of the joint were worked out and subjected to numerical analysis according to the assumed goal using material data obtained during strength tests. At the stage of numerical modelling, von Mises stresses (reduced stresses) were analyzed, which in a uniaxial stress state (stretching of the belt joint) caused identical effort as the corresponding complex stress state represented by them. The reduced stresses in the analyzed case were determined on the basis of the Huber-Mises-Hencky (H-M-H) hypothesis:

$$\sigma_{red} = \frac{\sqrt{2}}{2}\sqrt{(\sigma_1 - \sigma_2)^2 + (\sigma_2 - \sigma_3)^2 + (\sigma_3 - \sigma_1)^2}, \tag{1}$$

where:

σ_1, σ_2, σ_3 are principal stresses.

3.1. The scope of calculations and numerical characteristics of an adhesive joint

The finite element method, belonging to a group of most popular computer-aided methods used for solving mechanical issues, consists in replacing a continuous model of the analyzed mechanical system with its discrete model (Figures 3 and 4), which in a mathematical description assumes the form of a set of algebraic Equations [22].
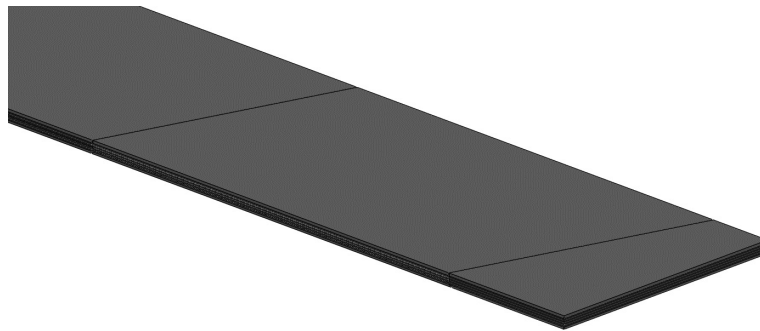

Fig. 3. A general view of a fragment of a spatial FEM model
of an adhesive-bonded joint of a conveyor belt

An important issue in FEM modelling is appropriate definition of the models of the analyzed materials. In the case of rubber and gum rubber adhesives, the analyses found in the literature usually employ the hyperelastic material model based on the

Mooney–Rivlin law [11, 23–27], which, however, is a fairly arbitrary choice made without verification against actual strength test data.
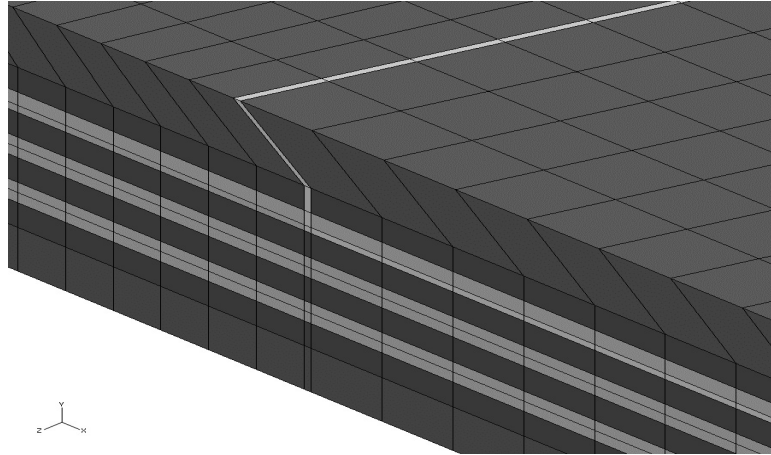

Fig. 4. A fragment of a sample spatial model of an adhesive-bonded joint

Rubber, however, is a unique material, capable of very large deformations, by virtue of which it is counted in the category of hyperelastic materials, requiring appropriate constitutive models and a reliable choice of those models in each particular case. Hyperelasticity is defined [28] as the ability of a material to undergo large elastic deformation under small forces, without losing its original properties. A hyperelastic material shows non-linear behaviour, which means that its deformation is not directly proportional to the load applied. Linear models of elasticity, totally inadequate in the discussed case, assume a linear strain-stress relation and small deformation values. Rubber, on the other hand, as a material having a high elastic deformation, is analyzed as a separate material group. That is why in the last decade a number of publications [26–31] have been devoted to the issues of rubber materials, their models, and the modelling of their behaviour in different structures and conditions. In spite of this significant number of publications in reputed international scientific journals and books, adequately precise modelling of the behaviour of rubber materials, as Diani et al. [26] note, still remains an open question. What we have at our disposal are a number of mathematical models describing the behaviour of such materials, which were developed over the past century starting from the time when Mooney presented his theory of large elastic deformations.

Modelling and design of hyperelastic materials, then, involve such activities as the selection of an appropriate strain energy function and accurate determination of material constants for such a function. In the available publications, the selection of models for modelling particular hyperelastic materials is usually a matter of an arbitrary decision. This is frequently the first, basic error which leads to an inadequacy of the results

of modelling since, after all, rubber is a specific material, whose properties are as a rule quite diversified dependent on its composition or content of special additives. Having data from strength tests, one can check experimentally which of the available theoretical models best represent the behaviour of the modelled material.

For that purpose, the available hyperelastic material models [23, 26–28, 32–34] were tested separately for each constituent rubber material of the analyzed conveyor belt adhesive joint, and the degree of their conformity with experimental data was assessed by analyzing the behaviour of the hyperelastic material in a given case on the basis of the constructed reaction curves using selected strain energy potentials for the available test data. Such procedure follows from the earlier analyzed fact that hyperelastic materials are described in terms of the strain energy potential $U(\varepsilon)$ [32], which defines the strain energy stored in the material per unit of reference volume (volume in the initial configuration). As mentioned before, several forms are used to describe this quantity, which enables effective modelling of the analyzed class of materials. The forms include the Arruda–Boyce form, the Marlow form, the Mooney–Rivlin form, the neo-Hookean form, the Ogden form, the polynomial form, the reduced polynomial form, the Yeoh form, and the Van der Waals form [23, 26–28, 32–35]:

a) The Arruda–Boyce model, according to which the strain energy potential is defined by the relation:

$$U = \mu \left[\frac{1}{2}\left(\bar{I}_1 - 3\right) + \frac{1}{20\lambda_m^2}\left(\bar{I}_1^2 - 9\right) + \frac{11}{1050\lambda_m^4}\left(\bar{I}_1^3 - 27\right) + \frac{19}{7000\lambda_m^6}\left(\bar{I}_1^4 - 81\right) + \frac{519}{673750\lambda_m^8}\left(\bar{I}_1^5 - 243\right)\right] + \frac{1}{D}\left(\frac{J_{el}^2 - 1}{2} - \ln J_{el}\right),$$ (2)

where:

   U is strain energy per unit of reference volume,

   μ, λ_m and D are temperature-dependent material parameters,

   $\bar{I}_1$ is the first deviatoric strain invariant defined as $\bar{I}_1 = \bar{\lambda}_1^2 + \bar{\lambda}_2^2 + \bar{\lambda}_3^2$, where $\bar{\lambda}_1$ is

a deviatoric stretch defined by the relation $\bar{\lambda}_i = J^{-\frac{1}{3}}\lambda_i$, J is the total volume ratio, J_{el} is the elastic volume ratio, and λ_i are the principal stretches. The relation between the initial shear modulus μ_0 and μ is specified by the Equation:

$$\mu_0 = \mu\left(1 + \frac{3}{5\lambda_m^2} + \frac{99}{175\lambda_m^4} + \frac{513}{875\lambda_m^6} + \frac{42039}{67375\lambda_m^8}\right).$$ (3)

The constitutive model for the large stretch behaviour of rubber elastic materials proposed by Arruda and Boyce in 1993 is also often referred to as the eight-chain

model because it was derived by idealizing a polymer as eight elastic chains inside a volume element. The strain-stress function was based on the eight-chain representation of the macromolecular structure of rubber.

b) the Marlow model, in which the form of the strain energy potential is

$$U = U_{dev}(\bar{I}_1) + U_{vol}(J_{el}),$$
(4)

where:

U is the strain energy per unit of reference volume, with U_{dev} as its deviatoric part, and U_{vol} as its volumetric part. The deviatoric part is specified by providing uniaxial, equibiaxial or planar test data. The volumetric part, on the other hand, is specified by providing volumetric data, defining the Poisson's ratio or specifying the lateral strains together with providing test data used for specifying the deviatoric part of the strain energy potential.

c) The Mooney–Rivlin model, in which the strain energy potential is defined by the relation:

$$U = C_{10}(\bar{I}_1 - 3) + C_{o1}(\bar{I}_2 - 3) + \frac{1}{D_1}(J_{el} - 1)^2,$$
(5)

where:

C_{10}, C_{01} and D_1 are temperature-dependent material parameters,

$\bar{I}_2$ is the second deviatoric strain invariant defined as $\bar{I}_2 = \bar{\lambda}_1^{(-2)} + \bar{\lambda}_2^{(-2)} + \bar{\lambda}_3^{(-2)}$.

d) The Neo-Hookean Model, defining the strain energy potential as:

$$U = C_{10}(\bar{I}_1 - 3) + \frac{1}{D_1}(J_{el} - 1)^2.$$
(6)

e) The Ogden Model, in which the form of the strain energy potential for hyperelastic materials and for high values of incompressible deformations of rubber-like solids is:

$$U = \sum_{i=1}^{N} \frac{2\mu_i}{\alpha_i^2}(\bar{\lambda}_1^{\alpha_i} + \bar{\lambda}_2^{\alpha_i} + \bar{\lambda}_3^{\alpha_i} - 3) + \sum_{i=1}^{N} \frac{1}{D_1}(J_{el} - 1)^{2i},$$
(7)

where:

N is a material parameter,

μ_i, α_i, D_1 are temperature-dependent material parameters definable in experimental tests.

The polynomial form, in which the strain energy potential can be expressed as a polynomial.

$$U = \sum_{i,j=1}^{N} C_{ij}(\bar{I}_1 - 3)^i (\bar{I}_2 - 3)^j + \sum_{i=1}^{N} \frac{1}{D_i}(J_{el} - 1)^{2i}, \tag{8}$$

where:

C_{ij} is a temperature-dependent material parameter.

f) The reduced polynomial strain energy potential of the form:

$$U = \sum_{i=1}^{N} C_{i0}(\bar{I}_1 - 3)^i + \sum_{i=1}^{N} \frac{1}{D_1}(J_{el} - 1)^{2i}, \tag{9}$$

where:

C_{i0} is a temperature-dependent material parameter.

g) The Van der Waals model, which describes the strain energy potential as the relation:

$$U = \mu\left\{-(\lambda_m^2 - 3)[\ln(1-\eta) + \eta] - \frac{2}{3}a(\frac{\tilde{I}-3}{2})^{\frac{3}{2}}\right\} + \frac{1}{D}\left(\frac{J_{el}^2 - 1}{2} - \ln J_{el}\right), \tag{10}$$

$$\tilde{I} = (1-\beta)\bar{I}_1 + \beta\bar{I}_2, \tag{11}$$

$$\eta = \sqrt{\frac{\tilde{I}-3}{\lambda_m^2 - 3}}, \tag{12}$$

where:

μ is the initial shear modulus,

a is an interaction parameter,

β is a material constant,

D is the compressibility.

h) The Yeoh Model, defining the strain energy potential as a function:

$$U = C_{10}(\bar{I}_1 - 3) + C_{20}(\bar{I}_1 - 3)^2 + C_{30}(\bar{I}_1 - 3)^3 +$$
$$\frac{1}{D_1}(J_{el} - 1)^2 + \frac{1}{D_2}(J_{el} - 1)^4 + \frac{1}{D_3}(J_{el} - 1)^6, \tag{13}$$

where:

C_{i0} and D_i are temperature-dependent material parameters.

The models described above are in many cases related to one another. For instance, the reduced polynomial model and the Mooney–Rivlin model can be treated as special cases of the polynomial model. The Yeoh and the Neo-Hookean strain energy potentials can be construed as special cases of the reduced polynomial form. The particular material models of the Mooney–Rivlin and the Neo-Hookean form can, in turn, be derived from the general form of the Ogden strain energy potential for special choices of μ_i and α_i [32].

As stated in the literature [32, 35], generally, when data from multiple experimental tests are available (typically, this requires at least uniaxial test data), the Ogden and the Van der Waals forms fit experimental results more accurately. If the available test data are limited, the Arruda–Boyce, the Van der Waals, the Yeoh, or reduced polynomial forms provide a sufficiently accurate and satisfactory representation of the behaviour of a material. When only one set of test data is available, the use of the Marlow form is recommended since, in this case, a strain energy potential is constructed that will reproduce the test data exactly and will show reasonable behaviour of the modelled material in other deformation modes.

As appears from the strength-test-data-based analysis of the above-described individual hyperelastic models of rubbers making up the conveyor belt joint and the assessment of the magnitude of the approximation error, the best representation and stability of the model in the analyzed case, both for the external (cover) rubber material and the internal (carcass) rubber, was obtained using the Marlow model (Figures 5 and 6).

For the rubber adhesive, on the other hand, the best results were obtained when using the Mooney–Rivlin model. The same characteristics of the models of materials making up the analyzed joint were adopted at the stage of numerical modelling. Additionally, however, to compare the obtained results, an analysis was conducted, during FEM modelling of the adhesive-bonded joint of a rubber-fabric conveyor belt, of a model in which the adhesive layer was characterized as an elastic-plastic material.

3.2. A FEM model of the analyzed adhesive joint

In accordance with the results of the earlier-described analysis, elastic-plastic and nonlinear-elastic (hyperelastic) material models were used for the numerical calculations, on account of the non-linear properties of the materials occurring in the analyzed joint. In the case of the analyzed fabric, it was decided that linear-elastic material characteristics should be used.

The calculations were fully non-linear and involved both physical and geometric nonlinearity. The non-linear geometric problem was analyzed by using incremental-iterative computation techniques based on the Newton–Raphson method. This method enables very precise calculations in cases of large deformations, typical for rubber materials, because it is based on non-linear geometrical Equations that take into account the non-linear relations between displacements and deformations. Physical (ma-

terial) nonlinearity, in turn, takes into consideration the non-linear relations between stresses and strains. Thus the numerical analysis made it possible to account for two types of nonlinearity.
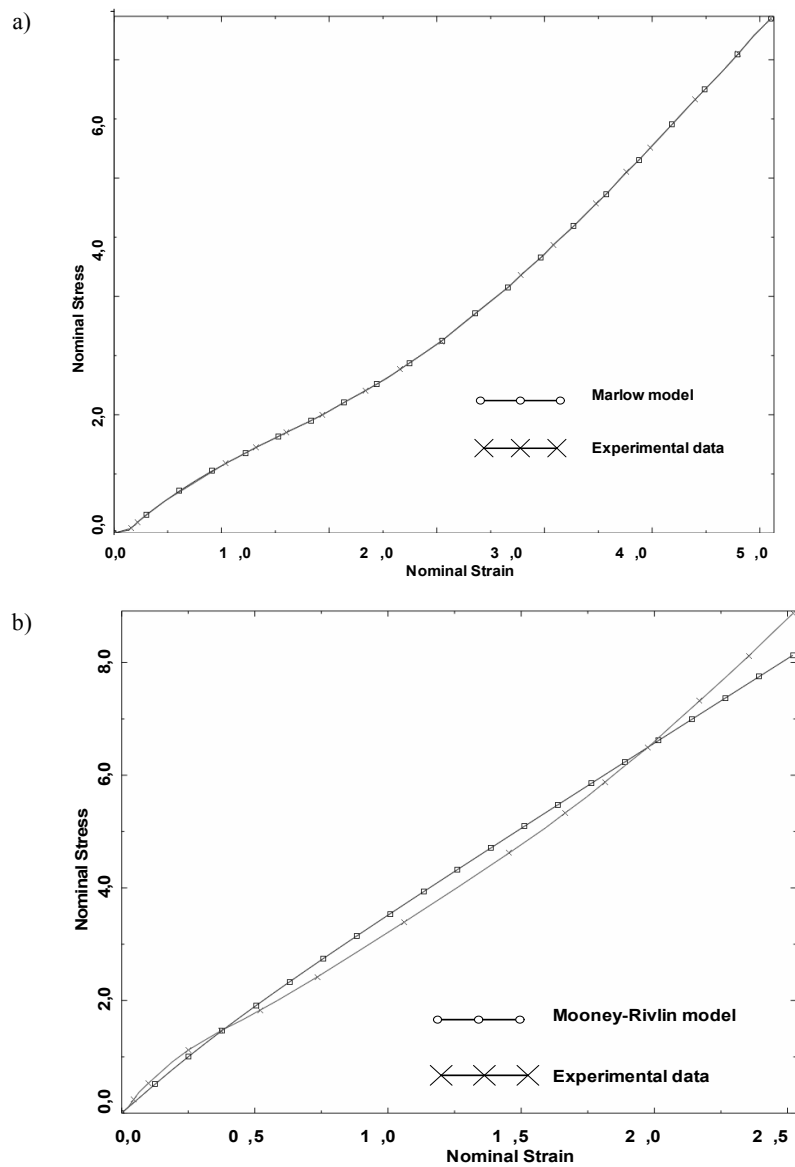

Fig. 6. A sample representation of the strength properties of internal rubber modeled with the use of (a) the Marlow model and (b) the Mooney–Rivlin model
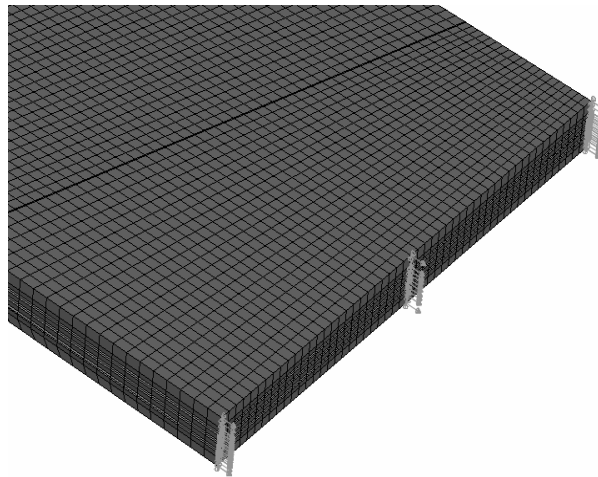
Fig. 7. A fragment of a spatial model of an adhesive-bonded joint: division into finite elements
and boundary conditions – application of load in the right part of the joint
(a view with the finite element mesh)

The numerical tool used for calculations was ABAQUS/Standard, a program that
enabled FEM analysis in the physically and geometrically nonlinear range. For FEM
calculations, a spatial numerical model of a single-lap adhesive bonded joint was used,
based on a hexagonal structural mesh of finite volumetric elements with three transla-
tional degrees of freedom per node. In the case of rubber, eight-node hybrid hexagonal
elements were used that allowed modelling of a hyperelastic material characterized by
large deformations and very small compressibility (or, indeed, incompressibility).

The boundary conditions were defined by suppressing the translational degrees of
freedom of nodes on the front left surface of the joint and by leaving the possibility for
the front right part of the joint to undergo displacements only in the direction of load
application (Figure 7). The load was applied by displacing the free end of the belt
along the x axis by 267 mm, i.e. 22 percent of the elongation of the entire conveyor
belt adhesive-bonded joint specimen, which corresponds to its mean elongation value
at critical load in experimental studies [6, 7, 15].

This manner of modelling is time-consuming and requires high computing power.
That is why an additional model was worked out based on the multi-layer structures
modelling technique (Figure 8) for the case of joining of sections of a multi-ply con-
veyor belt. This method is based on the Abaqus *layup* and *ply* options, which make it
possible to create a single-layer representation of a multi-layer structure by means of
shell elements (of the *shell*, *membrane* and *surface* type).

The advantage of such a method of modelling of multilayer structures is a signifi-
cant reduction in the size of the computing task due to modelling of the many layers of
a structure within one finite element (of the *shell* type, for instance). When a model is
worked out that well represents the actual conditions and has been appropriately veri-

fied, it becomes possible to carry out, in a short period of time, an analysis of a number of different models, for instance, ones with changed geometric parameters, in order to optimize the structure in terms of its geometry and strength.
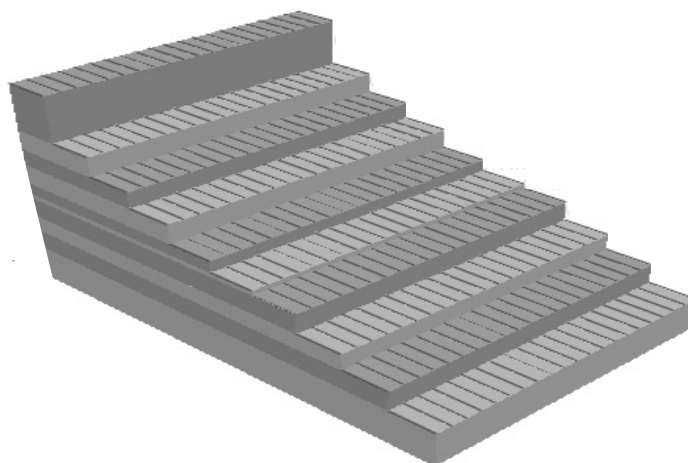

Fig. 8. A model of a joint based on the multi-layer structures modelling technique
– a fragment of the geometrical structure of the model

4. Conclusion

In the case of the adhesive joint connecting sections of a conveyor belt, there mainly occur shear loads and, in some rare cases, also peel loads. When the belt and the joint pass over pulleys and other elements of the load-bearing structure of the conveyor, there additionally occurs a momentary uneven shear load distribution as an effect of the action of forces that cause bending moments, which contributes to the increase of the tensile stress at the edges of the joint [36]. When designing an adhesive-bonded joint for connecting sections of a conveyor belt, this type of complications can be acted against by using techniques such as chamfering. A conveyor belt adhesive-bonded joint consists of four materials of different properties. Uneven deformation of these elements of the joint and their mutual displacement are the causes of development of deviatoric strains, including tangential stresses, which can lead to exceeding the value of breaking stresses and, as a consequence, destruction of the joint.

It is common knowledge that the strength of an adhesive-bonded joint depends on the thickness of the joint and that the value of the joint's breaking stresses is also a function of its thickness. A thicker joint better transfers shear stresses, as the stress is distributed in it over a larger area, thus reducing unit stresses in the adhesive, which results in a reduction of stress concentration. A similar situation takes place when an adhesive with a lower elasticity coefficient is used [36, 37]. Optimization of these two

parameters makes it possible to obtain a joint with the best strength characteristics. FEM analysis is extremely advantageous for the consideration of this problem since the results of experimental studies in this case diverge significantly from the results of analytical research. When selecting an adhesive and its parameters to suit a particular use, one should first consider the magnitude of the forces that will be acting on it and its ability to transfer maximum loads, as well as its resistance to fatigue or cyclic stresses, which is of particular importance in the case of conveyor belt joints. Cyclic stresses, particularly those of a prolonged nature, have a stronger negative effect on the durability of the joint than sustained stresses, even those of significant values. The fatigue strength of a joint, however, is most strongly influenced by the level of stresses in the joint, and in particular their uneven distribution and occurrence of stress concentration sites, which can be very precisely determined for any given case by analyzing the developed numerical model of a conveyor belt adhesive–bonded joint. An analysis of alternative joint structures or an optimization strength analysis carried out in this way enables fast and effective obtaining of exact results.

Acknowledgement

References

[1] Antoniak J.: *Urządzenia i systemy transportu podziemnego w kopalniach*, Katowice, Śląsk Publishers, 1990.
[2] Antoniak J.: *Przenośniki taśmowe w górnictwie podziemnym i odkrywkowym*, Gliwice, Wydawnictwo Politechniki Śląskiej, 2007.
[3] Antoniak J.: *Przenośniki taśmowe. Wprowadzenie do teorii i obliczenia*, Gliwice, Wydawnictwo Politechniki Śląskiej, 2004.
[4] Antoniak J.: *Urządzenia i systemy transportu podziemnego w kopalniach*, Katowice, Śląsk Publishers, 1976.
[5] Franasik K., Żur T.: *Mechanizacja podziemnych kopalń rud*, Katowice, Śląsk Publishers, 1983.
[6] Mazurkiewicz D.: *Monitoring the condition of adhesive-sealed belt conveyors in operation*, Eksploatacja i Niezawodność – Maintenance and Reliability, 2005, 3, pp. 41–49.
[7] Mazurkiewicz D.: *Computer system for monitoring conveyor belt joints*, Canadian Mining Journal 2007, 5, 23–24.
[8] *Taśmy przenośnikowe i inne produkty gumowe – poradnik*, Wolbrom: Fabryka Taśm Transporterowych Stomil Wolbrom S.A., 2008.
[9] www.mining-technology.com – The website for the mining, tunneling and quarrying technologies.
[10] Splicing instruction EP-conveyor Belts. Step-splice, cold. Metso Minerals 05/01 (not published).

[11] Błażej R.: *Wpływ właściwości mechanicznych rdzenia taśm przenośnikowych tkaninowo-gumowych na wytrzymałość ich połączeń*, Rozprawa doktorska, Wrocław, Politechnika Wrocławska, 2001.

[12] Błażej R., Hardygóra M., Komander H.: *Wpływ wybranych parametrów na trwałość zmęczeniową połączeń wieloprzekładkowych taśm przenośnikowych*, Transport Przemysłowy, 2002, 3, pp. 5–9.

[13] Hardygóra M., Błażej R., Komander H., Komander G., Konieczka Z., Stolarczyk R.: *Łączenie taśm przenośnikowych z linkami stalowymi metodą bezolejową*, Transport Przemysłowy, 2004, 4, 18, pp. 6–9.

[14] Madziarz M.: *Wpływ konstrukcji i technologii wykonywania połączeń tkaninowych, wieloprzekładkowych taśm przenośnikowych na ich wytrzymałość*, Wrocław, Politechnika Wrocławska, 1998.

[15] Mazurkiewicz D.: *Analysis of the ageing impact on the strength of the adhesive sealed joints of conveyor belts*, J. of Mat. Proc. Techn. 2008, 208, pp. 477–485.

[16] Szczygielska M., Mróz J., Broja A., Dyduch J., Augustowski W.: *Monitorowanie uszkodzeń taśm przenośnikowych w oparciu o zaimplantowane elementy detekcyjne*, Transport Przemysłowy, 2002, 3, 9, pp. 42–47.

[17] Godzimirski J.: *Wytrzymałość doraźna konstrukcyjnych połączeń klejowych*, Warszawa, WNT, 2002.

[18] Jabłoński R.: *Zmniejszenie naprężeń wzdłużnych jako jedna z możliwości zwiększenia trwałości taśm przenośnikowych*, Wrocław, Prace Naukowe Instytutu Górnictwa Politechniki Wrocławskiej, 1979.

[19] Jabłoński R., Kulinowski P.: *Zagadnienia doskonalenia konstrukcji przenośników taśmowych w pracach Katedry Maszyn Górniczych, Przeróbczych i Transportowych AGH*, Zakopane: Materiały XVI Międz. Sympozjum pt. *100 lat w służbie polskiego przemysłu wydobywczego*, FTT Stomil Wolbrom S.A., 2008, pp. 97–114.

[20] Niezgoda T.: *Analizy numeryczne wybranych zagadnień mechaniki*, Warszawa, WAT Publishers, 2007.

[21] Dębski H., Rudawska A.: *Analiza rozkładów naprężeń w jednozakładowym połączeniu klejowym*, [in:] *Analizy numeryczne wybranych zagadnień mechaniki*, ed. T. Niezgoda, Warszawa, WAT, 2007.

[22] Bąk R., Burczyński T.: *Wytrzymałość materiałów z elementami ujęcia komputerowego*, Warszawa, WNT, 2001.

[23] Altidis P., Warner B.: *Analyzing hyperelastic materials – some practical considerations*, Midwest ANSYS Users Group, Impact Engineering Solutions, 2004.

[24] Baldan A.: *Review: Adhesively-bonded joint in metallic alloys, polymers and composite materials*, Mechanical and environmental durability performance, J. of Mater. Sci. 2004, 39, pp. 4729–4797.

[25] Bilgili E.: *Modelling mechanical behaviour of continuously graded vulcanized rubbers*, Plastics, Rubbers and Composites, 2004, 4, pp. 163–169.

[26] Diani J., Brieu M., Gilarmini P.: *Observation and modelling of the anisotropic visco-hyperelastic behaviour of a rubberlike material*, Int. J. of Solids and Structures, 2006, 43, pp. 3044–3056.

[27] Martins P., Natal Jorge R. M., Ferreira A.: *A comparative study of several material models for prediction of hyperelastic properties: application to silicone-rubber and soft tissues*, Strain 2006, 42, pp. 135–147.

[28] Ruiz M., Gonzales L.: *Comparison of hyperelastic material models in the analysis of fabrics*, Intern. J. of Clothing Sc. and Techn., 2006, 5, pp. 314–325.

[29] Duncan B.C.: *Test methods for determining hyperelastic properties of flexible adhesives*, CMMT (MN) 054, Published by Crown, 1999.

[30] Gadala M.S.: *Unified numerical treatment of hyperelastic and rubber-like constitutive laws*, Communications in Applied Numerical Methods, 1991, 7, pp. 581–588.

[31] Kwon Y., Kwon H., Kim W., Leo S.: *Estimation of Rubber Material Property by Successive Zooming Genetic Algorithm*, J. of Solid Mech. and Mat. Eng. 2007, 6, pp. 815–826.

[32] Abaqus Analysis User's Manual, Dassault Systèmes, 2007.

[33] Ageorges C., Ye L.: *Fusion bonding of polymer composites. Series: Engineering materials and processes*, Springer Verlag, 2002.

[34] Pękala M., Radkowski S.: *Gumowe elementy sprężyste*, Warszawa, PWN, 1989.

[35] Darwish S.M.: *Analysis of weld-bonded dissimilar materials*, Int. J. of Adhesion and Adhesives 2004, 24, pp. 347–354.

[36] *Loctite – worldwide design handbook*, Munich: A Henkel Company, 1998.

[37] Godzimirski J., Kozakiewicz J., Łunarski J., Zielecki W.: *Konstrukcyjne połączenia klejowe elementów metalowych w budowie maszyn*, Rzeszów, Oficyna Wydawnicza Politechniki Rzeszowskiej, 1997.

Problemy symulacji numerycznej stanu naprężenia i odkształcenia w obszarze złącza klejonego taśmy przenośnikowej

Przenośniki taśmowe to powszechnie stosowane urządzenia transportu wewnątrzzakładowego, zbudowane z odcinków taśmy np. tkaninowo-gumowej, łączonych ze sobą w cięgno bez końca metodą klejenia. Połączenia taśm przenośnikowych narażone są na znaczne obciążenia dynamiczne w długim okresie czasu ich pracy. Mając na uwadze fakt, że zapewnienie wysokiej trwałości połączeń taśm przenośnikowych jest jednoznaczne z zagwarantowaniem ich niezawodnej eksploatacji, a wyniki dotychczas prowadzonych prac badawczych nie dają jednoznacznych rozwiązań szeregu problemów pojawiających się w tym przypadku, dlatego prowadzenie zaawansowanych prac w tym zakresie z wykorzystaniem technik informatycznych jest jak najbardziej wskazane. Szczególnie pomocna w poszukiwaniu nowych konstrukcji i optymalnych połączeń odcinków taśmy przenośnikowej jest analiza z wykorzystaniem metody elementów skończonych, co jednak wiąże się z szeregiem problemów, których okoliczności występowania oraz potencjalne rozwiązania opisuje niniejsza publikacja. Istotnym problemem w przypadku modelowania z wykorzystaniem MES jest na przykład odpowiednie zdefiniowanie modeli analizowanych materiałów. W przypadku połączenia klejowego taśmy przenośnikowej, składającego się z gumy oraz bazującego na gumie kleju kauczukowego z reguły w literaturze przyjmowany jest w tym przypadku do analizy model materiału hipersprężystego w oparciu o prawo Mooney–Rivlina, co odbywa się jednak na zasadzie dość arbitralnego wyboru, bez weryfikacji przy pomocy rzeczywistych danych pochodzących z badań wytrzymałościowych.

Guma to specyficzny materiał, zdolny do bardzo dużych odkształceń i z tej racji zaliczany do kategorii materiałów hipersprężystych, wymagających odpowiednich modeli konstytutywnych oraz wiarygodnego ich doboru w konkretnym przypadku. Odpowiednio dokładne zamodelowanie zachowania się materiałów gumowych nadal pozostaje kwestią otwartą. Dysponując

jednak danymi pochodzącymi z badań wytrzymałościowych, na drodze eksperymentalnej możliwe jest sprawdzenie, który z dostępnych modeli teoretycznych najlepiej odwzorowuje zachowanie się modelowanego materiału. W tym też celu oddzielnie dla każdego z materiałów składowych pochodzenia kauczukowego analizowanego złącza klejowego taśmy przenośnikowej przetestowano dostępne modele opracowane dla materiałów hipersprężystych. Oceniano przy tym ich stopień zgodności z danymi eksperymentalnymi za pomocą analizy zachowania się w danym przypadku materiału hipersprężystego w oparciu o tworzone krzywe reakcji przy wykorzystaniu wybranych potencjałów energii odkształcenia dla przypadku posiadanych danych testowych.

Analysis of adhesive properties of B2 hardmetal surface

Z. MIRSKI, T. PIWOWARCZYK

Wrocław University of Technology, Wybrzeże Wyspiańskiego 25, 50-370 Wrocław, Poland

Hardmetals belong to hardly wettable materials, so they should not be bonded without previous removing the surface layer left after sintering. The paper describes mechanical and chemical methods of preparing hardmetal surface for such processes as gluing and brazing. Particular attention is paid to the method of electrolytic etching that offers very good energetic properties of hardly wettable materials. In order to analyse the surface adhesive properties of hardmetals, measurements of roughness and wetting angle were performed, as well as electron microscopic examination and EDX analysis.

Keywords: *hardmetals, adhesion, surface preparation, roughness measurements, wetting measurements, EDX analysis*

1. Hardmetals used in the research

The hardmetal grade B2 (acc. to PN-H-89500:1988) were selected for the research, characterised by most advantageous abrasion resistance-to-ductility ratio, coarse-grained structure with uniformly distributed cobalt and absence of additional phases. Size of the WC grains (α phase) ranged basically from 1 to 7 μm, but also some grains up to 12 μm and single grains up to 15 μm happened. Examination of fracture surfaces did not reveal macroscopic pores or other material discontinuities. Microscopic investigations revealed minimum gaseous porosity (pores up to 10 μm) of the examined plates, which did not impair their quality.
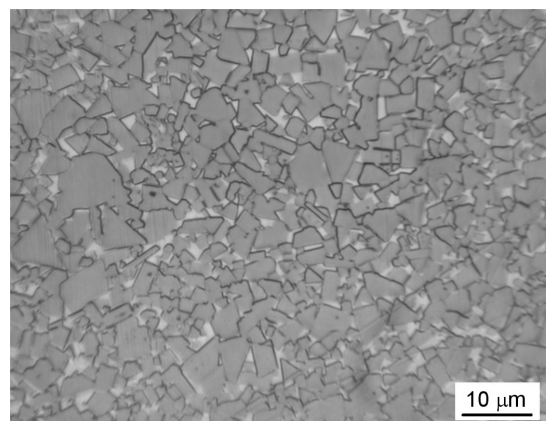

Fig. 1. Microstructure of hardmetals grade B2

Chemical analysis of the examined plates revealed cobalt content 9.3 wt.%. Chemical composition of the hardmetals is given in Table 1 and their physicochemical and mechanical properties are given in Table 2.

Table 1. Chemical composition of the examined hardmetals B2

Co	Ni	Ti	Ta	Nb	WC
9.3	0.006	max. 0.01	max. 0.01	max. 0.01	rem.

Table 2. Properties of the examined hardmetals B2

Density ρ, kg/m^3	$14.64 \cdot 10^3$
Hardness HV30	1220
Bending strength R_g, MPa	2300
Tungsten dissolved in Co, wt%	9.6

Microstructure of the B2 hardmetals is shown in Figure 1.

2. Methodology for preparing hardmetal surface

A very important factor affecting usable properties of a joint is proper preparation of the surfaces to be bonded, especially in the case of hardly wettable materials. This particularly concerns hardmetals, which after the sintering process should not be bonded without removing the surface layer. Their surface preparation often consists in applying metallic layers (in chemical/physical way or with plasma) [1−5]. Although the hardmetals are hardly workable by abrasive machining [6], in industrial practice they are usually subject to mechanical grinding. This is the reason why this method was chosen as one of the ways of hardmetal plate surface preparation.

Considering a possibility of significant surface development, abrasive blasting using alundum 99A with granulation 0.8 to 1.2 mm was selected as the next method of hardmetal surface preparation. This operation increases surface development. However, before this machining, the hardmetal preforms should be degreased to avoid introducing impurities into tiny pores and surface irregularities, as well as to prevent the abrasive agent from being soiled with grease. With respect to possible small quantities of oil in compressed air, the prepared surfaces were degreased once again after abrasive blasting [4]. This permitted removing dust and, at the same time, residues of the used abrasive. Roughness of the machined surface can be controlled by proper selection of grain size, angle and direction of the abrasive stream. To secure repeatability of the results, duration of the surface preparation by abrasive blasting was always 30 seconds and the distance of the blast nozzle directed perpendicularly to the specimen surface was 100 mm.

Chemical or electrochemical etching usually allows developing the surfaces of the materials to be bonded. A particular method of preparing hardmetal surface for bonding processes is electrolytic etching that consists in anodic dissolution of tungsten car-

bide grains in water solutions of alkaline metal hydroxides. The method is based on reduction of WC grains on the hardmetal preform surface to leave much more wettable β phase (Co-W-C). Cobalt does not reveal amphoteric properties, so it does not dissolve in bases. Figure 2 shows a model of hardmetal surface in raw condition (a) and after electrolytic etching (b). Electrolytic etching of the hardmetals results in obtaining developed, spongy cobalt layer 0.1 to 10 μm thick on the joint interface [3, 7].
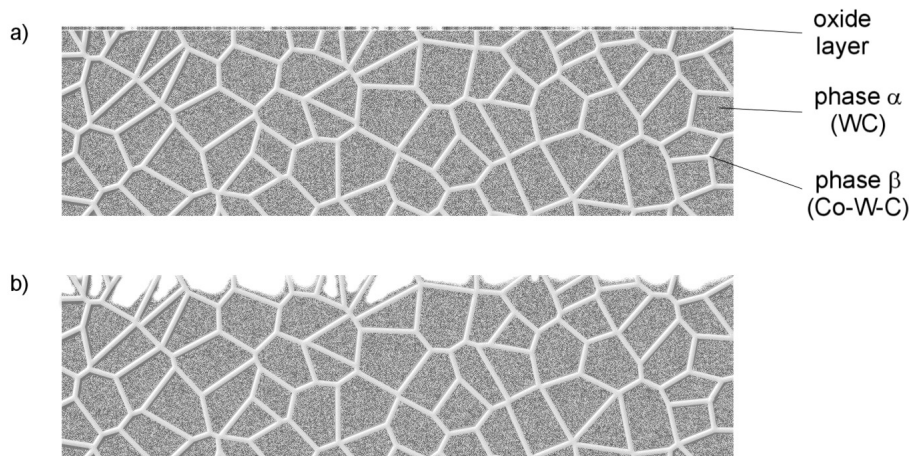

Fig. 2. Model of hardmetal surface: in raw condition (a) and after electrolytic etching (b)

From the point of view of bonding techniques (gluing, brazing), the especially favourable feature of this method is, beside significant surface development related to its stereometric features, isolating the metallic cobalt phase that enables easier wetting. It is expected that the mentioned factors, by increasing adhesive properties of surface layers, will also increase mechanical strength of glued joints.

Electrolytic etching of hardmetal surfaces was performed using an electropolisher Galvalab G7T made by SOJO with reversible magnetic stirrer. Its main parameters are: electrode voltage $U = 2$ to 12 V, electrode current $I = 0.1$ to 3.5 A, time range $t = 1$ to 20 min, max. etched area $S = 5$ cm^2. Layout of the testing stand for electrolytic etching is shown in Figure 3 [3, 7].

In the research, electrolytes were 4-mol solutions of NaOH and KOH. According to [3], the NaOH solution proved to be more active at dissolving tungsten carbides than the analogous KOH solution, so the first one was finally chosen as the electrolyte in the surface preparation processes.

Beside the type of electrolyte, intensity of dissolving WC grains is decided by basic parameters of electrolytic etching, namely electrode voltage U, etching time t and electrolyte temperature T. For each kind of the specimens, experimentally were determined the process parameters to obtain most advantageous properties for the intended application: $U = 3500$ mV and $t = 10$ min (temperature 30 °C). In the electrolytic

etching process, the electropolisher works as a so-called voltage stabiliser, so the current adjusting knob was always set to maximum.
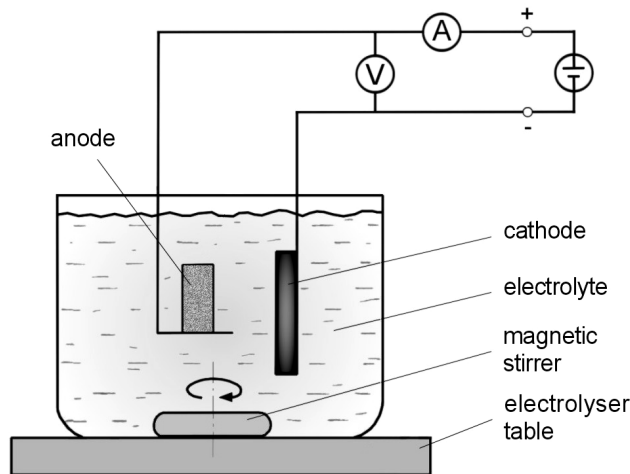

Fig. 3. Layout of testing stand for hardmetal electrolytic etching

After electrolytic etching, it was absolutely necessary to remove electrolyte residues and reaction products from the prepared surface layer. An effective method, practised by the authors, was cleaning the surface with Nitro solvent in an ultrasonic washer.

The third method of hardmetal surface preparation was a combination of electrolytic etching with subsequent abrasive blasting. Such a combination intensifies the adhesive interactions. In addition, it permits introducing new edges and gaps with maintained metallic surface structure.

3. Roughness measurements

Roughness measurements were made using a stationary profilometer Form Talysurf 120L made by Taylor Hobson, with a diamond tipped gauging point with apex angle 60° and roundness radius $r = 2$ μm. Pressure at the gauging point was 1 mN. Roughness measurements on the as-sintered surface were made on linear sections $l = 8.1$ mm long and on surface area $S = 9$ mm^2. Efficiency of the surface preparation methods was evaluated on the ground of three roughness parameters Ra, Rt and Rz. Five measurements were taken for each kind of surface preparation: mechanical grinding, electrolytic etching and combined electrolytic etching with abrasive blasting. For comparison, hardmetal in as-sintered condition were also analysed. Average values for the length $l = 8.1$ mm are shown in the diagram in Figure 4. Average values for the surface area $S = 9$ mm^2 are shown in the diagrams in Figure 5.
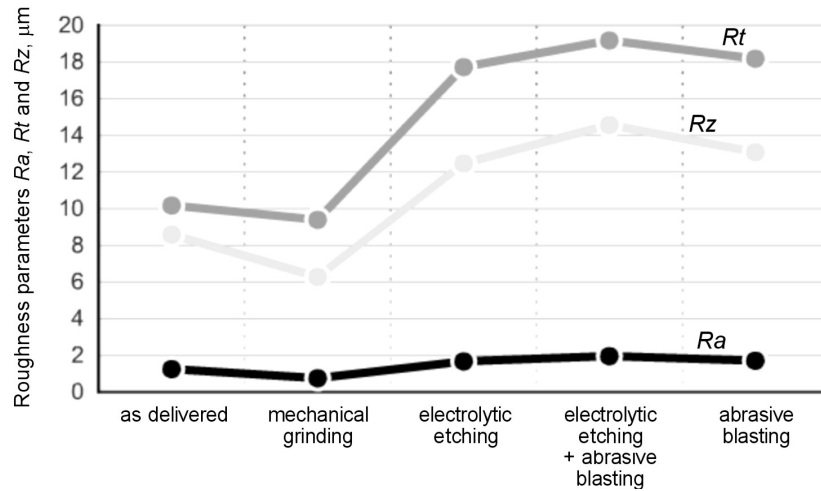
Fig. 4. Roughness parameters *Ra*, *Rt* and *Rz* for variously prepared
hardmetal surfaces on the length *l* = 8.1 mm
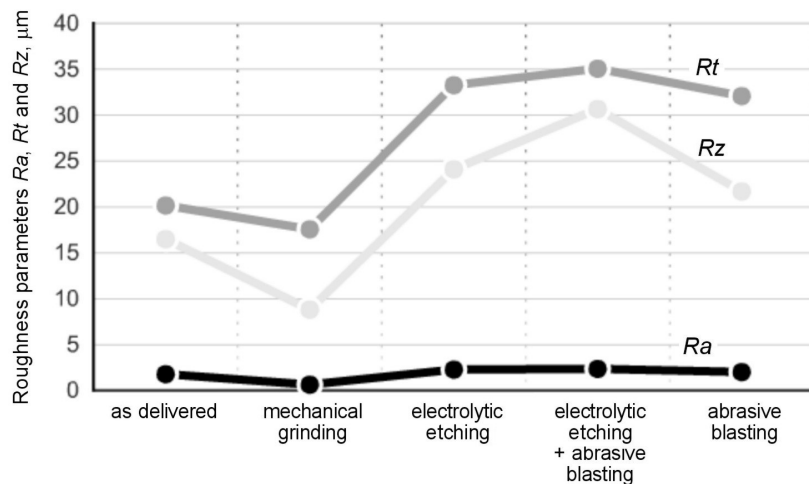
Fig. 5. Roughness parameters *Ra*, *Rt* and *Rz* for variously prepared
hardmetal surfaces on the surface area *S* = 9 mm^2

The roughness measurements prove that, from the point of view of surface development, the most efficient surface preparation method is electrolytic etching or its combination with abrasive blasting. Mechanical grinding, commonly used for surface preparation, is characterised by less developed stereometry than in the case of raw preforms. This is unfavourable e.g. in the case of gluing with mechanical adhesion. Thus, the gluing processes should employ more effective methods of surface layer preparation.

4. Wetting angle measurements

Analysis of adhesive properties of the surface layer requires considering energetic aspects. The standard EN 923:2008 determines wettability as ability of a liquid to spread on a solid surface. The physical phenomenon consists in the fact that a set liquid drop accepts equilibrium shape on the interface between solid and liquid phases or spreads along the solid surface [1, 3, 8]. In the first case, wettability degree can be determined on the ground of wettability angle that is an important quantity characterising interaction on the liquid-solid interface [8]. The wettability angle is included between the tangent to liquid surface at the contact point solid-liquid-air and the solid surface.

Beside the wetting angle, in surface analysis important are also thermodynamic quantities determined on its ground, like e.g. surface tension (specific free surface energy) or thermodynamic adhesion work. The calculation methods of surface layer energetic properties are based on the Young equation, formulated in 1805. The surface meeting assumptions of the Young equation maintains a set drop in equilibrium condition and even changes of its volume do not affect the wetting angle value [9].

According to the guidelines of proper wetting angle measurement, surfaces of the B2 hardmetals were made flat, horizontal, chemically homogeneous and neutral with respect to the wetting liquid [10]. As the wetting liquids, distilled water and methylene iodide recommended in this method were used first and next highly fluid anaerobic glue Loctite 638. With regard to strict relationship between wetting angle and local changes of surface tension and substrate topography, each time 5 drops of ca. 4×10^{-6} dm^3 were applied with a microsyringe or an automatic pipette. Then, the wetting angle θ was calculated using trigonometric relationships.

Wettability of hardmetal surface with selected liquids and anaerobic glue was determined on the station for wetting angle measurements, consisting of a Panasonic WV-CL 350 camera with a tripod, power supply with optical waveguides Flexilux 600 Longlife made by Scholly Fiberoptic GmbH, manipulator, measurement table and monitor, see Figure 6.
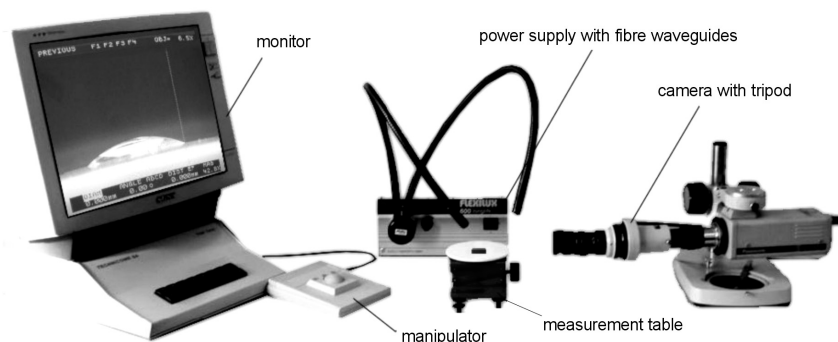

Fig. 6. Equipment for wetting angle measurements

Figure 7 shows average values of 5 wetting angle measurements for the preform surfaces wetted with distilled water ($\sigma = 72.8$ mN/m) and methylene iodide ($\sigma = 50.8$ mN/m), prepared by mechanical grinding, electrolytic etching, abrasive blasting and electrolytic etching combined with subsequent abrasive blasting. For comparison, the hardmetals in raw condition were also examined.
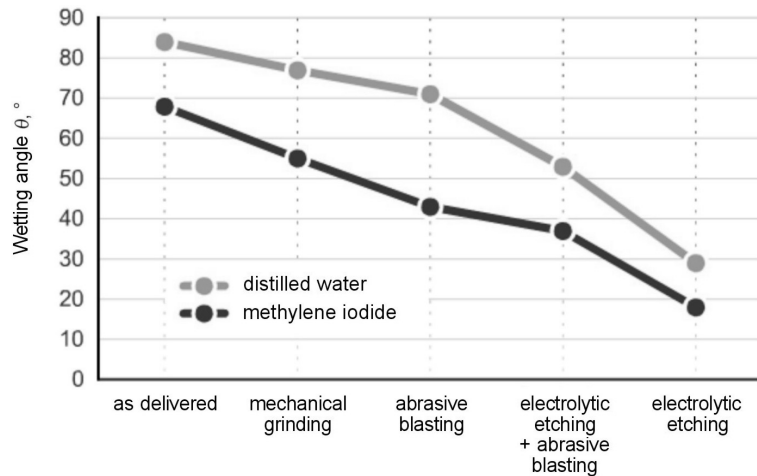

Fig. 7. Wetting angles θ for properly prepared hardmetal surfaces wetted with distilled water and methylene iodide

The measurement results prove that, from the wettability point of view, the most efficient surface preparation method is electrolytic etching. It permits introducing new edges and gaps together with developing metallic surface structure. This confirms the assumption indicating a relationship between the wetting angle and the surface roughness and homogeneity [10]. Differences in the drop size on the surfaces as delivered (a), mechanically ground (b) and electrolytic etched (c) are shown in Figure 8. Spread factor of distilled water on an electrolytic etched preform is almost 10 times higher than that for a raw preform (surface areas ratio 48.3 mm² to 5.2 mm²). Oval shape of a drop on the ground surface is related to grinding direction.

With respect to properties of Loctite 638, i.e. density $\rho = 1.09 \times 10^3$ kg/m³ and viscosity $\mu = 2500$ mPa·s, wetting angle was determined after the drop stabilised on the hardmetal surface, which happened in ca. 3 minutes after applying it. For standard liquids, forming an interface and establishing an equilibrium surface tension occurs within milliseconds [1, 8]. The presented wettability angle values for the hardmetal preforms wetted with anaerobic glue reveal a similar tendency as when wetted with distilled water and methylene iodide, see Figure 9. In this case, too, the best results were obtained for the electrolytic etched hardmetal surface ($U = 3500$ mV, $t = 10$ min).
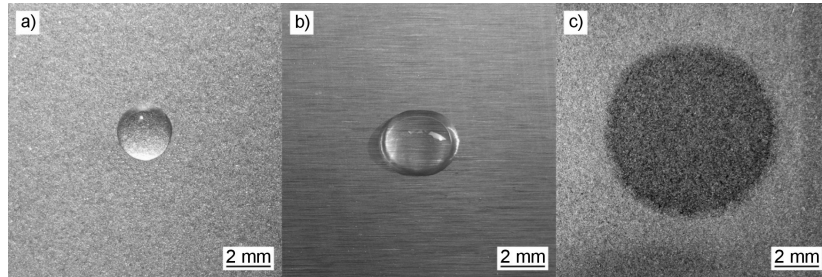
Fig. 8. Spread factor of distilled water on variously prepared hardmetal surfaces: as delivered (a), mechanically ground (b) and electrolytic etched (c)
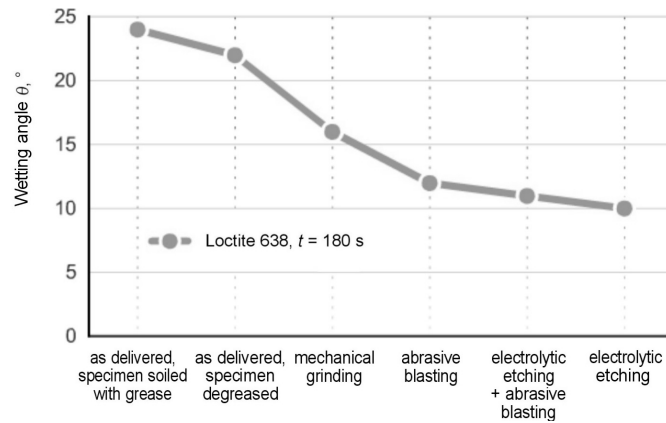
Fig. 9. Wetting angle for properly prepared hardmetal surfaces wetted with anaerobic glue Loctite 638
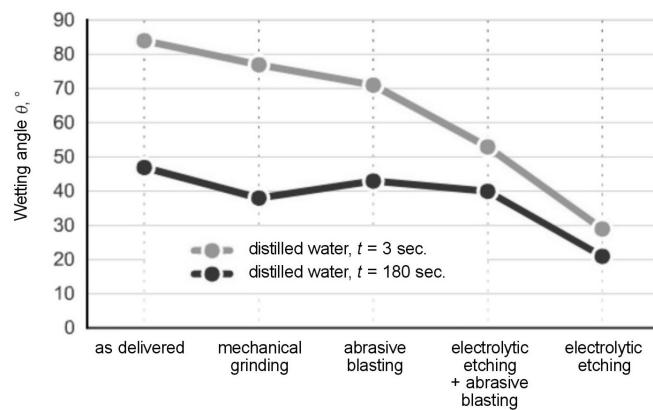
Fig. 10. Relationship between wetting angle and time for properly prepared hardmetal surfaces

Because of lower wetting angle values in comparison to those for distilled water and methylene iodide, additional measurements were taken to determine the relation-

ship between the wetting angle and time. The measurements made on the specimens wetted with distilled water after 3 minutes are shown in Figure 10. The results confirm favourable influence of time on the wetting angle. The visible almost 50% increase of wettability of mechanically ground specimens results from slight surface roughness and lack of spreading resistance along the grinding direction.

5. Surface analysis by electron microscopy

For variously prepared hardmetal preforms, observations were made using an analysing electron microscope and EDX analysis (energy dispersive X-ray analysis). Figures 11 to 13 show hardmetal surfaces in raw condition, after mechanical grinding and after electrolytic etching, together with respective characteristic radiation spectra. Analyses of cobalt phase were made on the area 50×60 μm. The measurement results indicate explicitly that electrolytic etching dissolves tungsten carbide grains in the surface layer, uncovering the metallic phase. This phase is the cobalt-based phase with small quantity of carbon and tungsten (9.6 wt%) dissolved during the sintering process [3]. For the examined B2 hardmetal after etching, almost 3 times higher cobalt concentration (26.5 wt% Co) was found in comparison with the preforms in raw condition (9.3 wt% Co) or after mechanical grinding (9.6 wt% Co). This is particularly favourable from the point of view of some bonding techniques (gluing, brazing), for which increased interaction of metallic phase is required.

In addition, EDX analysis was performed for the hardmetal surface after electrolytic etching in order to determine tungsten and cobalt concentration. Figure 14 shows a tungsten carbide grain, whose analysis revealed 96.3 wt% *W* and 3.7 wt% Co. The X-ray microprobe did not allow quantitative carbon analysis. At the point marked in Figure 15, the cobalt-based bonding phase contained 70.4 wt% Co and 29.6 wt% W. The so high tungsten concentration results from the electron beam penetration depth (1 to 3 μm) and small thickness of the β layer itself (Co-W-C).
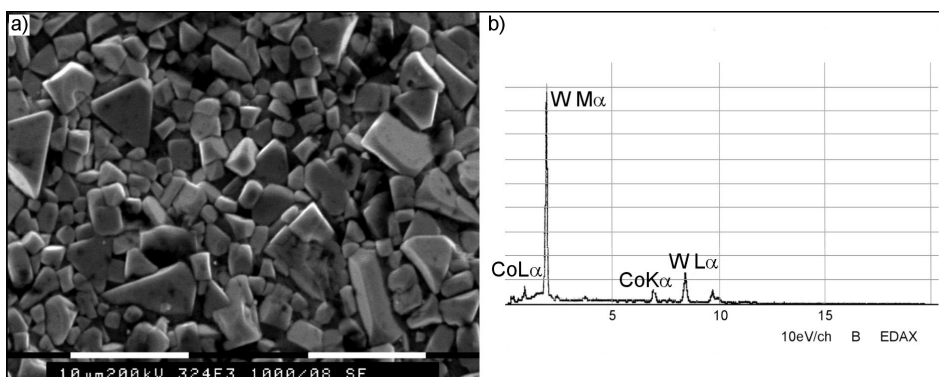
Fig. 11. Hardmetal surface in raw condition (a) and characteristic radiation spectrum (b), chemical composition: 9.3 wt% Co, rem. *W*
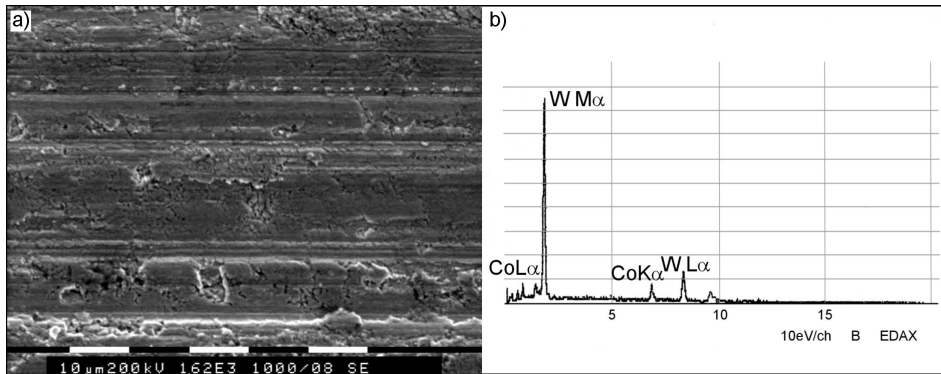
Fig. 12. Hardmetal surface after mechanical grinding (a) and characteristic radiation spectrum (b),
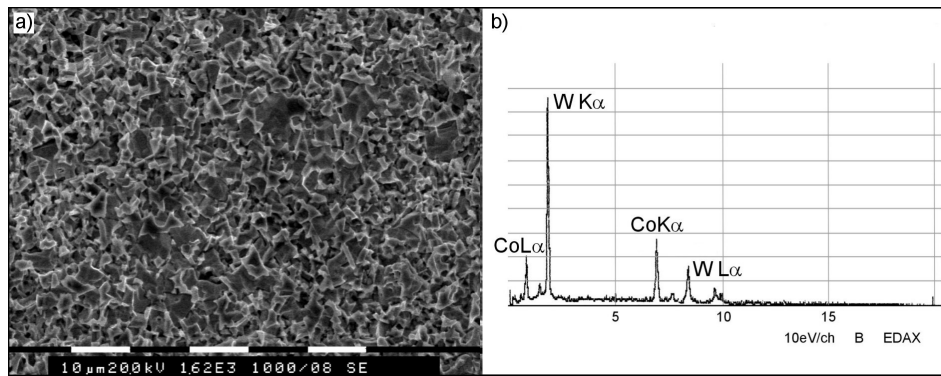chemical composition: 9.6 wt% Co, rem. *W*

Fig. 13. Hardmetal surface after electrolytic etching (*U* = 3500 V, *t* = 10 min) (a)
and characteristic radiation spectrum (b), chemical composition: 26.5 wt% Co, rem. *W*
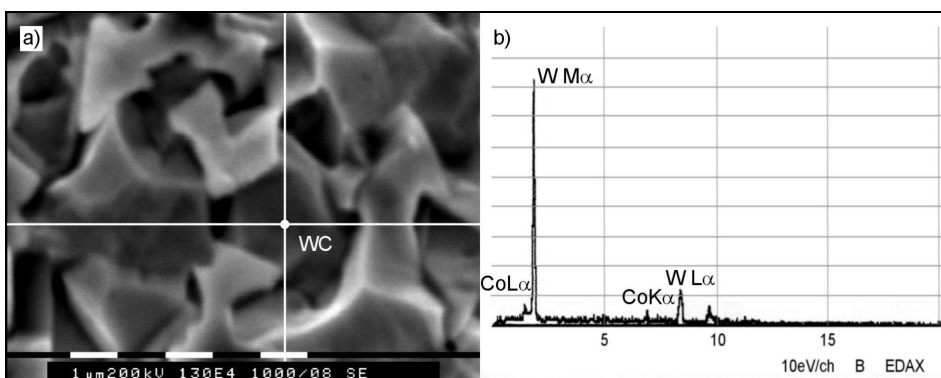

Fig. 14. Hardmetal surface after electrolytic etching with marked WC grain (a)
and characteristic radiation spectrum (b)
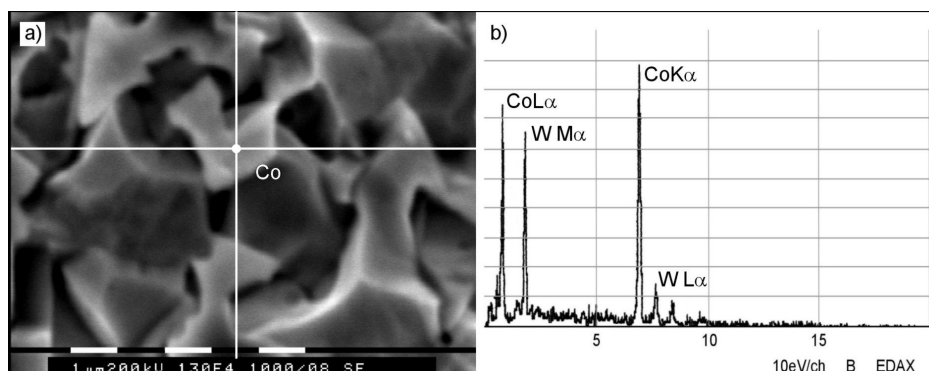
Fig. 15. Hardmetal surface after electrolytic etching with marked cobalt phase Co-W-C (a)
and characteristic radiation spectrum (b)

6. Conclusions

• Selection of a material surface preparation method is decisive for its adhesive properties, thus influencing strength and quality of joints of hardmetals with steel.

• The developed method of electrolytic etching of hardmetals with the parameters $U = 3500$ mV and $t = 10$ min or its combination with subsequent abrasive blasting leads to higher surface development in comparison with other traditional methods, like mechanical grinding.

• The hardmetal surface preparation method giving best results from the wettability point of view is selective electrolytic etching, for that the wetting angle values are the lowest and the spread factor is the highest.

• The method of electrolytic etching of hardmetals using the parameters $U = 3500$ mV and $t = 10$ min leads to the largest surface development in comparison with the other traditional methods (e.g. mechanical grinding). On the soldered surface, concentration of the cobalt-based metallic phase increased 3 times (till 27 wt% for the preforms with initial composition 9.5 wt% Co and the rest WC), what is favourable with respect to various bonding techniques (gluing, brazing).

References

[1] Piwowarczyk T.: *Zwiększanie oddziaływań adhezyjnych i kohezyjnych w połączeniach klejowych węglików spiekanych ze stalą C45* (*Increase of adhesive and cohesive interaction in adhesive joints of hardmetals with steel C45*) (in Polish), PhD Thesis, Institute of Production Engineering and Automation, Wrocław University of Technology, 2008.

[2] ASM International Handbook Committee: *ASM Metals Handbook*, Vol. 5, *Surface Engineering*, 9th Edition, American Society for Metals, USA, 1994.

[3] Mirski Z.: *Sterowanie szerokością szczeliny lutowniczej w procesach spajania materiałów różnoimiennych* (*Control of the width of brazed joint clearance in the processes of joining dissimilar materials*) (in Polish), The scientific works of Institute of Production Engineering and Automation of Wroclaw University of Technology, Series: Monograph No. 22; Wrocław University of Technology Publ., Wrocław, 2000.

[4] Pilarczyk J.: *Poradnik Inżyniera − Spawalnictwo* (*Engineer's guide – Welding*) 2 (in Polish), WNT Publ., Warsaw, 2005.

[5] Mirski Z., Granat K., Prasałek A.: *Properties of lead-free tin solders for metal and mechanic sector*, Archives of metallurgy and materials, 4, 2008, pp. 1035−1046.

[6] Cichosz P.: *Narzędzia skrawające* (*Cutting tools*), WNT Publ., Warsaw, 2006, (in Polish).

[7] Mirski Z., Szymkowski J., Piwowarczyk T.: *Klejenie i lutowanie twarde węglików spiekanych trawionych elektrolitycznie* (*Gluing and brazing of electrolytic etched hardmetals*) (in Polish), Przegląd Spawalnictwa, 9−10, 2006, pp. 64−68.

[8] Topolnicka T.: *Zwilżalność i napięcie powierzchniowe jako kryteria oceny lepiszczy i syciw pakowych*, (*Wettability and surface tension as evaluation criteria of pitch binders and impregnants*) (in Polish), PhD Thesis, Institute of Chemical Coal Processing in Zabrze and Wroclaw University of Technology, Wrocław – Zabrze, 2006.

[9] Żenkiewicz M.: *Adhezja i modyfikowanie warstwy wierzchniej tworzyw wielkocząsteczkowych* (*Adhesion and modification of surface layer of high-molecular plastics*) (in Polish), WNT Publ., Warsaw, 2000.

[10] Sobczak N., Singh M., Asthana R.: *High-temperature wettability measurements in metal/ceramic systems – Some methodological issues*, Current Opinion in Solid State and Materials Science, 9, 2005, pp. 241–253.

Analiza właściwości adhezyjnych powierzchni węglików spiekanych gat. B2

Węgliki spiekane należą do materiałów trudno zwilżalnych, zatem nie powinny być spajane bez usunięcia warstwy powierzchniowej po spiekaniu. W pracy omówiono mechaniczne i chemiczne metody przygotowania powierzchni węglików spiekanych do takich procesów, jak klejenie i lutowanie twarde. Szczególną uwagę poświecono metodzie trawienia elektrolitycznego, oferującej bardzo dobre właściwości energetyczne powierzchni materiałom trudno zwilżalnym. W celu analizy właściwości adhezyjnych powierzchni węglików spiekanych wykonano pomiary chropowatości, pomiary kąta zwilżania, badania z wykorzystaniem mikroskopii elektronowej i analizy pierwiastków metodą EDX.

Process monitoring and closed loop controlled process

R. NEUGEBAUER, H. BRÄUNLICH, S. SCHEFFLER

Fraunhofer Institute for Machine Tools and Forming Technology (IWU), Reichenhainer Str. 88, 09126 Chemnitz, Germany

There are a number of variables which can seriously affect the sheet metal forming process. By determining the process fluctuations, it will ultimately be possible to improve the production process. To do this, monitored or closed loop controlled processes potentially constitute an important tool for the reduction of defects, reduction of rework and a better quality of final products.

The Fraunhofer Institute for Machine Tools and Forming Technology (IWU) in Chemnitz investigated typical process variables such as flange movement as the basis for control systems. Different kinds of non-contact sensors were successfully tested. A multi-point cushion or tool integrated piezo-elements in conjunction with torsion-elastic tools were used as reacting systems.

One application used process monitoring with one or more sensors to support quality control, or the same system with an add-on for early error recognition and automatic recommendation of corrective measures. Finally, fully controlled loop systems based on intelligent algorithms were developed.

Keywords: *process monitoring, closed loop control, in-process, deep drawing, sheet metal forming, sensor, laser, piezo-actuator*

1. Introduction

With the increase in complexity of customer-specific component geometries in production and the simultaneous improvement in the properties of the finished components, the tasks facing the metal processing industry are ever more challenging, bordering on the impossible. For this reason, technologies and processes which exploit the potential of manufacturing options more effectively than was previously the case, which open up broader fields of application and reduce costs, are of crucial importance. In this connection, process monitoring and process control are of particular importance, since they firstly enable more prompt recognition and correction of faults and secondly facilitate seamless quality control.

The use of high-strength materials such as aluminium and the simultaneous increase in the complexity of components for reasons relating to design and functionality intensify the problems even further. The requirement for reproducibility must be regarded as a further, very important criterion for mass production [1–5].

When combined, the points listed above, which characterise almost all production operations at the present time, result in the following general specification criteria:
- work at the limits of the forming capability of the materials,
- work in a very narrow process window.

The resulting links are shown in Figure 1. What stands out, compared with processes in use to date is the narrower field of tolerance within which manufacturing must now take place.
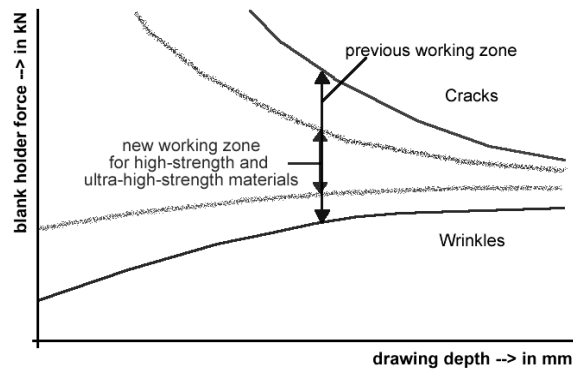
Fig. 1. Working zone during deep drawing

Production which is reproducible and free from defects thus becomes increasingly more difficult as the working zone becomes smaller. There are two options for countering this:

• The boundaries of the process window must be widened. This is facilitated, for example, by the use of multi-point drawing technology in conjunction with blank holders with flexural elasticity or by means of a drawing process with superimposed vibration.

• Manufacturing must remain constantly at the centre of the available working area. This variant requires process monitoring or process control in order to be able to intervene in the event of any deviation in the parameters.

As most presses in industrial use are in plants where the aforementioned multi-point drawing technology is not available, attention is focused mostly on the second alternative. The following conditions must be met for maximum effectiveness:

• a process variable which can be detected and which characterises the changing process with an adequate degree of precision,

• appropriate sensors to monitor this process variable (wherever possible in-process),

• analytical software which processes these data and generates a response (correction factor) as output,

• an option to implement the correction in the plant, which can be carried out manually in the context of a process monitoring capability.

2. Factors affecting the forming

In addition to pre-process and post-process factors, it is of course the forming process itself which has the greatest influence.

The results of the drawing process, which is the process that is most representative of forming technology, are essentially determined by

• the sheet metal material in the form of a blank, together with its properties and dimensions,

• the forming tool with its active components, i.e. the punch, matrix and blank holder,

• the press, in particular the drawing device,

• the tribological system influenced by the three parameters above, which is responsible for the flow of materials.

The sheet metal material itself is subject to fluctuations due to changes in the coil or variations from batch to batch, for example in terms of the thickness of the sheet metal, the mechanical and technical specifications and the structure.

During production, the reciprocal effects of these fluctuations result in components with varying properties (in particular with respect to dimensional stability), or even lead to production of defective components.
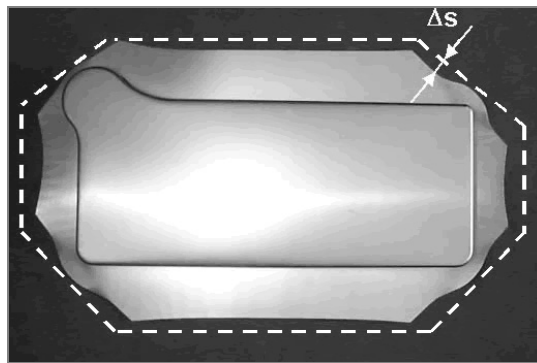
Fig. 2. Drawing in of the sheet metal during deep drawing

Ultimately, however, all of the above influential variables manifest themselves in a change in the characteristics of the drawing in of the sheet metal (Figure 2) during deep drawing. This process variable can therefore be regarded as reflecting the quality of the production process for an individual component or for entire series. In-line detection of this variable therefore provides an opportunity to apply process monitoring or process control to deep drawing operations.

3. Sensors

3.1. Sensor technology currently available

The most important properties of the sensors to be used to detect the drawing in of the flange are the degree of accuracy required and the speed of the signals.

Thanks to modern processor technology, these conditions are now met by almost all types of sensor on the market. In initial pre-testing carried out at the IWU since 1998, sensors of varying design for detecting flange indentation have been investigated.

These included:

• Inductive path sensors, which make contact with the edge of the sheet metal by means of a tongue with a spring,

• fibre-optic measuring probes, which are mounted so they pass through the tool in the hold-down area and which detect the drawing in by means of the grain of the sheet metal,

• linear array cameras, which after forming record the edge of the sheet metal all round the workpiece,

• laser triangulation sensors (Figure 3), which detect the drawing in of the flange without making contact.
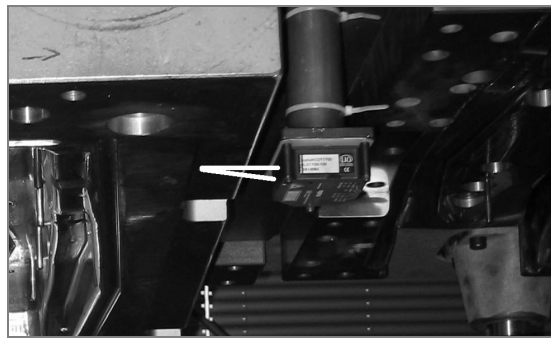
Fig. 3. Laser triangulation sensor

For obvious reasons (in-line, non-contact, no penetration of the tool) the laser sensor, which was mounted on the tool as an add-on, proved the most suitable for process monitoring. The scanning frequency achievable using this system (up to 10 kHz) and the extremely high degree of accuracy (resolution < 0.08% of the measurement range) are further advantages of this type of sensor. Characteristic sheet metal drawing-in sequences are illustrated in Figure 4, taking a monitored drawing stage (B pillar) as an example.

Fears that vibrations in the operating mechanism of the press could lead to erroneous signals or even to failure of the sensor have so far failed to materialise in several industrial applications. Similarly, it has been possible to disprove the theory that the use of this type of sensor is limited to flat tools only, since the very small light scatter of the laser (< 0.2 mm) means that the drawing in of the sheet metal can be detected without any problems, even in moderately curved tools. Neither does normal contamination present any problem: for forming stages involving over-average use of drawing oil, a compressed air nozzle can be connected up to clean the measuring channel.
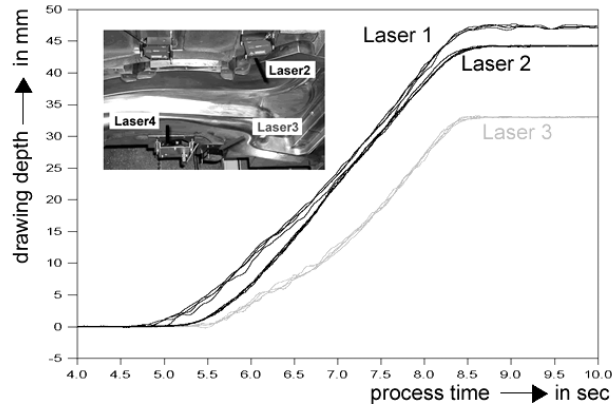
Fig. 4. Drawing in of a flange during a drawing operation

In an SFB project, a sensor variant based on a ball bearing sensor (similar to a computer mouse) is currently being tested. This involves detection of the movement of the inflowing material by means of mechanical contact with the material. In this system too, however, the surface of the tool ultimately has to be penetrated in order for the sensor to make direct contact, which makes this type of sensor unsuitable.

3.2. Future sensor technology

Although the laser sensor has worked without any errors in all the instances in which it has been used in practical application to date, the fact that it is mounted externally on the tool constitutes a possible source of errors (damage, collision during the process, contamination).

For this reason, the IWU is currently pursuing the idea of non-contact sensors integrated in the tool, of which there are two main types. These are described in greater detail below.
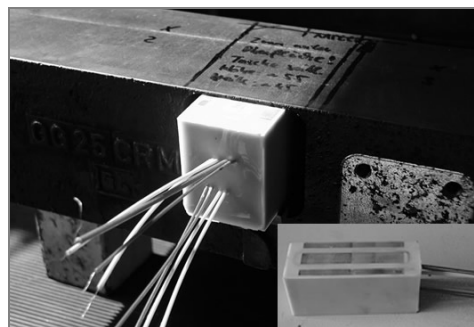
Fig. 5. Sensor based on the eddy-current principle in the tool

Coil sensors. Non-contact coil sensors are based on the eddy-current principle, where the sensor is built in beneath the surface of the tool (Figure 5) and detects the moving edge of the sheet metal through the tool surface. In contrast with [9], there is no break in the surface of the tool, and in addition only one coil is used (in the blank holder or the matrix).

The advantages of this coil technology are above all its robustness and the low costs. Depending on the nature of the measuring principle, detection is possible with both steel and aluminium blanks. In the testing tool, tolerances for sheet metal edge detection were under +/–0.5 mm deviation in the closed tool (Figure 6, reference system: laser sensor), penetrating a tool thickness of at least 4 mm.
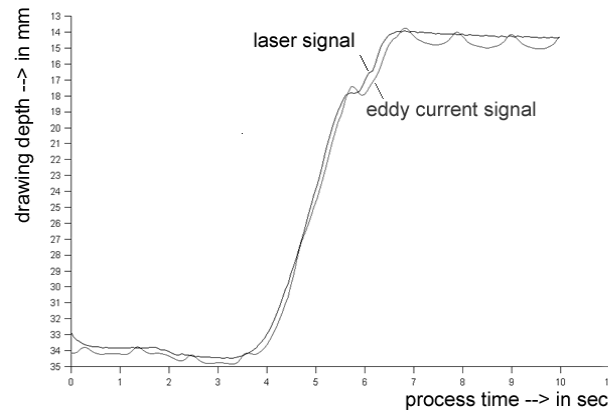
Fig. 6. Drawing in detected by eddy-current principle

Sensor fields based on piezo elements. In this type of sensor system [9], pressure-sensitive sensor fields comprising piezo elements (Figure 8) are used. These are mounted on the surface of the tool beneath a protective layer to prevent wear and tear (Figure 7).
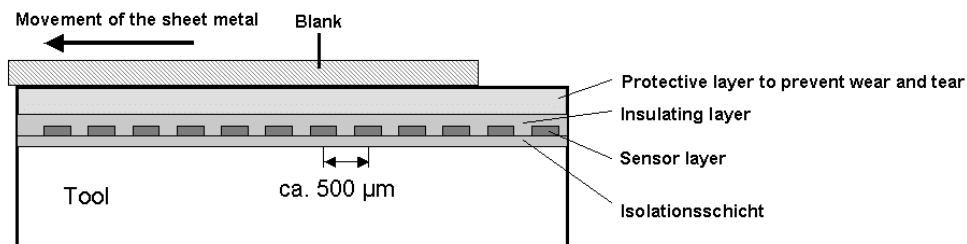
Fig. 7. Layered construction

This enables global monitoring of the component, and the structure of the sensor layer means that the tool can be embedded. By means of a pressure/no pressure report and the logical interconnection of the individual sensors, it is possible to determine the position of the sheet metal in the tool as a whole at any point in time.
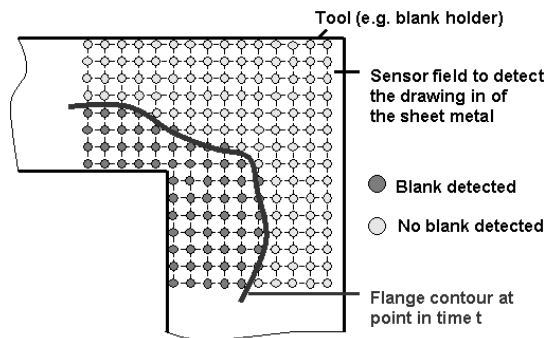
Fig. 8. Sensor fields based on piezo elements

4. Actuators

In order to be able to intervene in the drawing process to make corrections, a control variable is required that can exert a direct influence on the process parameter monitored (drawing in of the flange). Of necessity, the choice in this case is the blank holder force.

Changing the blank holder force has a direct effect on the surface pressure in the area of the flange, which results in a change in characteristics of the drawing in of the sheet metal.

By making comparisons with stored master and limit values, it is possible to change the blank holder force during the drawing operation (process control) or between two strokes of the press (process monitoring) in order to guarantee a component which lies within specified tolerance limits.

We present below various techniques for actively exerting an influence on the drawing process.

4.1. Change in overall blank holder force

For production using a conventional tool assembly this is the usual option chosen to correct the quality of the component during the drawing stage.

In this approach, increasing or decreasing the blank holder force affects the entire component, although in most cases only a small area of the component proves to be critical for forming. Where there is a rigid tool construction and a plant with a single or four-point cushion, there is practically no other option available.

4.2. Change in local blank holder force

As mentioned above, for almost all components the problems encountered when forming are confined to localised areas. It would therefore appear logical to restrict the effect of changing the blank holder force to these particular areas, leaving the non-critical remainder of the component subject to constant production conditions.

There are once again two pre-requisites for achieving this:
- the opportunity to change the blank holder force locally,
- a tool designed in such a way as to relay these changes locally.

These variants are described in greater detail below.

Torsion-elastic tools. Conventional tools (blank holders) are constructed with a high degree of flexural strength (Figure 9a), i.e. it is assumed that the best possible production conditions in terms of the tools (wear pattern) have been created as a result of the TryOut, requiring only minor corrections at a later stage. Safety issues and the absence of innovative tool design concepts also play a decisive part in this.

At the Fraunhofer IWU, we have for some time been pursuing the use of blank holders with flexural strength (Figure 9b) which make it possible to influence surface pressure locally. In [5–7], in addition to the structural principles of these tool components, the effects which can be achieved as a result are demonstrated. These are manifested mainly in a shift in the process limit "cracks", leading to a more stable manufacturing process.
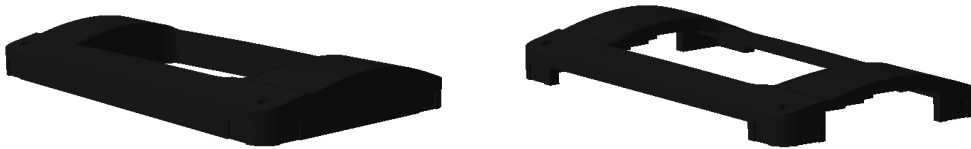
Fig. 9. Blank holders a) rigid and b) torsion-elastic (universal)

Local application of force – multi-point cushions. If a torsion-elastic tool design is available, the passive mode of operation already has positive effects on process stability [8]. In order to achieve optimum results, however, the opportunity to apply local force should be seized.

In this respect, the multi-point cushions of modern presses emerge as the best possible variant (Figure 10) in terms of exerting strategic influence on the process at any point in time. This cushion design can also be retrofitted.

The combination of multi-point drawing technology and torsion-elastic blank holders results in a significant widening of the process window and hence to a more stable production process, as can be seen in Figure 9. An incidental effect is the distinct increase (of up to 45%) in the possible drawing depth for the same blank. This is accounted for by the optimised and more even distribution of surface pressure.

Fig. 10. Multi-point cushion (16 axes)
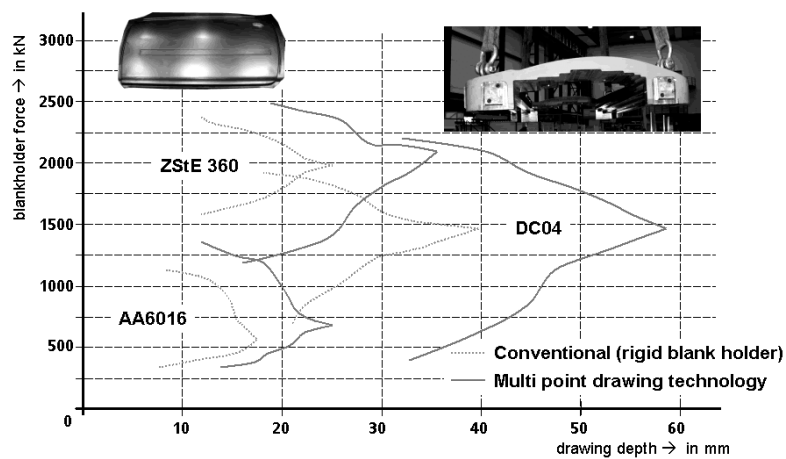
Fig. 11. Working areas

Local application of force – piezo actuators. Because, as has already been mentioned, most components typically have only one or two critical areas, an additional option exists for the local application of force: integral piezo elements integrated within the tool.

This variant attracts particular attention when no multi-point cushion is available in the plant. In this case, the blank holder force is applied universally over the tool, as has hitherto been normal practice. At the critical points, removable piezo actuator systems built into the tool then relay the differentiated application of force into the blank holder area.

Fig. 12. Piezo actuator built into the tool (B pillar)

Figure 12 shows such a system built into the blank holder of a B-pillar. The local-ised thinning of the surface of the tool above the actuator can also be seen. The fact that it is usually possible to retrofit and replace the piezo actuators in existing tools has proven to be advantageous.

5. Process monitoring systems

The aim of creating the process monitoring system was to make it possible to work within specific tolerances relevant to the particular component. These tolerances are characterised by an upper value for drawing in of the flange (wrinkle limit) and a lower value for drawing in of the flange (crack limit). Both values can be provided in ad-vance by the finite element method, for instance, but it is also possible to use meas-urements taken from the press for this purpose.

Only one value, the overall drawing in of the flange, is detected and analysed in this process. By analysing the trends and comparing them with the previous manufac-turing procedure, the probability of divergence from the "good component zone" is then evaluated. A signal is then generated, warning of the risk of defective parts being produced.

The procedure for process monitoring of a drawing stage is described in detail below.

5.1. Data recording

Integration of the laser triangulation system in the drawing tool provided an op-portunity to analyse the main forming phase. In Figure 13, this is illustrated using the example of a side rail, showing a sensor mounted in the plane of joint in the bottom die.
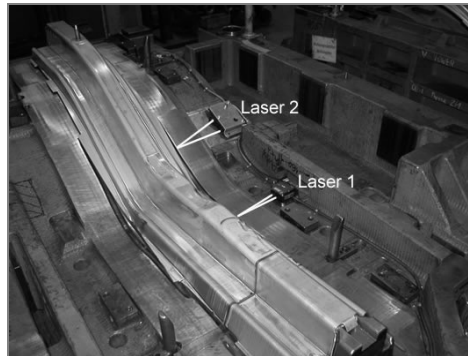
Fig. 13. Sensors in the tool (frame side rail)
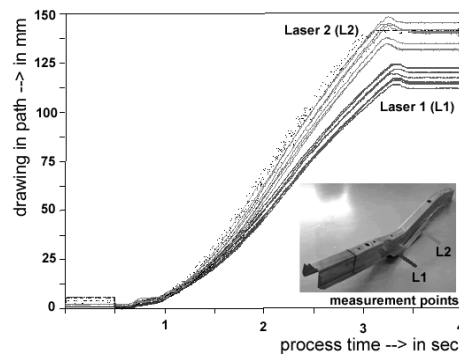
Fig. 14. Tolerance range of drawing in of flange

This made it possible to record the drawing in path for each component. After comparing all the data, it was established that process conditions fluctuate enormously within a run of only 120 consecutive components. This is manifested in overall drawing-in paths which deviate from one another by up to 3 mm (Figure 14) and in the consequent variation in properties of the finished component. This is primarily due to the fluctuations in material specifications of the various batches.

5.2. Data preparation

In contrast with the process control described in point 6, in process monitoring it is only necessary to take steps to intervene when there is a high probability that components classified as defective will be produced. This is accomplished by analysing the trend in the production process as described. In other words, the drawing path is ascertained by applying analytical measures to the drawing in characteristics (measured value at the end of drawing in – measured value at the start of drawing in). No trigger signal from the press is required, so the process monitoring functions as an independent system without intervention in the plant.
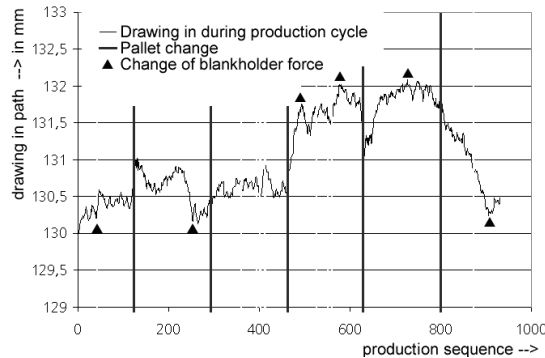
Fig. 15. Production sequence (drawing in process)

Figure 15 shows a typical production sequence based on this principle.

Despite being sourced from the same supplier, the manufacturing process causes material specifications to vary from coil to coil (and within the same coil), which is particularly apparent during the marked pallet changes as a discontinuity in the drawing in behaviour. If the resulting components deviate too far from the specific criteria to be met, corrective action is taken by intervening in the process. This is accomplished by changing the blank holder force in the drawing stage.

5.3. Principle of process monitoring

When evaluating the production procedure shown in Figure 13, it was established that measures were taken by means of the press operator to keep the drawing in of the flange within a specified range (without his being aware of this!)

The necessary correction was only made in the event of an error repeatedly being identified during quality control of the finished component. In the entire press line (taking this component as an example) there are at least 15 additional components which might already exhibit the same defect. In the case illustrated, 77 of the 622 components inspected were classed as defective, 32 of them classed as scrap.

By means of software analysis of the manufacturing process, it was possible to eliminate components thus classified almost completely. In other words, by observing the recorded error conditions, it would have been possible to initiate the subsequent response at a considerably earlier stage, resulting in the production of fewer defective parts.

The approach taken was as follows:

A normal production process is characterised by smaller fluctuations, i.e. the drawing in path of consecutive components fluctuates constantly around a fictitious mean value. In contrast, any defective components tend to be characterised by a shorter or longer drawing in process. These tendencies are detected by the monitoring program and are flagged in Figure 16. By making the necessary adjustments in the software,

minor and normal fluctuations ("short" tendencies) are ignored, with the result that only the real process deviations are taken into account.
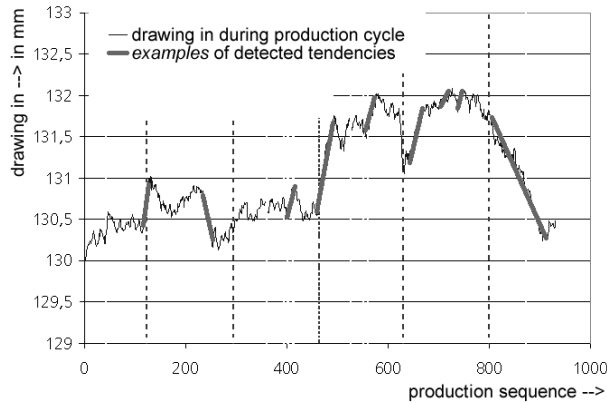
Fig. 16. Analysis of tendencies

If such a trend moves in the direction of the previously specified limits or exceeds these limits, then an error signal is generated. In addition, a counter-measure can be proposed which is calculated on the basis of the determined values. In the present case, an intervention in the production process is made for control purposes by changing the blank holder force, where the correction signal is a positive or negative delta of this process variable (Figure 17).
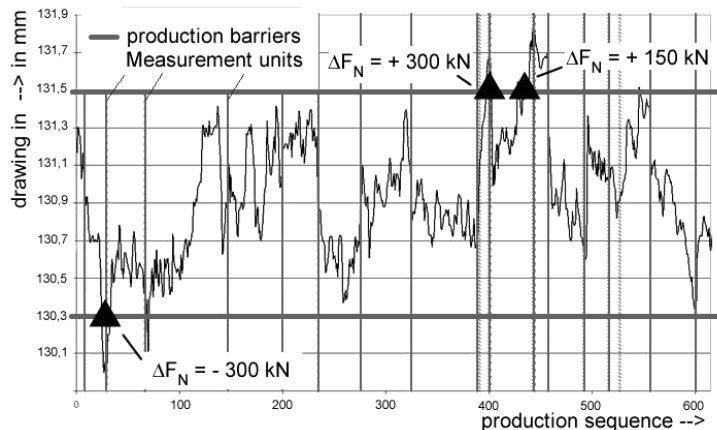
Fig. 17. Correction value output

In practice, the correction made and recorded in the actual production process would have been detected considerably earlier than necessary, as a result of which

the aforementioned 77 parts classified as defective would have been reduced to fewer than 25.

Process monitoring was installed for this component following some test measurements and has been implemented for some months now. This made it possible to halve the proportion of components requiring subsequent work from a total of approximately 8% previously to approximately 4% currently. At the same time, the proportion of components which could not be reworked (scrap components) fell from approximately 3% to less than 1%.

Figure 18 shows a signalled stoppage of the press line. The decision was taken only after the integrated trend analysis had excluded one-off outliers. In the case illustrated, after the fourth component with characteristics outside the established limits for an acceptable component (drawing in of the flange too great) it was recommended that the blank holder force be increased by 400 kN.

Without a response from the process monitoring system, it would only have been possible to perform a visual inspection at the end of the press line after a further 12 components.
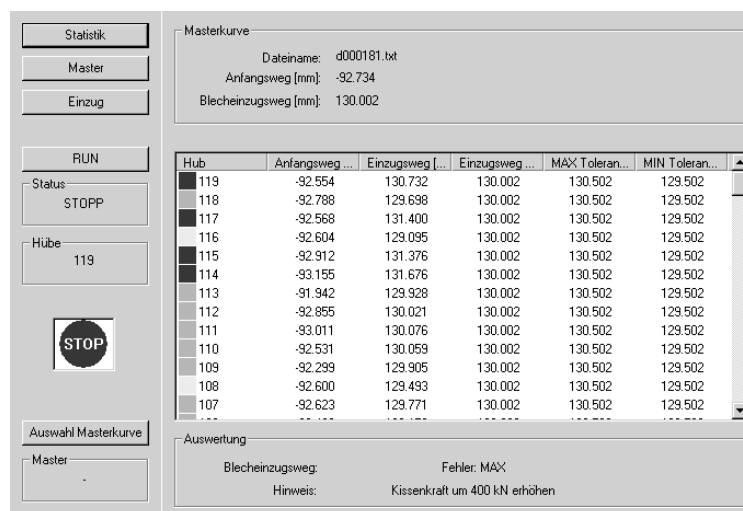
Fig. 18. Screenshot of process monitoring

Work is currently under way on a new, more highly developed system enabling more accurate and even earlier detection of defective parts. This system can also be used for other components without any problem.

5.4. Improving dimensional stability

Inextricably linked with process monitoring and classification of components as a good or defective is the issue of the dimensional stability of the components.

To this end, the respective measurement data of over 120 components were analysed with and without process monitoring. These components again originated from at least 8 different production cycles over a period of 6 months, so as to eliminate any effect from equivalent material properties.

The cutting plane of the component measured in Figure 19 lies in the direction of the laser beam 1 (Figure 13).

It should be noted that the tolerance ranges of the individual measuring points are essentially smaller with process monitoring than without. This is particularly apparent in respect of the two measurement points 2 and 9, where the reduction amounts to approx. 0.4 mm.

Ultimately, especially for the assembly of connecting parts, this means less expense, since the components supplied have lower tolerances in relation to each other.
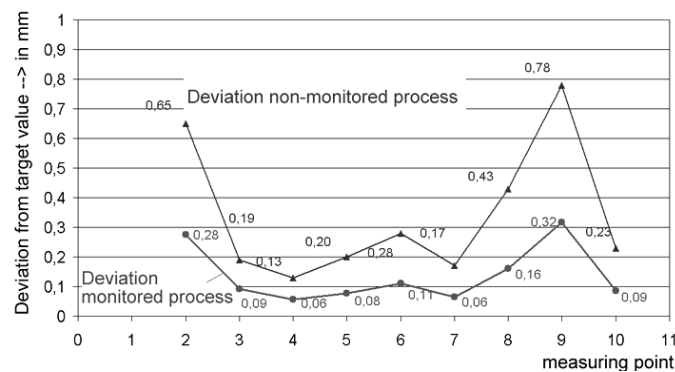
Fig. 19. Dimensional stability

5.5. Advantages of process monitoring

By monitoring the drawing phase, analytical data is made available locally to the press operator, on the basis of which it is possible to:

• identify defective components at a very early stage or to cancel production in advance,

• to exclude identified defective parts from the process and thereby feed only components which meet specifications into the subsequent assembly process,

• to decide, on the basis of the trend analysis, whether this is merely a short-term fluctuation or whether the production process is drifting towards production of defective parts,

• to take suitable steps to avoid production of defective parts,

• to use the automated features of the monitoring software to relay corrections which were previously made manually directly to the plant ("simple" process control),

• in general, to produce components with smaller dimensional tolerance ranges, thus making assembly easier.

In addition, of course, the system described above can also be used for other forming operations (e.g. tryout of tools or bending operations) in which a variable and process-relevant parameter can be recorded by measurement technology.

6. Process control systems

In contrast to process monitoring systems, in which intervention in the production process is initiated only in the event of limit values being approached, the process control systems developed by the Fraunhofer IWU intervene whenever deviations are identified in the production of each individual component.

The objective of such systems is therefore to reproduce a master component – in such a way that discrepancies resulting from the sum of the process fluctuations that occur are identified and can be corrected even before the stroke is completed.

Again, this is based on detection of the drawing in of the flange – on this occasion as a control parameter, the characteristics of which reflect all the influences on the drawing process. In addition to the unwanted fluctuations in material specifications, these include factors such as the tolerances in sheet metal thickness or variations in basic lubrication. In [10–14], based on these factors, it is demonstrated that the drawing in of the sheet metal is a suitable control parameter for establishing a closed loop control circuit. Additional findings from these studies include the following:

• quantitative evidence showing that changes in all important process parameters can be compensated for by the control system,

• both sensor technology and the closed-loop control circuit must respond with great sensitivity to variations in process parameters; the sensor technology routinely used to date to detect the drawing in of the sheet metal must however be improved,

• control circuits function independently of the cause of the malfunction, and without specifying the cause,

• evidence, based on a number of examples, of the viability in practical terms in series production.

The basis for process control continues to be the (locally) flexibly configurable blank holder area of the tool. Ultimately, it is only as a result of this constructive measure in relation to active components that a change in the material flow can be achieved by varying the local surface pressure in the blank holder/workpiece/matrix contact system, thus making it possible to control the process.

Two control circuits implemented at the Fraunhofer IWU are described below.

6.1. "Intelligent machine" control circuit

This design concept is intended for presses with multi-point drawing installations, since modification of surface pressure is achieved by changing the spindle sleeve force at the control point. The principle of this variant is illustrated in Figure 20.
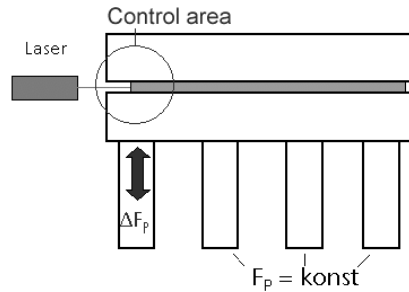
Fig. 20. "Intelligent machine" control circuit

In order to detect the drawing in of the sheet metal, a laser triangulation system is used which is mounted on the outside of the tool. During the stroke of the press, the laser detects the drawing in of the sheet metal at relevant points in the gap between blank holder and the matrix. Under optimum process conditions, this drawing in curve characterises the master curve to be used at a later stage. On this basis it is possible to compare the drawing-in curves of subsequent workpieces with the specified path values, with intervention by the control system where necessary.

The process control and regulation software to be developed will be integrated in the existing press software, the number of sensors being determined by the number of points at which control is required.

Drawing in characteristics of the flange. Figure 21 shows the drawing in characteristics of the flange in several consecutive components. The central area of a good component, in which minor process deviations result in minimal changes in drawing behaviour, can clearly be seen.
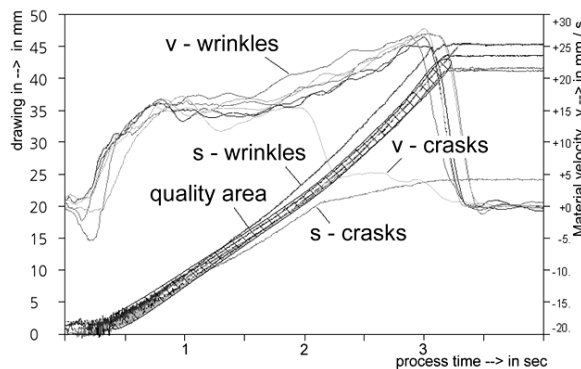
Fig. 21. Process-determined deviations in drawing-in characteristics

Although the curves which are characteristic of cracked and wrinkled components constitute more serious deviations, both conditions can be identified by the sensors a long time in advance of the actual malfunction occurring – both by means of the path

signal and by the velocity profile. This behaviour is used for the purpose of process control.

"Intelligent machine" process control. For complex sheet metal components in which the degree of deformation lies relatively close to the deformation curve limit, there is a whole host of drawing in curves to be recorded, as is shown in Figure 19. The working zone between the wrinkle and crack failure limits is thus formed. One of the recorded curves should be used as a master curve, to be selected in accordance with the particular characteristics of the existing workpiece geometry. In normal circumstances, an equal distance between the curves for wrinkle and crack formation is recommended. It is however safer to determine a curve in the upper third, i.e. nearer to the wrinkle limit, since it is generally more advantageous to opt for a greater distance from the crack limit. In addition, in the case of large components, flange areas are usually cut in an additional operation, eliminating existing or incipient wrinkle formation.

Based on the master curve, the control system is able to make constant comparisons between the actual and target values for the drawing in of the flange and to intervene to make corrections as necessary. This cycle is illustrated in Figure 22. At the beginning of the drawing process, the material flows in too quickly, so the local hold-down pressure is increased accordingly (the surface pressure increases). For half of the drawing process there is a reversal in the drawing in of the flange; the drawing in process is too slow. In response, the blank holder force is reduced (the surface pressure drops) and the course of the drawing in path is almost identical to the specified master value. This is contrasted with the drawing in of another component without controls.
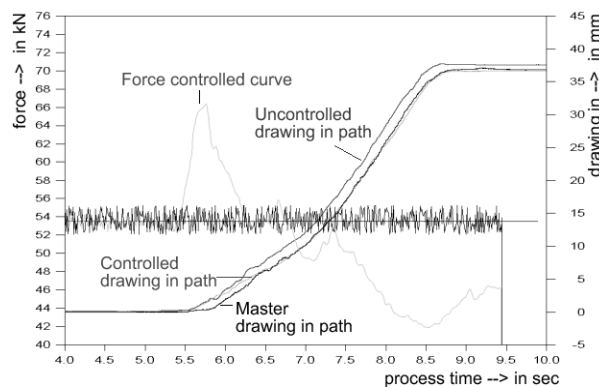
Fig. 22. "Intelligent press" control curves

This type of control is essentially recommended for plants with existing multi-point cushions, since in most cases all the technical requirements in terms of hardware in the press are already present. The installation of the regulator in the control system is therefore a profitable one-off investment.

6.2. "Intelligent tool" control circuit

In contrast with the control variant outlined in 6.1, there are no mechanical prerequisites for the intelligent tool (multi-point drawing installation).

The piezo actuator previously described (see 4.2) acts as the sensor-actuator system in conjunction with a load cell. This configuration can be integrated within the tool and can therefore be used in any installation, since complete disconnection from the press and its control system is possible. The underlying principle of this variant is illustrated in Figure 23.

The drawing in of the flange likewise functions as a control parameter which is measured indirectly via the surface pressure. This is accomplished by a force sensor at the point in question. The control variable here is again the blank holder force, which is modified by a piezo actuator on the basis of the sensor values.
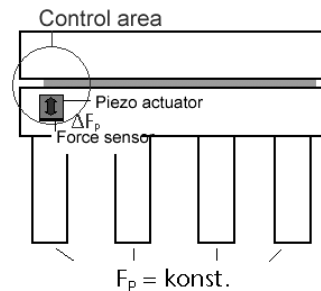
Fig. 23. "Intelligent tool" control circuit
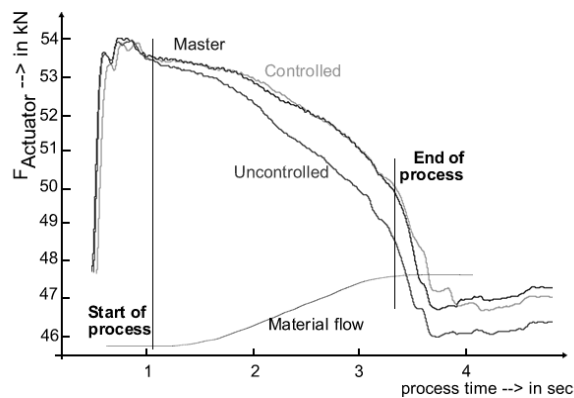
Fig. 24. Resulting force curves in the piezo actuator

The principle can be explained as follows: the piezo actuator, mechanically and electrically pre-loaded to the nominal load, acts as a spring in conjunction with the local torsion-elastic tool. With the progressive drawing in of the flange, the tool surface

yields as a result of the pressure of the piezo actuator from beneath (in total less than 0.05 mm). This results in expansion (= release) of the piezo elements, and in the load cell a lesser force with greater lift is measured. Figure 24 shows characteristics of the forming process detected in this manner.

A component manufactured under optimum conditions therefore possesses an additional master value in the form of local surface pressure, which can be assigned directly to the drawing in of the flange. This serves as the basis for the control system in which the electrical voltage is used as a control variable, expanding the piezo elements in the actuators to a greater or lesser extent.

This type of regulation system is recommended in particular for older plants and components which have few (or possibly only one) critical component area. Since the sensor can be used for several tools, this too ultimately constitutes a profitable investment.

6.3. Advantages of process control systems

A control system permits intervention during the forming process to take corrective action after a comparison of target and actual values. The sensor and actuator systems showed here work with sufficiently high cycle rates (> 50 Hz) to enable minor deviations to be detected at the earliest possible stage. This has the following advantages:

- the control system works independently of the cause,
- any defective components are identified as soon as they are created and are immediately eliminated by the control system,
- the working method is fully automated; there is no need for manual intervention by a press operator,
- the process capability in respect of the component under investigation rose from CPK = 0.27 to CPK = 1.31, i.e. the process has long-term capability.

The design concept for the control system used here can also be used for other forming technologies.

7. Summary

Process stability in deep drawing was significantly increased as a result of the process monitoring and control systems outlined above. The dimensional stability of the components produced under such conditions was also increased.

In order to achieve this, identification of defects at an early stage was followed by intervention in the production process in each individual case to adjust the blank holder force. This was accomplished independently of the respective initiator (e.g. undesirable fluctuations in material specifications, sheet metal thickness, tribology, etc.) and in each case the drawing in of the flange was used as the control or monitoring parameter.

The systems used and presented here are already viable in terms of their inclusion in processes, as has been demonstrated on many occasions under series production conditions. However, sensor technology still has potential for further development. An approach focusing on non-contact sensors which are integrated within the tool is undoubtedly the way forward.

References

[1] Lüpfert K.H.: *Maßhaltigkeit und Prozessfähigkeit von Karosseriepressteilen aus Hochfestem Material*, in: Praxis-Forum 22/94, Tagung Karosserierohbau in Bad Nauheim.

[2] Seidel H.J.: *Prozessregelung basierend auf Stoffflussmessung beim tiefziehen*, Sonderforschungsbereich SFB 362 "Fertigen in Feinblech", 2005.

[3] Doege E., Brendel, Schomaker: *Fehlerdiagnose – Überwachungssysteme mit Sensortechnik sichern die Fertigungsqualität beim umformen*, Maschinenmarkt, Würzburg, 98, 1992, 42, pp. 52–58.

[4] Siegert K., Wagner S., Ziegler M.: *Closed loop binder force system*, Vortrag zur SAE-Tagung Detroit, MI/USA, 1996.

[5] Bräunlich H.: *Blecheinzugregelung beim tiefziehen mit Niederhalter – ein Beitrag zur Erhöhung der Prozessstabilität*, Dissertation, FhG IWU Chemnitz, 2001.

[6] Klose L.: *Einsatzplanung von Mehrpunktziehanlagen auf Einfachwirkenden pressen*, Dissertation, FhG IWU Chemnitz, 2003.

[7] Bräunlich H.: *Auf dem Weg zum beherrschten tiefziehprozess*, Vortrag zum 2. Kolloquium Prozesssicherheit in der Blechbearbeitung, 13–14.04.99, Chemnitz.

[8] Scheffler S., Bräunlich H.: *Regelstrategien für Blechumformprozesse (Tiefziehen)*, Viertes Industriekolloquium SFB 362, Clausthal 11–12.02.2004.

[9] Lüthje H., Nordmann K.: *Oberflächensensoren überwachen Werkzeugschneiden*, F&M Feinwerktechnik, Mikrotechnik & Mikroelektronik, 109, 2001, 5, pp. 56–58.

[10] Forstmann U.: *Induktive Wegsensoren zur Überwachung und Regelung des Blecheinzugs beim tiefziehen*, FhG-IPK Berlin, 2000.

[11] Scheffler S.: *Einsatzeignung von Ziehkissen*, Forschungsvereinigung Werkzeugmaschinen und Fertigungstechnik e.V., 2004.

[12] Straube, O.: *Untersuchungen zum Aufbau einer Prozessregelkette für das Ziehen von Karosserieteilen*, Dissertation, Berlin, Carl-Hanser-Verlag: München, Wien, 1994.

[13] Liewald M.; Spur G.; Straube O.: *Verfahren zum selbsttätigen prozessoptimalen Regeln von Ziehvorgängen in Pressen und hierzu geeignete Ziehpresse*, DE 43 38 828 A1.

[14] Spur G., Thoms V., Liewald M., Straube O.: *Regelung des Tiefziehprozesses in der Preßteilefertigung mit dem Blechkanteneinlauf als Regelgröße*, Blech, Rohre, Profile, Bamberg 41, 4, 1994, pp. 237–240.

Monitorowanie i sterowanie procesu poprzez sprzężenie zwrotne

Istnieje pewna liczba czynników, które mogą poważnie wpłynąć na proces kształtowania blach. Poprzez określenie zmienności procesu staje się możliwe poprawienie procesu produkcji. W tym celu monitorowanie lub sterownie procesami poprzez sprzężenie zwrotne stanowi

ważne narzędzie pozwalające na redukcję wad, zmniejszenie ilości poprawek i lepszą jakość końcowych produktów. Fraunhofer Institute for Machine Tools and Forming Technology (IWU) w Chemnitz zbadał typowe zmienne procesu, takie jak np. przemieszczenie kołnierza jako podstawę dla systemów kontroli. Różne rodzaje bezkontaktowych sensorów zostały z powodzeniem przetestowane. Wielopunktowa poduszka lub zintegrowane piezoelementy w połączeniu z narzędziami skrętno-sprężystymi zostały użyte jako systemy reagujące. Kompletny system kontroli opartym na inteligentnych algorytmach został opracowany.

Statistical analysis of solar radiation models onto inclined planes for climatic conditions of Lower Silesia in Poland

D. WŁODARCZYK, H. NOWAK

Wrocław University of Technology, Wybrzeże Wyspiańskiego 25, 50-370 Wrocław, Poland

The paper presents the statistical analysis' results of major models of the solar radiation intensity onto an inclined plane. Models with various degrees of complexity: from the simplest classical isotropic model to the most complex anisotropic model (the Perez model) were analyzed. The data yielded by the theoretical models were compared with a four-year measurement database from the actinometric station in the SolarLAB Photovoltaic Laboratory in Wrocław. Also the potential benefits of using albedo data characteristic of the measurement location versus the classical 0.2 albedo assumption were examined.

Keywords: *intensity of solar radiation, actinometric measurements, statistical analysis, albedo*

1. Introduction

When calculating, for renewable energy use purposes, the solar gains of a building or that of planes exposed to solar radiation (e.g. solar collectors and photovoltaic panels) it is essential to correctly model the intensity of the solar radiation incident on inclined planes. This particularly applies to Poland where as a rule no measurements of solar radiation onto inclined planes are conducted in the actinometric stations. The norm in the stations is to measure the intensity of total solar radiation onto horizontal plane; sometimes also diffuse radiation is measured. Theoretical models of the intensity of solar radiation onto inclined planes use the values of solar radiation onto horizontal plane. Thanks to the models one can calculate the solar gains of a plane with any inclination and azimuth.

This paper presents the results of a comparative statistical analysis (based on a four-year measurement database from the actinometric station in the SolarLAB Photovoltaic Laboratory in Wrocław) of the following models of solar radiation onto inclined planes: the isotropic model [1]0, the Koronakis model [2], the Jimenez & Castro model [3], the circumsolar model [4], the Bugler model [5], the Temps & Coulson model [6], the Klucher model [7], the Hay model [8], the Ma & Iqbal model [9], the Skartveit & Olseth model [10], the Reindl model [11], the Gueymard model [12], the Muneer model [13] and the Perez model [14]. The models differ in their treatment of diffuse radiation. This is the first such comprehensive analysis of models of solar radiation onto inclined planes for the actinometric conditions prevailing in Poland. The analyses published before were limited to only a few models [15−17].

Moreover, the validity of the use of the albedo values characteristic of the measurement location versus the traditional isotropic assumption, according to which on the average 20% of the annual solar radiation incident on a horizontal surface in a measurement location is reflected from this surface, is tested.

2. Theoretical modelling of solar radiation onto inclined planes

The theoretical models discussed here are based on measurements of the total and diffuse radiation onto a horizontal plane and calculate the intensity of solar radiation onto an inclined plane, being the sum of the beam component, the diffuse component and the reflected component 0:

$$I_\beta = I_{b,\beta} + I_{d,\beta} + I_{r,\beta},$$ (1)

where:

$I_{b,\beta}$ – the intensity of beam radiation onto an inclined plane [W/m^2],

$I_{d,\beta}$ – the intensity of diffuse radiation onto an inclined plane [W/m^2],

$I_{r,\beta}$ – the intensity of reflected radiation onto an inclined plane [W/m^2].

2.1. Intensity of beam radiation

The intensity of beam radiation onto an inclined plane is calculated by converting the corresponding value for a horizontal plane. The intensity can be described by the formula:

$$I_{b,\beta} = I_b \cdot r_b,$$ (2)

where:

I_b – the intensity of beam radiation onto a horizontal plane [W/m^2],

r_b – a geometrical index being a ratio of the intensity of beam radiation onto an inclined plane to the corresponding intensity of beam radiation onto a horizontal plane.

In most cases, beam radiation measurement data are not available since special sensors (pyrheliometers) are needed to acquire them. Considering that solar radiation onto a horizontal plane is composed of beam radiation and diffuse radiation, in order to calculate the beam radiation one needs the total radiation value and the diffuse radiation value, which are much easier to measure. If only the total radiation onto the horizontal plane is known, in order to calculate the diffuse component fraction one should use theoretical models based on clearness index k_T. The authors presented the results of a statistical analysis of such models for the climatic conditions prevailing in Poland in papers [18] and [19].

2.2. Intensity of diffuse radiation

The second term of Equation (1) represents the intensity of diffuse radiation onto an inclined plane. Diffuse radiation is very difficult to model mathematically whereby researchers have divergent views on how to describe diffuse radiation onto an inclined plane. Generally, one can distinguish three groups of models: isotropic models, pseudo-isotropic models and anisotropic models. They differ in the division of the sky into regions with normal and elevated diffuse radiation intensity. The regions of elevated intensity are the circumsolar region and the region near the horizon line.

The isotropic model assumes that the distribution of diffuse radiation intensity is uniform over the whole sky. Pseudo-isotropic models introduce some cosmetic corrections concerning sky anisotropy into the isotropic model. Anisotropic models include appropriate modules representing areas of elevated diffuse radiation.

The isotropic model, also called the Liu & Jordan model, was published in 1962 [1]. It assumed that diffuse radiation intensity was uniformly distributed over the whole sky and that the amount of diffuse radiation incident on an inclined plane depended only on its inclination angle β:

$$I_{d,\beta} = \frac{1}{2} I_d \left(1 + \cos\beta\right),\tag{3}$$

where I_d is the intensity of diffuse radiation onto a horizontal plane [W/m^2].

Because of its simplicity, the Liu & Jordan model is often used in engineering calculations, but the greatly simplified treatment of diffuse radiation intensity distribution over the sky often leads to less accurate results in comparison with the actual meteorological data. According to [13], the isotropic model yields good results only under completely overcast sky conditions. The diversity of sky cover contributes to large errors generated by the Liu & Jordan model.

In 1982 Jimenez and Castro [20] carried out studies of sky solar radiation and found that the distribution of sky diffuse radiation is anisotropic. They also called into question the applicability of the Liu & Jordan model to inclined surfaces which are not oriented towards the Sun.

The isotropic sky assumption was also questioned in [21] where it was found that the sky's southern part is responsible for 63% of the total intensity of diffuse radiation.

Taking the above into account Koronakis [2] modified Equation (3) which for a vertical plane oriented southwards covers 66.7% of the total sky radiation:

$$I_{d,\beta} = \frac{1}{3} I_d \left(2 + \cos\beta\right).\tag{4}$$

Another pseudoisotropic model [3] assumed that diffuse radiation onto a horizontal plane amounts to about 20% of the total radiation. Hence Equation (3) takes the form:

$$I_{d,\beta} = \frac{1}{2} \cdot 0.2I(1 + \cos\beta),$$
(5)

where I is the intensity of total solar radiation onto a horizontal plane [W/m^2].

The first anisotropic model [4] is applicable only to a cloudless sky since it assumes that the whole diffuse radiation comes from the sky sector in which the Sun's disc is located at a given moment. This model treats diffuse radiation as beam radiation:

$$I_{d,\beta} = I_d \cdot r_b.$$
(6)

Because of its assumption the model is often referred to as the circumsolar model.

Bugler [5] modified the isotropic model by adding modules for the diffuse radiation coming from the Sun's disc and for the radiation from the rest of the sky, dependent on the angular height of the Sun over the horizon. The Bugler equation is as follows:

$$I_{d,\beta} = \left[\left(I_d - 0.05 \frac{I_{b,\beta}}{\cos\theta_z} \right) \frac{1 + \cos\beta}{2} \right] + 0.05 I_{b,\beta} \cos\theta.$$
(7)

Temps and Coulson [6] modified Equation (3) by introducing two terms representing diffuse radiation coming from the vicinity of the Sun's disc (P_1) and sky radiation from the region close to the horizon (P_2).

$$I_{d,\beta} = \frac{1}{2} I_d (1 + \cos\beta) P_1 P_2,$$
(8)

where:

$$P_1 = 1 + \cos^2\theta \cdot \left(\sin^3\theta_z \right),$$
(9)

$$P_2 = 1 + \sin^3\left(\frac{\beta}{2} \right).$$
(10)

Ultimately the Temps and Coulson equation takes the form:

$$I_{d,\beta} = \frac{1}{2} I_d (1 + \cos\beta) \left[1 + \cos^2\theta \cdot \left(\sin^3\theta_z \right) \right] \left[1 + \sin^3\left(\frac{\beta}{2} \right) \right].$$
(11)

Equation (3) was modified by Klucher in 1979 [7]. The changes concerned the assessment of cloudiness by the model, i.e. function F determining the degree of cloud cover:

$$F = 1 - \left(\frac{I_d}{I}\right)^2.$$ (12)

The Klucher model is described by this equation:

$$I_{d,\beta} = I_d \left[\frac{1}{2}\left(1 + \cos\left(\frac{\beta}{2}\right)\right)\right]\left[1 + F\cos^2\theta \cdot \left(\sin^3\theta_z\right)\right]\left[1 + F\sin^3\left(\frac{\beta}{2}\right)\right].$$ (13)

Another anisotropic model is the Hay & Davies model [8] (commonly referred to as the Hay model) which assumes that sky diffuse radiation originates from two sources: the Sun's disc and the rest of the sky with isotropic diffuse radiation. The two components are described by anisotropy index F_{Hay}:

$$F_{Hay} = \frac{I_b}{I_0} = \frac{I - I_d}{I_0}.$$ (14)

According to the Hay model, the equation of the intensity of diffuse radiation onto an inclined plane has this form:

$$I_{d,\beta} = I_d \left[F_{Hay} \cdot \left(\frac{\cos\theta}{\cos\theta_z}\right) + \left(\frac{1 + \cos\beta}{2}\right) \cdot \left(1 - F_{Hay}\right)\right].$$ (15)

In 1983 Ma and Iqbal [9] proposed a model dividing diffuse radiation into radiation emitted by the circumsolar region and radiation emitted by the rest of the sky. Cloudiness is determined on the basis of atmosphere clearness index k_T:

$$I_{d,\beta} = I_d \left[k_T r_b + (1 - k_T)\cos^2\left(\frac{\beta}{2}\right)\right].$$ (16)

Another anisotropic model was proposed by Skartveit and Olseth in 1986 [10]. Solar radiation measurements carried out by them in Bergen (Norway) showed that a significant part of sky diffuse radiation under completely overcast sky conditions comes from the sky region around the zenith. This effect vanishes when cloud cover disappears. Hence the model includes correcting factor Z:

$$\begin{cases} Z = 0.3 - 2F_{Hay} & \text{for} \quad F_{Hay} < 0.15, \\ Z = 0 & \text{for} \quad F_{Hay} \geq 0.15. \end{cases} \tag{17}$$

Then diffuse radiation onto an inclined plane is expressed by:

$$I_{d,\beta} = I_d \left[F_{Hay} r_b + Z \cos \beta + \left(1 - F_{Hay} - Z\right)\left(1 + \frac{\cos \beta}{2}\right) - S(\omega, \Omega_i) \right]. \tag{18}$$

The last term in Equation (18) represents the effect of obstacles obscuring the horizon, which block some of the diffuse radiation incident on the inclined plane. In most cases, this term is neglected since the data usually come from actinometric stations which by assumption are located in open terrain without any major natural or artificial obstacles.

To the Hay model Reindl et al. [11] added a module for the diffuse radiation coming from the region near the horizon line. They found that the intensity of diffuse radiation originating from this region decreases as sky overcast increases and so they included modulating function f_R in the module:

$$f_R = \sqrt{\frac{I_b}{I}}. \tag{19}$$

The Reindl equation is as follows:

$$I_{d,\beta} = I_d \left[\left(1 - F_{Hay}\right) \cdot \left(\frac{1 + \cos \beta}{2}\right) \cdot \left(1 + f_R \cdot \sin^3\left(\frac{\beta}{2}\right)\right) + F_{Hay} r_b \right]. \tag{20}$$

The function modulating the intensity of diffuse radiation coming from the region near the horizon line works relatively simply. When the sky is fully overcast, beam radiation intensity I_b is close to zero and so function f_R also becomes zero. At this moment the model assumes that the diffuse radiation in the region near the horizon line is isotropic.

In 1987 Gueymard [12] proposed to calculate diffuse radiation onto a horizontal plane under partly overcast sky conditions using a linear combination of radiation indices: R_{d1} – for completely overcast sky and R_{d0} – for cloudless sky:

$$I_{d,\beta} = I_d \left[\left(1 - N_G\right) R_{d0} + N_G R_{d1} \right], \tag{21}$$

where – a sky cloudiness function. Since, as a rule, cloudiness data are not generally available, Guemard based his function N_G on solar radiation data. Similarly, indices

R_{d1} and R_{d0} are calculated from empirical equations derived on the basis of solar radiation data.

The Muneer anisotropic model [13] considers separately planes illuminated with sunlight and the shaded ones. In addition, it divides planes illuminated with sunlight depending on sky cloudiness.

The equation of the intensity of diffuse radiation onto shaded planes and planes illuminated with sunlight under a cloudy sky (a theoretical possibility of illumination exists because of the position of the Sun over the plane) is as follows:

$$I_{d,\beta} = I_d \left[\cos^2\left(\frac{\beta}{2}\right) + \frac{2b}{\pi(3+2b)} \cdot \left(\sin\beta - \beta\cos\beta - \pi\sin^2\left(\frac{\beta}{2}\right) \right) \right], \qquad (22)$$

while for planes illuminated with sunlight under a cloudless sky it has this form:

$$I_{d,\beta} = I_d \cdot \left[\cos^2\left(\frac{\beta}{2}\right) + \frac{2b}{\pi(3+2b)} \cdot \left(\sin\beta - \beta\cos\beta - \pi\sin^2\left(\frac{\beta}{2}\right) \right) \right] \cdot \left(1 - F_{Hay}\right)$$
$$+ I_d \cdot F_{Hay} \left(\frac{\cos\theta}{\cos\theta_z} \right). \qquad (23)$$

According to Muneer [13], coefficient b in Equation (22) is constant and amounts to 2.5. It is variable in Equation (23) and is calculated from the following relation derived for data coming from 14 locations all over the world:

$$\frac{2b}{\pi(3+2b)} = 0.04 - 0.82F_{Hay} - 2.026F_{Hay}^2. \qquad (24)$$

The Perez model [14] is one of the most often used anisotropic models because of its results which place it among the top most accurate calculation models. The model assumes three sky regions with different diffuse radiation intensities: the circumsolar region, the region over the horizon line and the rest of the sky which is isotropic. According to Perez, the equation of the intensity of solar radiation onto an inclined plane looks as follows:

$$I_{d,\beta} = I_d \left[(1 - F_1)\frac{(1+\cos\beta)}{2} + F_1\frac{a}{b} + F_2\sin\beta \right], \qquad (25)$$

where:

F_1 and F_2 are sky brightness coefficients for respectively the circumsolar region and the region above the horizon line. Coefficients a and b take into account the angle

of incidence of diffuse radiation from the circumsolar disc onto inclined and horizontal planes.

Coefficients a and b are calculated from the equations of solar geometry. Indices F_1 and F_2 are calculated from the same equations, but additionally using an empirically determined set of coefficients published in [14].

2.3. Intensity of reflected radiation

The last term of Equation (1) represents radiation $I_{r,\beta}$ reflected onto an inclined plane. Assuming that the reflected rays are diffuse and the coefficients of reflection of the beam and diffuse rays are identical, $I_{r,\beta}$ is calculated from the formula:

$$I_{r,\beta} = \frac{1}{2}\rho I(1-\cos\beta),$$ (26)

where ρ is the ground surface albedo.

Reflected radiation has less influence on the intensity of total radiation onto inclined planes. Nevertheless proper modelling of this component, particularly when no measurements can be taken with an albedometer in the place where solar radiation is analyzed, contributes to higher accuracy of the whole mathematical model of total radiation.

The intensity of reflected radiation directly depends on the albedo of the surface on which solar radiation falls (albedo is a ratio of the intensity of the radiation reflected from a surface to the total radiation incident on this surface).

When determining the intensity of reflected radiation one should also make an assumption concerning the isotropy or anisotropy of this component of total radiation.

One of the first albedo models was the Liu and Jordan assumption of 1963 [22], fixing albedo (ρ) at 0.2 for total radiation incident on a horizontal plane:

$$I_r = 0.2 \cdot I,$$ (27)

where:

I_r – the intensity of radiation reflected from a horizontal plane [W/m^2],

I – the intensity of total solar radiation onto a horizontal plane [W/m^2].

Value 0.2 in the Liu & Jordan model is constant regardless of the location, the climate, the solar geometry, the season, the time of the day, etc. The model is commonly used when albedo measurements with an albedometer are impossible.

In solar radiation calculations one can also use the albedo values for a given location, based on actinometric measurements conducted for many years.

In 1990 Podogrocki et al. [23] developed standard average monthly albedo values for the whole year for the actinometric conditions prevailing in Poland. The values are shown in Table 1.

Table 1. Average albedo values for actinometric conditions prevailing in Poland [23]

Month	1	2	3	4	5	6	7	8	9	10	11	12
Albedo	0.45	0.39	0.20	0.18	0.21	0.21	0.19	0.21	0.20	0.21	0.24	0.43

As a part of the present research, the influence of the use of the classical albedo model versus the average monthly values under the climatic conditions prevailing in Poland on the statistical indicators yielded by the actinometric models was investigated.

3. Actinometric station and measurements methodology

The statistical analysis of the theoretical models was carried out on the basis of solar radiation measurements taken at the measurement station in the SolarLAB Photovoltaic Laboratory at the Faculty of Microsystems Electronics and Photonics at Wrocław University of Technology in the period from December 2002 to October 2006.

Fig. 1. Actinometric station in SolarLAB Photovoltaic Laboratory in Wrocław

Total radiation on a horizontal plane was measured with a CM21 Kipp&Zonen pyranometer. Diffuse radiation onto a horizontal plane was measured with a CM21 Kipp&Zonen pyranometer equipped with a diffusion ring. Total radiation onto an inclined plane was measured with a CM21 Kipp&Zonen pyranometer equipped with a CMV ventilation chamber. The pyranometer for measuring the intensity of total radiation onto an inclined plane was mounted in the plane of the photovoltaic modules tested in the SolarLab Laboratory (Figure 1). In order to ensure that a maximum

amount of solar energy reached the photovoltaic modules the inclination angle of the plane of the PV modules was adjustable to 35° and 50° in respectively the summer and winter season.

Data were automatically measured round the clock in two-second periods and subsequently integrated to one-hour periods by a computer controlled data logger.

4. Measurement database

Data for comparative analyses of solar radiation models should be checked for faulty data due to, for example, measuring system failures, terrain obstacles, etc. Equations eliminating the elements which do not meet the quality requirements are used for this purpose.

The CIE (Commission Internationale de l'Eclairage) [24] data quality requirements were applied to the solar radiation on horizontal plane data used for the calculations made as part of this research:

$$\begin{cases} 0 \leq I_d \leq 1.1I \\ 0 \leq I \leq 1.2I_0 \\ 0 \leq I_d \leq 0.8I_0 \\ 0 \leq I_b \leq I_0 \end{cases} \tag{28}$$

where:

I – the intensity of total solar radiation onto a horizontal plane [W/m^2],

I_d – the intensity of diffuse radiation onto a horizontal plane [W/m^2],

I_b – the intensity of beam radiation onto a horizontal plane [W/m^2],

I_0 – the intensity of solar radiation onto a horizontal plane at the atmosphere boundary [W/m^2].

Moreover, measurement values arousing suspicion that they could cause any of the sensors to hang up (identical measurement values in consecutive hours) were removed from the database. Ultimately, the database amounted to 9681 hours.

Various statistical indicators informing about errors generated by theoretical models relative to measurement data, are used to evaluate the models.

The main statistical indicators used for evaluating solar radiation models are those suggested by Iqbal [4] and Notton [25]:

- MBE – a mean bias error,
- RMSE – a root mean square error,
- CC – a correlation coefficient.

MBE and RMSE can also be expressed in relative values referred to the average value of the measured solar radiation unit, i.e. MBE [%] and RMSE [%]. This way of expressing MBE and RMSE is proposed in, among others, [25].

5. Statistical analysis of theoretical models

5.1. Standard albedo model

The results of the statistical analyses of the solar radiation models for the standard albedo model are shown in Tables 2, 3 and 4.

Table 2. Statistical indicators of solar radiation models at inclination of 35° for standard albedo model

Model	Statistical indicators of tested models				
	MBE	RMSE	MBE[%]	RMSE[%]	CC
	[Wh/m^2]	[Wh/m^2]	[%]	[%]	[–]
Isotropic	−8.39	121.17	−2.37	34.26	0.9069
Koronakis	−4.07	120.75	−1.15	34.14	0.9075
Jimenez & Castro	36.14	127.55	10.22	36.07	0.9039
Circumsolar	61.31	143.43	17.34	40.56	0.8968
Bugler	−19.10	120.65	−5.40	34.11	0.9092
Temps & Coulson	28.88	122.49	8.17	34.64	0.9128
Klucher	20.11	125.05	5.69	35.36	0.9081
Hay	9.08	122.92	2.57	34.76	0.9071
Ma & Iqbal	24.49	125.13	6.92	35.38	0.9079
Skartveit & Olseth	49.70	133.81	14.05	37.83	0.9091
Reindl	3.97	123.14	1.12	34.82	0.9063
Gueymard	1.10	123.26	0.31	34.85	0.9061
Muneer	7.71	125.64	2.18	35.53	0.9045
Perez	9.92	118.95	2.81	33.63	0.9130

Table 3. Statistical indicators of solar radiation models at inclination of 50° for standard albedo model

Model	Statistical indicators of tested models				
	MBE	RMSE	MBE[%]	RMSE[%]	CC
	[Wh/m^2]	[Wh/m^2]	[%]	[%]	[–]
Isotropic	−20.31	116.33	−5.25	30.09	0.9098
Koronakis	−10.73	113.39	−2.78	29.32	0.9127
Jimenez & Castro	28.16	123.92	7.28	32.05	0.8997
Circumsolar	59.02	148.81	15.26	38.49	0.8798
Bugler	−29.87	114.87	−7.72	29.71	0.9155
Temps & Coulson	24.44	113.07	6.32	29.24	0.9184
Klucher	26.13	118.78	6.76	30.72	0.9129
Hay	11.18	114.37	2.89	29.58	0.9135
Ma & Iqbal	18.78	121.61	4.86	31.45	0.9054
Skartveit & Olseth	46.13	124.68	11.93	32.25	0.9134
Reindl	−2.12	120.65	−0.55	31.20	0.9031
Gueymard	−7.48	121.23	−1.93	31.35	0.9027
Muneer	3.68	123.79	0.95	32.02	0.9010
Perez	2.91	114.31	0.75	29.56	0.9127

Table 4. Statistical indicators of solar radiation models for whole measurement database for standard albedo model

Model	Statistical indicators of tested models				
	MBE	RMSE	MBE[%]	RMSE[%]	CC
	[Wh/m^2]	[Wh/m^2]	[%]	[%]	[-]
Isotropic	−13.57	119.09	−3.69	32.36	0.9080
Koronakis	−6.97	117.60	−1.89	31.96	0.9098
Jimenez & Castro	32.67	125.99	8.88	34.23	0.9023
Circumsolar	60.32	145.79	16.39	39.62	0.8899
Bugler	−23.78	118.17	−6.46	32.11	0.9118
Temps & Coulson	26.95	118.49	7.32	32.20	0.9153
Klucher	22.73	122.36	6.18	33.25	0.9104
Hay	9.99	119.28	2.71	32.41	0.9100
Ma & Iqbal	22.00	123.61	5.98	33.59	0.9071
Skartveit & Olseth	48.14	129.91	13.08	35.30	0.9110
Reindl	1.32	122.06	0.36	33.17	0.9052
Gueymard	−2.63	122.39	−0.72	33.26	0.9048
Muneer	5.95	124.84	1.62	33.92	0.9033
Perez	6.87	116.95	1.87	31.78	0.9130

For the classical albedo model at a plane inclination angle of 35° the best result as regards MBE [%] (value 0.31%) was achieved by the Gueymard model. Among the top five models most accurate with regard to this parameters there were: the Reindl model, the Koronakis model, the Muneer model and the isotropic model. The lowest RMSE [%] of 33.63% was scored by the Perez model. Low RMSE [%] values were also scored by: the Bugler model, the Koronakis model, the isotropic model and the Temps & Coulson model. The highest CC of 0.9130 was scored by the Perez model. The other models with a high correlation coefficient were: the Temps & Coulson model, the Bugler model, the Skartveit and Olseth model and the Klucher model.

In the case of the classical albedo model at an angle of inclination of the plane with a pyranometer amounting to 50°, the lowest MBE [%] of −0.55% was scored by the Reindl model. Also the Perez model, the Muneer model, the Gueymard and the Koronakis model scored a low MBE [%]. The lowest RMSE [%] of 29.24% was scored by the Temps & Coulson model. The other models generating a low RMSE [%] were: the Koronakis model, the Perez model, the Hay model and the Bugler model. As regards CC, the highest value of 0.9184 was achieved by the Temps & Coulson model. The other models with a high correlation coefficient were: the Bugler model, the Hay model, the Skartveit & Olseth model and the Perez model.

For the whole database covering the two inclination angles and using the classical albedo model the lowest mean bias error of 0.36% was scored by the Reindl model (Figure 2). Also the Guemard model, the Muneer model, the Perez model and the Koronakis model achieved low MBEs. The lowest RMSE [%] of 31.78% was scored by the Perez model. The other models with low relative root means square errors

were: the Koronakis model, the Bugler model, the Temps & Coulson model and the Gueymard model. The Temps & Coulson model achieved the highest correlation coefficient for the data base covering the two inclination angles of the pyranometer plane. The other models with a high CC were: the Perez model, the Bugler model, the Skartveit & Olseth model and the Klucher model.
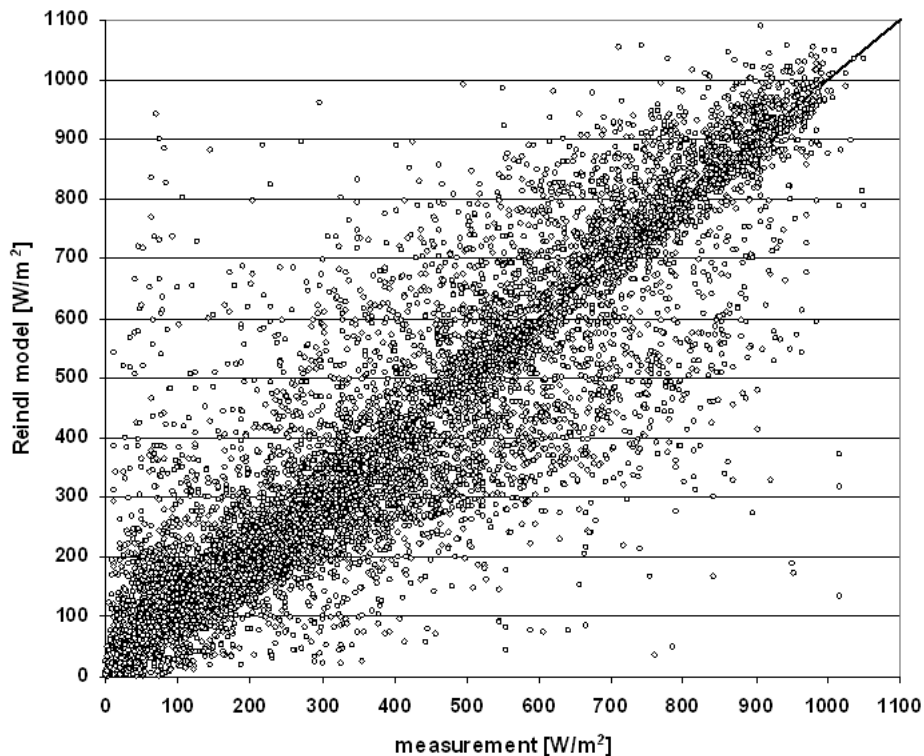

Fig. 2. Measured data versus theoretical Reindl model data
for whole measurement database and 0.20 albedo model

5.2. Average monthly albedo

The results of the statistical analyses of the models for the average monthly albedos [23] are shown in Tables 5, 6 and 7.

According to Table 2 and Table 5, the use of the average monthly albedo values for the actinometric conditions in Poland results in only slight changes in comparison with the classical albedo model. For the Polish albedo data and the inclination of 35° the lowest MBE [%] of 0.41% is generated by the Gueymard model. The other models characterized by a low MBE [%] are: the Koronakis model, the Reindl model, the isotropic model and the Muneer model. As regards RMSE [%], the lowest error is generated by the Perez model. Among the top five models with the lowest RMSE [%] there

were also: the Bugler model, the Koronakis model, the isotropic model and the Temps & Coulson model. The highest CC of 0.9128 was scored by the Perez model. The other models with a high CC are: the Temps & Coulson model, the Bugler model, the Skartveit & Olseth model and the Klucher model.

At a pyranometer plane inclination of 50° the lowest MBE [%] of −0.30% was scored by the Reindl model. The other models with a low MBE [%] are (in descending order): the Perez model, the Muneer model, the Gueymard model and the Koronakis model. Among the top five models with the lowest relative root mean square error there were: the Koronakis model, the Temps & Coulson model, the Hay model, the Bugler model and the Perez model. The Koronakis model achieved an RMSE [%] of 29.49%. The highest correlation coefficient of 0.9171 was achieved by the Temps & Coulson model. The other models with a high CC were: the Bugler model, the Hay model, the Skartveit & Olseth model and the Klucher model.

Using the whole database covering the two inclination angles and the average monthly albedo values for the actinometric conditions prevailing in Poland, the lowest relative mean bias error of 0.53% was achieved by the Reindl model. Low MBE [%] errors were also scored by: the Gueymard model, the Koronakis model, the Muneer model and the Perez model. The lowest RMSE [%] of 31.92% was achieved by the Perez model. The other models with low relative root mean square errors are: the Koronakis model, the Bugler model, the Temps & Coulson model and the isotropic model. The highest correlation coefficient for the database covering the two measuring plane inclination angles was achieved by the Temps & Coulson model. The other models with a high CC are: the Perez model, the Bugler model, the Skartveit & Olseth model and the Klucher model.

Table 5. Statistical indicators of solar radiation models at inclination of 35° for average monthly albedos

Model	Statistical indicators of tested models				
	MBE	RMSE	MBE[%]	RMSE[%]	CC
	[Wh/m^2]	[Wh/m^2]	[%]	[%]	[–]
Isotropic	−8.03	121.22	−2.27	34.28	0.9068
Koronakis	−3.71	120.81	−1.05	34.16	0.9074
Jimenez & Castro	36.50	127.87	10.32	36.16	0.9036
Circumsolar	61.67	143.85	17.44	40.68	0.8963
Bugler	−18.75	120.62	−5.30	34.11	0.9092
Temps & Coulson	29.24	122.68	8.27	34.69	0.9127
Klucher	20.47	125.19	5.79	35.40	0.9079
Hay	9.43	123.03	2.67	34.79	0.9069
Ma & Iqbal	24.84	125.40	7.02	35.46	0.9077
Skartveit & Olseth	50.05	134.03	14.15	37.90	0.9089
Reindl	4.32	123.28	1.22	34.86	0.9061
Gueymard	1.45	123.37	0.41	34.88	0.9059
Muneer	8.06	125.79	2.28	35.57	0.9044
Perez	10.28	119.12	2.91	33.68	0.9128

Table 6. Statistical indicators of solar radiation models at inclination of 50° for average monthly albedos

Model	Statistical indicators of tested models				
	MBE	RMSE	MBE [%]	RMSE [%]	CC
	[Wh/m^2]	[Wh/m^2]	[%]	[%]	[–]
Isotropic	−19.36	116.90	−5.01	30.23	0.9086
Koronakis	−9.78	114.02	−2.53	29.49	0.9116
Jimenez & Castro	29.11	125.18	7.53	32.38	0.8979
Circumsolar	59.97	150.35	15.51	38.89	0.8779
Bugler	−28.92	115.21	−7.48	29.80	0.9145
Temps & Coulson	25.39	114.17	6.57	29.53	0.9171
Klucher	27.08	119.79	7.00	30.98	0.9118
Hay	12.13	115.22	3.14	29.80	0.9124
Ma & Iqbal	19.73	122.88	5.10	31.78	0.9038
Skartveit & Olseth	47.08	125.83	12.18	32.54	0.9123
Reindl	−1.17	121.56	−0.30	31.44	0.9018
Gueymard	−6.53	122.02	−1.69	31.56	0.9015
Muneer	4.63	124.72	1.20	32.26	0.8997
Perez	3.86	115.30	1.00	29.82	0.9114

Table 7. Statistical indicators of solar radiation models for whole measurement database and average monthly albedos

Model	Statistical indicators of tested models				
	MBE	RMSE	MBE[%]	RMSE[%]	CC
	[Wh/m^2]	[Wh/m^2]	[%]	[%]	[–]
Isotropic	−12.96	119.36	−3.52	32.43	0.9075
Koronakis	−6.35	117.91	−1.73	32.04	0.9093
Jimenez & Castro	33.28	126.71	9.04	34.43	0.9014
Circumsolar	60.93	146.72	16.56	39.87	0.8888
Bugler	−23.17	118.30	−6.30	32.15	0.9114
Temps & Coulson	27.56	119.05	7.49	32.35	0.9147
Klucher	23.35	122.87	6.34	33.39	0.9098
Hay	10.61	119.69	2.88	32.52	0.9095
Ma & Iqbal	22.62	124.31	6.15	33.78	0.9063
Skartveit & Olseth	48.76	130.52	13.25	35.47	0.9105
Reindl	1.93	122.54	0.53	33.30	0.9045
Gueymard	−2.02	122.79	−0.55	33.37	0.9042
Muneer	6.57	125.32	1.78	34.05	0.9027
Perez	7.49	117.47	2.03	31.92	0.9124

6. Conclusions

The rational use of thermal energy in buildings still remains a serious economic and technical problem in many countries, including Poland. Currently in all the EU countries organizational and technical projects aimed at rationalizing annual energy consumption in buildings and consequently, improving environmental protection by

reducing the release of greenhouse gases are being carried out. Also in Poland a series of problems in this field are being solved. Among others, legislative work aimed at introducing the EU's energy efficiency assessment system for buildings and flats is being done (European Energy Performance of Building Directive – EPBD).

As the world fossil fuel reserves are depleted, increasingly more attention is devoted to the possibilities of using renewable energy sources, mainly solar radiation energy, to improve the thermal balance of buildings, chiefly through the conversion of solar energy into heat energy (solar collectors) and electric energy (photovoltaic cells). Solar radiation energy not only aids the annual thermal balance of a building, but also is a source of natural lighting inside it.

The correct modelling of the intensity of solar radiation onto inclined planes is particularly important for calculating solar gains of a building and planes exposed to solar radiation intensity, with renewable energy (solar collectors or photovoltaic panels) use in mind.

Statistical analyses of 14 major models of the intensity of solar radiation onto an inclined plane were carried out. The data yielded by the theoretical models were compared with measurement data for the period from December 2002 to October 2006 from the actinometric station in the SolarLAB Photovoltaic Laboratory in Wrocław.

Among the analyzed models of total solar radiation onto an inclined plane the best results were scored by: the Reindl model, the Gueymard model, the Perez model, the Koronakis model and the Muneer model. The models are characterized by low statistical errors and high coefficients of correlation between measurement and theoretical data. It should be noted that from the five best models as many as four (the Reindl model, the Gueymard model, the Perez model and the Muneer model) are the latest generation anisotropic models, i.e. they take into account the region over the horizon line, with elevated diffuse radiation emission.

No large differences between the results yielded by the statistical models using the standard albedo model (0.20) and the average monthly albedo for the actinometric conditions prevailing in Poland were found.

Thus it seems that anisotropic models of solar radiation onto inclined planes, which take into account the region with elevated diffuse radiation intensity above the horizon line, are the most suitable for the climatic conditions prevailing in Poland. When no local albedo data are available, the classical 0.2 albedo model can be successfully used.

One should also note that the analyzed models of solar radiation onto inclined planes can be employed in other engineering fields. They can be helpful in calculating thermal stresses in building structures exposed to strong insolation (e.g. cooling towers, chimneys, silos, bridges).

References

[1] Liu B., Jordan R.: *Daily insolation on surfaces tilted towards the equator*, Trans. ASHRAE, 1962, pp. 526−541.

[2] Koronakis P.: *On the choice of the angle of tilt for south facing solar collectors in the Athens basin area*, Solar Energy, 36, 1986, pp. 217−225.

[3] Jimenez J., Castro Y.: *Solar radiation on sloping surfaces with different orientations in Granada*, Spain, Solar Energy, 28, 1982, pp. 257−262.

[4] Iqbal M.: *An introduction to solar radiation*, Academic Press, Canada, 1983.

[5] Bugler J.: *The determination of hourly insolation on an inclined plane using a diffuse irradiance model based on hourly measured global horizontal insolation*, Solar Energy, 19, 1977, pp. 477−491.

[6] Temps R., Coulson K.: *Solar radiation incident upon slopes of different orientations*, Solar Energy, 19, 1977, pp. 179−184.

[7] Klucher T.: *Evaluation of models to predict insolation on tilted surfaces*, Solar Energy, 23, 1979, pp. 111−114.

[8] Hay J., Davies J.: *Calculation of the solar radiation incident on a inclined surface*, Proceedings First Canadian Solar Radiation Data Workshop, 1980, pp. 59−72.

[9] Ma C., Iqbal M.: *Statistical comparison of models for estimating solar radiation on inclined surfaces*, Solar Energy, 31, 1983, pp. 313−317.

[10] Skartveit A., Olseth J.: *Modelling slope irradiance at high latitudes*, Solar Energy, 38 1987, pp. 271−274.

[11] Reindl D., Beckman W., Duffie J.: *Evaluation of hourly tilted surface radiation models*, Solar Energy, 45, 1990, pp. 9−17.

[12] Gueymard C.: *An anisotropic solar irradiance model for tilted surfaces and its comparison with selected engineering algorithms*, Solar Energy, 38, 1987, pp. 367−386, Erratum, Solar Energy, 40, 1988, pp. 175.

[13] Muneer T.: *Solar Radiation and Daylight Models*, 2nd edition, Elsevier Butterworth-Heinemann, 2004.

[14] Perez R., Ineichen P., Seals R., Michalsky J., Stewart R.: *Modelling daylight availability and irradiance components from direct and global irradiance*, Solar Energy, 44, 1990, pp.271−289.

[15] Kossecka E., Chochowski A., Czekalski D.: *Analysis of estimated and measured solar radiation on a tilted surface*, Archives of Civil Engineering, 49, 2003, pp. 531−544.

[16] Kossecka E., Chochowski A., Czekalski D.: *Comparison of measured at SGGW station and calculated solar radiation on a tilted surface*, Archives of Civil Engineering, 49, 2003, pp. 241−251.

[17] Włodarczyk D., Nowak H.: *Modelling of the solar radiation onto inclined planes* (in Polish). XI Polish Scientific Technical Conference: Building Physics in Theory and Practice, Łódź, 2007, Poland, pp. 305−310.

[18] Włodarczyk D., Nowak H.: *Estimation of a diffuse fraction from hourly global horizontal data from Wroclaw* (in Polish), I International Conference on Solar Energy and Ecobuildings: "Renewable Energy. Innovative Ideas and Technologies for Buildings", Solina, 2006, Poland, pp. 549−556.

[19] Włodarczyk D., Nowak H.: *Diffuse sky radiation models' accuracy analysis based on measurement data for Lower Silesia region*, Archives of Civil Engineering, 3, 2008.

[20] Jimenez J., Castro Y.: *Solar radiation on sloping surfaces with different orientations in Granada*, Spain, Solar Energy, 28, 1982, pp. 257−262.

[21] Hamilton H., Jackson A.: *A shield for obtaining diffuse sky radiation from portions of the sky*, Solar Energy, 34, 1985, pp. 121−123.

[22] Liu B., Jordan R.: *The long term average performance of flat plate solar energy collectors*, Solar Energy, 7, 1963, pp. 53−74.

[23] Podogrocki J. (red.): *Development of comparative heating season for estimating energy use in buildings* (in Polish), Part II. Development of actinomertic characteristics. IMGW, Warsaw 1990, Poland.

[24] Keindrick D.: *Guide to recommended practice of daylight measurement*, International Commission on Illumination (CIE), Report No. CIE-108, Wien, Austria, 1994.

[25] Notton G., Cristofari C., Muselli M., Poggi P.: *Calculation of an hourly basis of solar diffuse irradiations from global data for horizontal surface in Ajaccio*, Energy Conversion and Management, 45, 2004, pp. 2849−2866.

Analiza statystyczna modeli promieniowania słonecznego na płaszczyzny pochylone w warunkach klimatycznych Dolnego Śląska

W artykule przedstawiono wyniki analizy statystycznej większości znanych z literatury przedmiotu modeli natężenia promieniowania słonecznego na płaszczyznę pochyloną. Cechą różniącą poszczególne modele jest odmienne traktowanie promieniowania rozproszonego: od najprostszego, klasycznego modelu izotropowego po najbardziej rozbudowany model anizotropowy Pereza. Jest to pierwsza tak kompleksowa analiza modeli promieniowania słonecznego na płaszczyzny pochylone przeprowadzona w polskich warunkach aktynometrycznych.

Dane pochodzące z modeli teoretycznych porównano z danymi pomiarowymi ze stanowiska aktynometrycznego w Laboratorium Fotowoltaicznym SolarLAB Politechniki Wrocławskiej. Dane mierzono w okresie od grudnia 2002 do października 2006 wykorzystując do tego pyranometry CM21 Kipp&Zonen.

Dane pomiarowe zostały poddane procedurze kontroli jakości danych aktynometrycznych CIE [24], pozwalającej na eliminację danych błędnych, związanych np. z awariami systemu pomiarowego, przeszkód terenowych itd.

Wyniki analizy statystycznej w sposób bezsprzeczny potwierdziły wyższość modeli anizotropowych nad modelami izotropowymi oraz pseudoizotropowymi. Wśród modeli anizotropowych najlepsze wyniki uzyskiwały modele uwzględniające w teorii obszar nieboskłonu nad horyzontem emitujący promieniowanie rozproszone.

Zbadano także potencjalne korzyści ze stosowania miesięcznych danych albedo charakterystycznych dla lokalizacji pomiaru względem klasycznego założenia dla albedo wynoszącego w skali całego roku 0,20. Nie stwierdzono znaczących różnic w wynikach przy stosowaniu obu podejść modelowania promieniowania odbitego.

The influence of annealing temperature and time on the structure and features of the Al-Si coatings on steel sheets, purposed for pressured welded pipes applied in exhaust systems

K. ŻABA

University of Science and Technology, al. Mickiewicza 30, 30-059 Kraków, Poland

The research results shown in the article characterize the initial state of the Al-Si coating on the steel sheet and its evolution, being an effect of the influence of the temperature and the time.

The heating was carried out in different temperatures (up to 800 °C) and in different periods. After the heating, observation of the sections with the appliance of a scanning electron microscope was realized and microanalyses of the chemical composition were carried out. The state and the features of the coatings were also tested in technological tests by bumping, deep drawing, bending and expanding.

The results of microhardness research, documenting structural changes, are also presented.

Keywords: *Al-Si coating, annealing temperature, intermetallic layer, microhardness*

1. Formulating the problem

The reason for the appliance of pressure welded pipes with Al-Si coatings, for elements of exhaust systems, is the effect of jointing the strength features of steel with the resistance against high temperatures and corrosion of the Al-Si coating.

The pipes are manufactured as smooth or perforated of two-side sheets (Figure 1), with a thermally spread coating of ca. 9% contents of Si and standard thickness of 20 μm.

The choice of the grade of steel is determined by the requirements concerning the plastic features, necessary in the further conversion of the pipes.
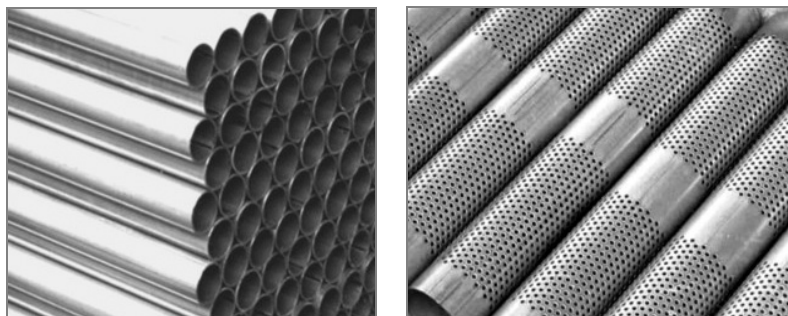

Fig. 1. A photo of exemplary smooth and perforated pipes for the elements of exhaust systems

The research results shown in the article characterize the initial state of the coating and its evolution, being an effect of the influence of the temperature and the time. This is both a problem of changing the state of the coating being the effect of performing of the heat influence zone in the process of inductive heating of the edge of the port pipe during pressure welding, as well as changing the features of the coating in the exploitation conditions.

The researches answer also the question of the consequences of the possible, specially introduced action of heating the sheet or the ready product, tending to achieve a new complex of features.

The heating was carried out in different temperatures (up to 800 °C) and in different periods. After the heating, observation of the sections with the appliance of a scanning electron microscope was realized and microanalyses of the chemical composition were carried out. The state and the features of the coatings were also tested in technological tests, also including microhardness, documenting structural changes.

The material used for the research was steel with Al-Si coating [1–2]. The researches of Al-Si coat on steel sheets were presented in papers [3–11].

2. The results of observations of the coating in initial state

The basic information concerning the coating spread on the sheet is shown in the photo in Figure 2. An intermetallic Al-Fe-Si alloy layer, guaranteeing the adherence of the Al-Si coating, is visible.

⇐ ALUMINIUM-SILICON ALLOY

⇐ IRON-ALUMINIUM-SILICON INTERMETALLIC
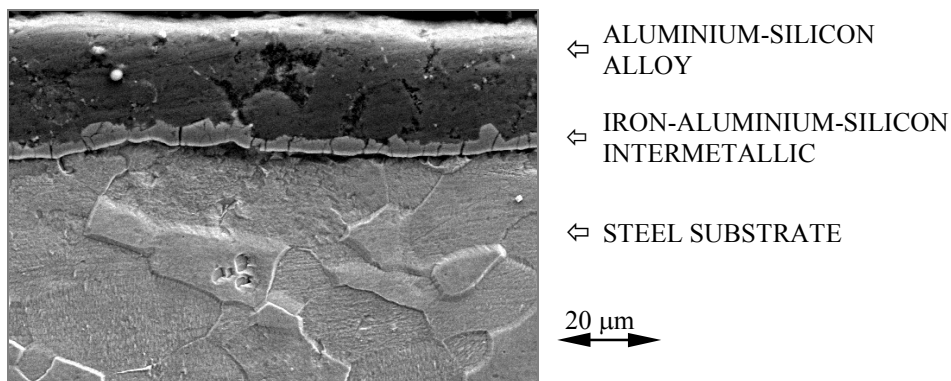
⇐ STEEL SUBSTRATE

20 μm

Fig. 2. The results of observation of the coating with the visible intermediate layer

In the photo and tables shown in Figure 3 the results of local and linear analyses of the chemical composition of the coating were shown.

A stepwise growth of Fe contents up to ca. 30% the transitory zone can be seen. The contents of Al decreases in this zone. Huge silicon separations visible in the photo

of the microstructure cause the characteristic leaps of the curve of Si contents. The decrease of Al is associated with Si growth and inversely.
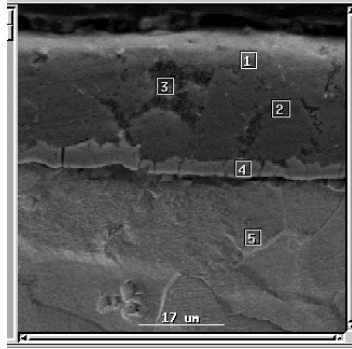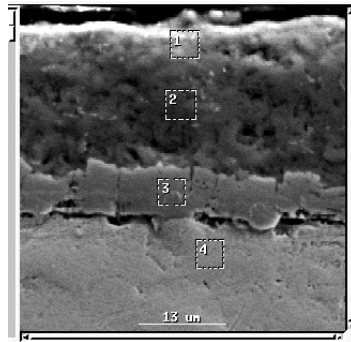

	Al	Fe	Si
P1	96.5	1.7	1.8
P2	88.5	0.9	10.6
P3	63.8	7.9	28.3
P4	57.1	30.4	12.5
P5	0.4	99.4	0.2

Fig. 3. The results of the local and linear analysis of coating in initial state

3. The evolution of the structure and chemical consistence of the coating after heating in different temperatures and times

After the heating in temperature between 100–300 °C during the time of 2–1350 hours there were no changes of the structure and chemical consistence of the coating.

Different situation was in temperature 500 °C and 800 °C. In Figures 4, 5 the results of local analysis of the contents of each component of the coating on the samples heated in temperatures 500 °C during the time of 2–24 hours are shown.

	Al	Fe	Si
P1	71.5	4.2	24.3
P2	54.5	34.1	11.4
P3	55.9	42.5	1.6
P4	0.2	99.7	0.1

Fig. 4. Results of local analysis, 500 °C/2 h
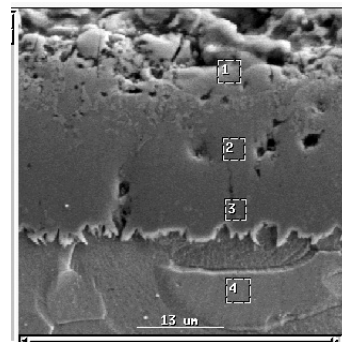
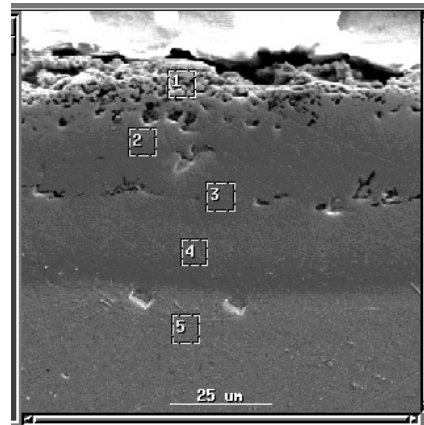|	Al	Fe	Si
P1	44.5	41.1	14.4
P2	54.9	43.6	1.5
P3	54.4	44.9	0.7
P4	0.2	99.7	0.1

Fig. 5. Results of local analysis, 500 °C/24 h

In Figures 6, 7 the local analysis' results of each component of the coating contents in the samples heated in temperature of 800 °C during the time of 2–24 hours are shown.
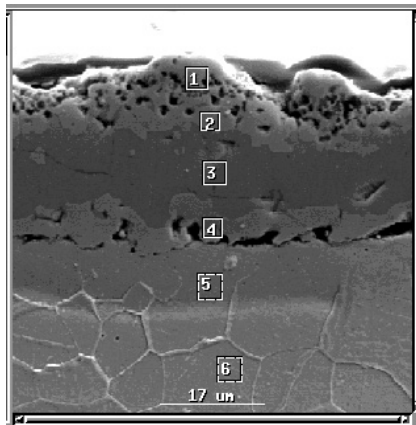
	Al	Fe	Si
P1	33.4	54.0	12.6
P2	29.5	62.7	7.8
P3	53.3	45.7	1.0
P4	22.9	69.4	7.7
P5	4.2	95.3	0.5
P6	0.1	99.8	0.1

	Al	Fe	Si
P1	29.9	62.7	7.4
P2	32.4	66.1	1.5
P3	15.2	81.1	3.7
P4	8.3	90.9	0.8
P5	0.1	99.8	0.1

Fig. 6. Results of local analysis, 800 °C/2 h   Fig. 7. Results of local analysis, 800 °C/24 h

The progress of the diffusion processes is observed in photos. The observations are illustrated by diagrams in Figures 8, 9.
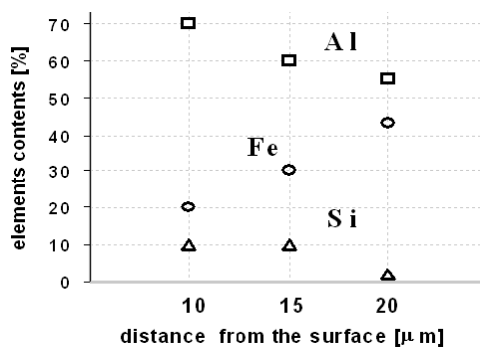
Fig. 8. Change of percentage contents of elements of the surface after annealing in 500 °C/2 h
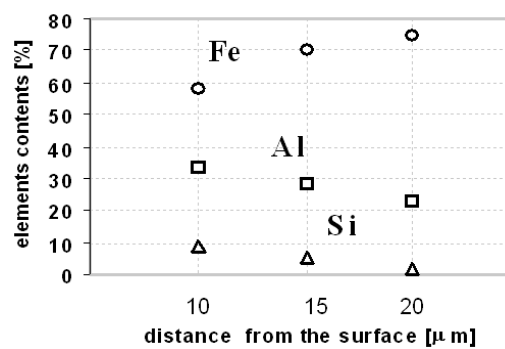
Fig. 9. Change of percentage contents of elements of the surface after annealing in 800 °C/24 h

4. Technological trials – testing the condition of the coating before and after annealing in increased temperature and different times

The samples cut of the sheets and the pipes, before and after annealing in temperature of 500 °C and 800 °C for 2 and 24 hours, were technologically tested by bumping, deep drawing, bending and expanding. The results of the observations are shown in Figures 10–13.
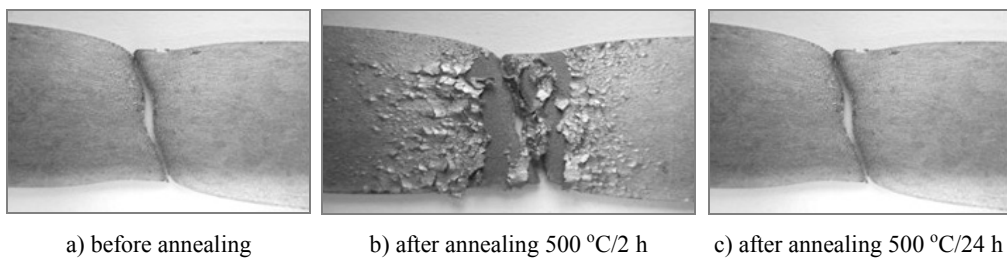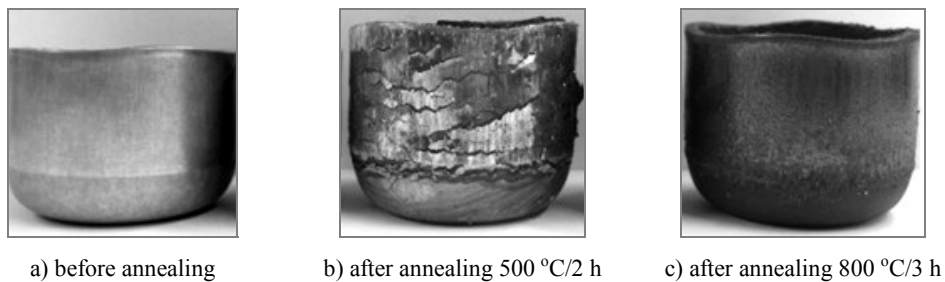

a) before annealing   b) after annealing 500 $^{\circ}$C/2 h   c) after annealing 500 $^{\circ}$C/24 h

Fig. 10. The samples after bumping

a) before annealing   b) after annealing 500 $^{\circ}$C/2 h   c) after annealing 800 $^{\circ}$C/3 h

Fig. 11. The samples after the deep drawing

a) before annealing   b) after annealing 500 $^{\circ}$C/2 h   c) after annealing 500 $^{\circ}$C/24 h
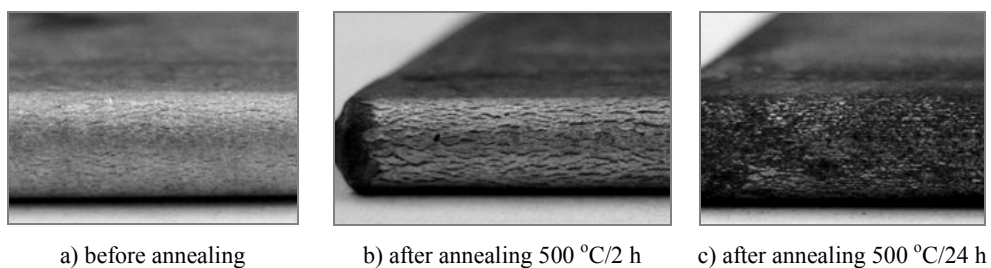
Fig. 12. The samples after the test of bending

The effect of surface oxidation is visible. After the fell of the few-millimetres thick layer brittle oxides, a chemically microanalysed surface of chemical contents of Fe-Al-Si alloy can be seen.
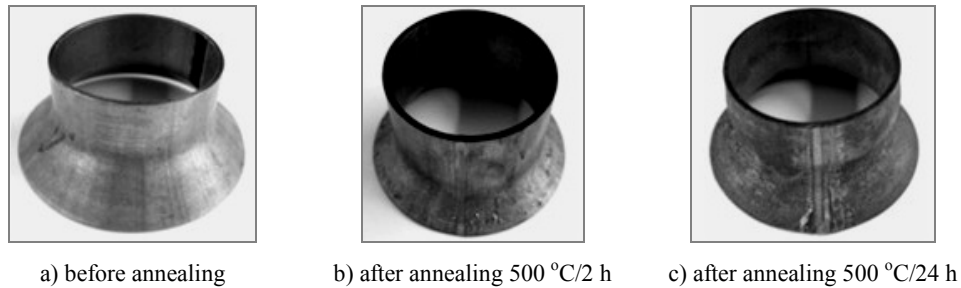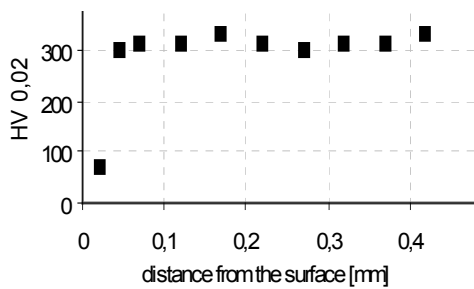
a) before annealing   b) after annealing 500 °C/2 h   c) after annealing 500 °C/24 h

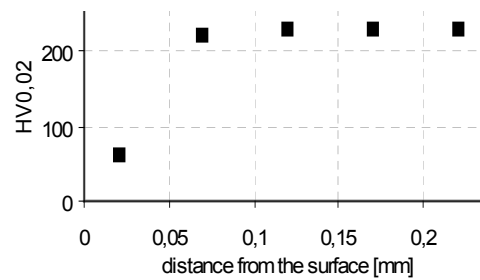Fig. 13. The pipe after the test of expanding

5. Testing coating microhardness

The following diagrams in Figures 14–17 show the results of the microhardness' measurements of the sheets' cross-section before and after annealing at the temperature of 500 and 800 °C for 2 and 24 hours.
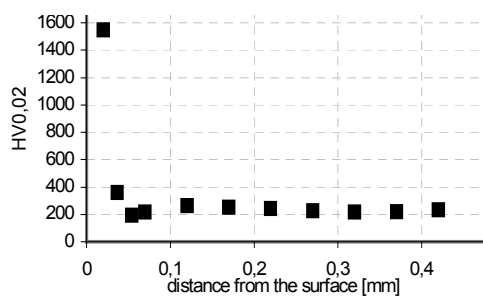

Coating hardness 65–83, Steel hardness 297–331

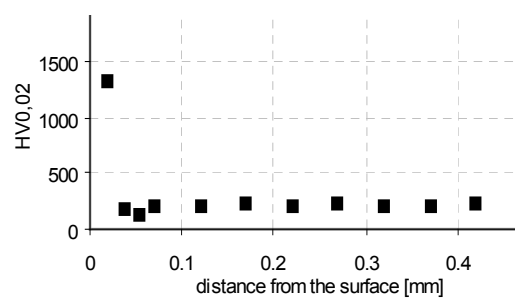Fig. 14. Sample without heating treatment

Coating hardness 58–61, Steel hardness 194–232

Fig. 15. Sample after annealing at 500°C/2h

Coating hard. 1547–2187, Steel hard. 192–262

Fig. 16. Sample after annealing at 500 °C/24 h

Coating hard. 886–1323, Steele hard. 194–232

Fig. 17. Sample after annealing at 800 °C/3 h

6. Summary

1. The coating in its initial state is a two-layer coating. The external layer is an Al-Si alloy of melting temperature ca. 580–590 °C, depending on Si contents. The intermetallic layer is an Al-Fe-Si alloy.

2. In the increased temperature, the two-layer coating transforms (as an effect of diffusion processes) into a one-layer form, of three-components alloy of Al-Fe-Si.

3. The transformed coating gains new features, for instance its melting temperature rises.

4. It has been found, that the coating transformed by the performance of the temperature and time becomes susceptible to distortions under the conditions of creating a one-layer structure.

5. The measurements of the microhardness document the meaning of the changes of the features caused by the diffusion.

References

[1] ASTM A463/A463M − 06: *Standard specification for steel sheet, aluminum-coated, by the hot-dip process*.
[2] ASM Handbook: *Surface engineering*, ASM International, Handbook Commitee, Vol. 5, 1994, pp. 346.
[3] Kawase H., Takezoe A.: *Peeling of coated metal due to severe press-forming in aluminized steel sheet*, Transactions of the Iron and Steel Institute of Japan, Vol. 22 , No. 5, 1982, pp. 371–376.
[4] Sano M., Kubota N., Masuhara K., Yamayoshi K., Fukumoto H.: *Development of pre-painted aluminized steel sheet for automotive mufflers*, SAE International, 1985.
[5] Kobayashi S., Yakou T.: *Control of intermetallic compound layers at interface between steel and aluminum by diffusion-treatment*, Materials Science and Engineering A, Vol. 338, Issues 1–2, 2002, pp. 44–53.
[6] Żaba K., Nowak S., Kąc S., Wróbel M.: *Research on temperature time and atmospheric impact on Al-Si coat of low-carbon steel strips*, International Conference: Problems of modern techniques in aspect of engineering and education, Pedagogical University Cracow, Institute of Technology – Cracow, November, 2006, Monography, pp. 73–78.
[7] Wang Chaur-Jeng, Chen Shih-Ming: *The high-temperature oxidation behavior of hot-dipping Al-Si coating on low carbon steel*, Surface and Coatings Technology, Vol. 200, Issue 22–23, 2006, pp. 6601–6605.
[8] Kee-Hyun Kim, Van-Daele Benny, Van-Tendeloo Gustaaf, Young-Sug Chung, Jong Kyu Yoon: *Analysis of the intermetallic compound formed in hot dip aluminized steel*, Advanced Materials Research, Vol. 15–17, 2007, pp. 159–163.
[9] Awan G.H., Ahmed F., Ali L., Shuja M.S. Hasan F.: *Effect of coating-thickness on the formability of hot dip aluminized steel*, Pakistan Journal of Engineering and Applied Science, Vol. 2, 2008, pp. 14–21.
[10] Gul Hameed Awan, Faiz ul Hasan *The morphology of coating/substrate interface in hot-dip-aluminized steels*, Materials Science and Engineering A, Vol. 472, Issues 1–2, 2008, pp. 157–165.

[11] Wang Deqing: *Phase evolution of an aluminized steel by oxidation treatment*, Applied Surface Science, Vol. 254, Issue 10, 2008, pp. 3026–3032.

Wpływ temperatury i czasu wyżarzania na strukturę i własności powłoki Al-Si na stalowych blachach, przeznaczonych na zgrzewane rury stosowane w układach wydechowych

Przedstawione w artykule wyniki badań charakteryzują stan początkowy powłoki Al-Si oraz jej ewolucję skutkiem oddziaływania temperatury i czasu.

Nagrzewanie prowadzono w różnych temperaturach (do 800 °C) i w różnych czasach.

Po nagrzewaniu dokonano obserwacji przekrojów za pomocą elektronowego mikroskopu skaningowego oraz dokonano mikroanaliz składu chemicznego. Badano również stan i własności powłok w testach technologicznych, w tym mikrotwardość, dokumentującą zmiany strukturalne.

Information for Authors

Send to: *Archives of Civil and Mechanical Engineering*
            Polish Academy of Sciences, Wrocław Branch
            Podwale 75, 50-449 Wrocław, Poland

Archives of Civil and Mechanical Engineering (ACME) publishes both theoretical and experimental papers which explore or exploit new ideas and techniques in the following areas: structural engineering (structures, machines and mechanical systems), mechanics of materials (elasticity, plasticity, rheology, fatigue, fracture mechanics), materials science (metals, composites, ceramics, plastics, wood, concrete, etc., their structures and properties, methods of evaluation), manufacturing engineering (process design, simulation, diagnostics, maintenance, durability, reliability). In addition to research papers, the Editorial Board welcome: state-of-the-art reviews of specialized topics, letters to the Editor for quick publication, brief work-in-progress reports, brief accounts of completed doctoral thesis (one page is maximum), and bibliographical note on habilitation theses (maximum 250 words). All papers are subject to a referee procedure, except for letters, work-in-progress reports and doctoral and habilitation theses, which are briefly reviewed by the Editorial Board.

The papers submitted have to be unpublished works and should not be considered for publication elsewhere.

The Editorial Board would be grateful for all comments on the idea of the journal.

Detailed information about the Journal on web:
    http://www.acme.pwr.wroc.pl
    http://www.pan.wroc.pl
    www.ib.pwr.wroc.pl/wydzial/czasopismoACME.html
    http://www.wmech.pwr.wroc.pl

The papers should be submitted through the webside
    http://www.acme.pwr.wroc.pl

Price 15 zł
(0% VAT)